creative commons
COMMONS DEED

저작자표시-비영리-변경금지 2.0 대한민국

이용자는 아래의 조건을 따르는 경우에 한하여 자유롭게

- 이 저작물을 복제, 배포, 전송, 전시, 공연 및 방송할 수 있습니다.

다음과 같은 조건을 따라야 합니다:

**저작자표시**. 귀하는 원저작자를 표시하여야 합니다.

**비영리**. 귀하는 이 저작물을 영리 목적으로 이용할 수 없습니다.

**변경금지**. 귀하는 이 저작물을 개작, 변형 또는 가공할 수 없습니다.

- 귀하는, 이 저작물의 재이용이나 배포의 경우, 이 저작물에 적용된 이용허락조건을 명확하게 나타내어야 합니다.
- 저작권자로부터 별도의 허가를 받으면 이러한 조건들은 적용되지 않습니다.

**저작권법에 따른 이용자의 권리는 위의 내용에 의하여 영향을 받지 않습니다.**

이것은 이용허락규약(Legal Code)을 이해하기 쉽게 요약한 것입니다.

Disclaimer

dCollection

ULSAN NATIONAL INSTITUTE OF SCIENCE AND TECHNOLOGY

Doctoral Thesis

# Multiscale simulation study of the influence of molecular architecture on polymer structure and rheology under flow

Seung Heum Jeong

School of Energy and Chemical Engineering

(Chemical Engineering)

Ulsan National Institute of Science and Technology

2021

ULSAN NATIONAL INSTITUTE OF
SCIENCE AND TECHNOLOGY

# Multiscale simulation study of the influence of molecular architecture on polymer structure and rheology under flow

Seung Heum Jeong

School of Energy and Chemical Engineering

(Chemical Engineering)

Ulsan National Institute of Science and Technology

ULSAN NATIONAL INSTITUTE OF
SCIENCE AND TECHNOLOGY

# Multiscale simulation study of the influence of molecular architecture on polymer structure and rheology under flow

A thesis/dissertation submitted to
Ulsan National Institute of Science and Technology
in partial fulfillment of the
requirements for the degree of
Doctor of Philosophy

Seung Heum Jeong

06.18.2021 of submission

Approved by

Advisor
Chunggi Baig

ULSAN NATIONAL INSTITUTE OF
SCIENCE AND TECHNOLOGY

# Multiscale simulation study of the influence of molecular architecture on polymer structure and rheology under flow

Seung Heum Jeong

This certifies that the thesis/dissertation of Seung Heum Jeong is approved.

06.18.2021 of submission

Signature

Advisor:Chunggi Baig

Signature

Jaeup Kim: Thesis Committee member #1

Signature

Dongwoog Lee: Thesis Committee member #2

Signature

Jiseok Lee: Thesis Committee member #3

Signature

Jun Mo Kim: Thesis Committee member #4

*three signatures total in case of masters

ULSAN NATIONAL INSTITUTE OF
SCIENCE AND TECHNOLOGY


## Abstract

In polymer physics, the molecular aspects of a polymer material, such as chemical constituents, molecular weight, and molecular architectures, are critical factors that affect the material properties. Therefore, it is not surprising, there were many investigations for understanding the fundamental role of the molecular architecture of the polymer to get the required structural and rheological properties of the polymeric system. Numerous experiments, simulations, and theories for the various molecular architecture of polymer have been performed and made in past decades. In particular, associated with the connectivity between monomers, the cases of long linear and long-chain branched polymers have been thoroughly investigated and revealed fundamental structural, dynamical, and rheological behaviors. However, though the structural and dynamical understanding for the linear and long-chain branched polymers brought us the basis of molecular architecture, a comprehensive understanding of molecular architecture has not yet been obtained, particularly because of a lack of knowledge on the role of short-chain branches and ring-shaped structures.

In chapter 1, we have comprehensively studied the general effect of short- and long-chain branching on the structural and rheological properties of polymeric materials using non-equilibrium molecular dynamics (NEMD) and Brownian dynamics (BD) simulations for a several short-chain branched (SCB) polymers under shear and elongational flows. Our results show that the short branches constantly disturb stretching and alignment of the attached part toward flow direction via their fast random dynamics attributed to the short characteristic time, whereas the long branches are easily aligned. Further, we have observed this fundamental role of short and long branches is remaining unchanged independent of the flow type and strength. However, by altering the short branch densities and their distributions along the backbone or long branches, we were revealed the overall chain alignment and rheological behaviors for the SCB polymer could be dramatically changing. For instance, compared to the H-polymer having two long-chain branches along the linear backbone, the H-(SCB_Backbone) polymer having short branches along the backbone of the H-polymer exhibit considerably less shear-thinning behavior of viscosity resulting from the lesser chain alignment of the SCB backbone. In contrast, the H-(SCB_arm) polymer, which has short branches along the four long branches of H-polymer, displays backbone stretch attributed to the effective tensile force from the fluctuation of both ends leading to a higher degree of shear-thinning behavior of viscosity.

In chapter 2, we have studied about the ring-shaped polymer structures based on the novel viewpoint that ring polymers, with their closed-loop molecular geometry, are naturally defined by an intrinsic two-dimensional topological surface. We analyzed the fundamental structural characteristics and representative dynamic mechanisms of ring polymers under shear flow using NEMD and BD simulations. We then proposed several representative physical measures that could effectively be used to characterize the overall ring structure and dynamics. To directly quantify the physical properties, an

ULSAN NATIONAL INSTITUTE OF
SCIENCE AND TECHNOLOGY

efficient numerical algorithm was developed to describe the complex intrinsic surfaces represented by flexible ring polymers.

ULSAN NATIONAL INSTITUTE OF
SCIENCE AND TECHNOLOGY

ULSAN NATIONAL INSTITUTE OF SCIENCE AND TECHNOLOGY

# Contents

ULSAN NATIONAL INSTITUTE OF
SCIENCE AND TECHNOLOGY

ULSAN NATIONAL INSTITUTE OF SCIENCE AND TECHNOLOGY

## List of Figures

ULSAN NATIONAL INSTITUTE OF SCIENCE AND TECHNOLOGY

intermediate flow strengths, for the simulated linear, SCB_uniform, SCB_dumbbell, and SCB_center systems. The chain end-to-end distances are made dimensionless with $\left\langle \tilde{R}_{\text{ete}}^2 \right\rangle = \left\langle R_{\text{ete}}^2 \right\rangle ( K / k_B T )$ and $\left|\tilde{\mathbf{R}}_{\text{ete}}\right| = \left|\mathbf{R}_{\text{ete}}\right| \sqrt{K / k_B T}$, where $K$, $k_B$, and $T$ denote the elastic spring constant, the Boltzmann constant, and temperature, respectively.

**Figure 2.4** (a) Root mean-square chain end-to-end distance $\left\langle R_{\text{ete}}^2 \right\rangle$ of the whole backbone, the bare backbone part, and the branched backbone part as a function of *Wi* for the SCB_dumbbell (top panel) and SCB_center (bottom panel) systems. The vertical dotted line denotes the borderline between the two characteristic flow regimes: in the first regime (*Wi* < 30), only the bare backbone stretches, whereas in the second regime (*Wi* > 30), both the bare and branched backbone parts stretch. The horizontal arrows direct the proper *y*-axis of data points that have the same color. The chain end-to-end distance is made dimensionless likewise the same in Figure 2.3. (b) Shear stress $\sigma_{xy}$, contributions of the whole chain (black filled circle), the bare backbone (black open circle), and the branched backbone (orange open circle) for the SCB_dumbbell (top panel) and SCB_center (bottom panel) systems. The shear stress is made dimensionless with $\tilde{\sigma}_{xy} = \sigma_{xy} \sqrt{k_B T / K^3}$. The error bars are smaller than the size of the symbols unless otherwise specified.

**Figure 2.5** (a) viscosity $\eta$ (normalized by the equilibrium value) (top panel), the first normal stress coefficient $\Psi_1$ (normalized by the equilibrium value) (middle panel), and rotation time (normalized by the equilibrium value) (bottom panel) as a function of *Wi* for the H-(original) (black circle)), H-(SCB_arm) (red triangle), and H_(SCB_backbone) (blue left triangle). Here rotation time was computed by the power spectral density (PSD) analysis through Fourier transformation of the time autocorrelation function $\left\langle \mathbf{u}(t) \cdot \mathbf{u}(0) \right\rangle$ where $\mathbf{u}(t)$ represents the unit backbone end-to-end vector. (b) Root mean-square chain end-to-end distance of the longest linear chain dimension $\left\langle R_{\text{ete,ll}}^2 \right\rangle$ (top panel), the backbone $\left\langle R_{\text{ete,bb}}^2 \right\rangle$ (middle panel), and the arm $\left\langle R_{\text{ete,arm}}^2 \right\rangle$ (bottom panel). The backbone and arm parts are schematically indicated by the inset. The chain end-to-end distance is made dimensionless likewise the same in Figure 2.3.

**Figure 2.6** Schematic illustrations for the fundamental molecular mechanisms underlying the rotational and tumbling dynamics of an individual chain for the linear, SCB_uniform, SCB_dumbbell, SCB_center, H-(original), H-(SCB_arm), and H-(SCB_backbone) systems under shear flow.

ULSAN NATIONAL INSTITUTE OF SCIENCE AND TECHNOLOGY

**Figure 2.7.** (a) Elongational viscosity $\eta_E$ [$\equiv -(\sigma_{xx} - \sigma_{yy})/4\dot{\varepsilon}$ where $\dot{\varepsilon}$ is the applied strain rate] and the root mean-square chain end-to-end distance of the longest linear chain dimension $\left\langle R^2_{\text{ete,ll}} \right\rangle$, the backbone $\left\langle R^2_{\text{ete,bb}} \right\rangle$, and the arm $\left\langle R^2_{\text{ete,arm}} \right\rangle$ as a function of *Wi* under uniaxial elongational flow. These chain end-to-end distances are made dimensionless likewise the same in Figure 2.3. The elongational viscosity is made dimensionless with $\tilde{\eta}_E = \eta_E(\sqrt{16\tilde{\tau}_R^2 k_B T/\zeta^2 K})$ where $\tilde{\tau}_R$ is the dimensionless Rouse time of the connector vector $\mathbf{Q}$. The horizontal dotted lines indicate the fully stretched length $\mathbf{R}_{\max} = \mathbf{Q} \times (N_{\text{bead}} - 1)$ of each dimension. (b) Simple schematics illustrating the dynamical features of the backbone and arms under elongational flow for H-(original), H-(SCB_arm), and H-(SCB_backbone) systems at the weak (*Wi* = 0.4), intermediate (*Wi* = 2), and high (*Wi* = 8) flow strengths. The vertical dotted lines in (a) indicate three representative (weak, intermediate, and high) flow strengths.

**Figure. 3.1** (a) Simple schematic description of the intrinsic surface constructing algorithm for the ring polymer. Rotational illustrations of the toy model under shear flow without the Brownian random force: (b) When there is no surface area facing the *yz*-plane at the initial state. (c) When there is non-zero surface area facing the *yz*-plane at the initial state. The yellow arrows in the illustrations indicate the normal vector of the toy model.

**Figure 3.2** (a) Projected areas of the intrinsic surface of the ring into three *xy*- (circles and dashed line), *xz*- (squares and solid line), and *yz*- (triangles and dotted line) planes for toy model (dark green lines), dilute system (black symbols), and melt system (orange symbols) as a function of Weissenberg number (*Wi*). The projected areas were normalized by the total area of the intrinsic ring surface $A_t$. (b) The ratio between $A_{xy}$ and $A_{xz}$ as a function of *Wi* for toy model (dark green line), dilute system (black circles), and melt system (orange circles). (c) The neutral direction (*zz*-)component of the gyration tensor $G_{\alpha\beta}$ [$= \frac{1}{N}\sum_{i=1}^{N}(\mathbf{r}_{i,\alpha} - \mathbf{r}_{c,\alpha})(\mathbf{r}_{i,\beta} - \mathbf{r}_{c,\beta})$, where $\mathbf{r}_i$, $\mathbf{r}_c$, and $N$ denote the position of particle $i$, the center of mass of the chain, and the number of particles per chain, respectively] for linear (triangles) and ring (circles) polymers with respect to *Wi*. The error bars are smaller than the size of the symbols unless otherwise specified.

**Figure 3.3** (a) Schematic illustrations for the representative molecular mechanisms for the ring polymer under shear flow. The colored backbone and beads in the schematics are markings to help understand

ULSAN NATIONAL INSTITUTE OF
SCIENCE AND TECHNOLOGY

the dynamics of the ring polymers that have no endpoints. (b) Averaged angle accumulation during a cycle of loop migration (left panel), end-loop tumbling (middle panel), and center-loop tumbling (right panel) for $\theta_n$ of $\mathbf{n}_{avg}$, $\theta_{xy}$ of $\mathbf{Q}_{xy}$ projected on the *xy*-plane, and $\theta_{yz}$ of $\mathbf{Q}_{yz}$ projected on the *yz*-plane. Notice that the relative position vector $\mathbf{Q}_i$ of $i^{th}$ atom or bead in a chain is represented by $\mathbf{Q}_i = \mathbf{r}_i - \mathbf{r}_c$ where $\mathbf{r}_c$ denotes the center of mass position vector of a chain.

**Figure 3.4** (a) The probability of the end-loop (circle) and center-loop (triangle) tumbling with respect to *Wi* for the dilute (black) and melt (orange) ring systems. (b) Probability distribution function (PDF) of the chain radius of gyration $R_g$ (normalized by the equilibrium value) for the $C_{400}$ ring (black line) and linear (dark green line) PE melts in the strong flow regime at *Wi* = 100 and 2000, respectively, where the polymer chains in each system become maximally stretched and oriented in the flow direction. The error bars are smaller than the size of the symbols unless otherwise specified.

**Figure 3.5** Time correlation functions (TCFs) ($\langle \mathbf{u}(t) \cdot \mathbf{u}(0) \rangle$, where **u** is a unit vector) for the ring-diameter vector $\mathbf{R}_d$ (black lines), center-to-center vector $\mathbf{R}_{ctc}$ (yellow lines), and averaged normal vector $\mathbf{n}_{avg}$ (red lines) at equilibrium (*Wi* = 0), intermediate (*Wi* = 200), and strong flow (*Wi* = 1000) strengths as a function of the reduced time $t/\tau_R$ for (a) dilute and (b) melt ring systems. (c) Simple schematic illustrations of the dynamics of $\mathbf{R}_{ctc}$ (yellow arrow) and $\mathbf{n}_{avg}$ (red arrow) during a cycle of end-loop tumbling (top schematics) and loop-migration (bottom schematics).

**Figure 3.6** (a) Schematic illustrations of link formation between inter-ring chains under shear flow. (b) PDFs of the chain radius of gyration (normalized by the equilibrium value) of all rings (black solid lines), the uncoupled individual rings (red dashed lines), and the linked supramolecular rings (blue dotted lines) for the melt ring system in the strong-flow regime (*Wi* = 240, 480, and 1000), where the average chain stretching and orientation toward flow (*x*-)direction are nearly saturated.

ULSAN NATIONAL INSTITUTE OF
SCIENCE AND TECHNOLOGY

# I. Introduction

## 1.1 General Introduction

In past decades, as described in numerous experiments, simulations, and theories, it is well known that dynamical and rheological responses of polymeric materials to an applied flow field are varying with their chemical structures.[1-9] In comparison to the simple monomeric materials, the polymeric materials have shown a unique property that drastic change of rheological properties with varying monomeric aspects of polymer (chemical structures), such as chemical composition, molecular weight, and molecular architecture. Therefore, in the case of polymeric materials, it is possible to get the required material properties by altering the chemical structure without changing the chemical constituents. This unique property of polymeric material has enabled the application of polymers to almost all areas of science and technology, from the down-scale, where laboratory and daily life, to the up-scale, where the industrial processes. So, in the point of polymer physics, it is not surprising to see remarkable advances in polymer synthesis techniques and fundamental study about the structure-property-phenomenon relationship of polymeric materials in past decades. Particularly, based on the connectivity or the entropic spring concept of the polymer chain, significant research of the structural and dynamical behaviors of linear and long-chain branched polymers under various flow conditions have been carried, and the complex rheological properties and phenomena of linear and long-chain branched polymers are now well understood.[2,10-15]

However, despite these advances, a comprehensive understanding in the field of the structure-property-phenomenon relationship of the polymer chain has not yet been obtained because of the lack of information concerning the short-chain branches and the closed-loop geometry (the ring-shaped). The former has been disregarded in the entropic-based concepts due to that it has not sufficient long length to have entropy, and the latter has no endpoints that could be applying the entropic spring concepts. Therefore, to achieve a comprehensive understanding of the influence of molecular structures to control the material properties of polymeric materials, comprehending the fundamental role of the short-chain branches and the closed-loop geometry in conjunction with that of the linear and long-chain branches is indispensable.

ULSAN NATIONAL INSTITUTE OF SCIENCE AND TECHNOLOGY

## 1.2 Simulation

In the field of polymer physics, since the importance of the chemical structure of polymer has been emerged via numerous experiments,[1-9] there were many tries to reveal the detailed microscopic information of polymer chain. However, despite the advance of experiment methods and theories, it is still challenging to get some detailed microscopic information about the polymer molecules directly, such as the dynamics mechanisms of a polymer molecule in response to the applied flow field. Therefore, to fill the lack of microscopic molecular information and explain how molecules behave, experimentalists and theoreticians have worked to construct models for simulation in past decades.[16,17] The early models for molecular simulation started from the observation of phenomena, such as the Weissenberg effect, Brownian motion, and neutron scattering experiments, it was established first in the early 19th century by Morrell and J. H. Hildebrand. They represented the simple liquid as the packing of many simple gelatin balls.[17] Based on this simple model of molecules in liquids, the development of a model for polymer liquid has been continuing nowadays by adding much detailed information founded from the experiments and theories to describe the real behavior of molecules in the microscopic scales as described in Figure. 1.1. The thermostat for accurate and reliable system conditions.[18,19] The intra modes of molecules like covalent bonds between atoms, bending angle between bonds, and torsional angles describing real polymer chain-shape.[20] The potential models to describe the equation of motion for the molecules.[21]

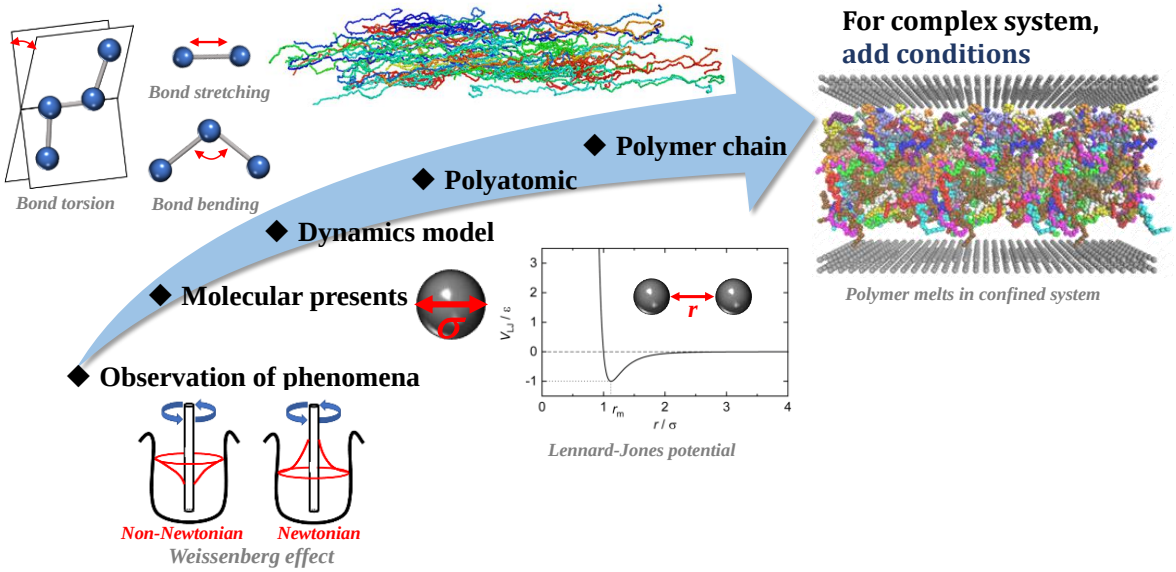


**Figure 1.1** Simple schematics about history of molecular dynamics simulation.

These additions of detailed pieces of information for the polymer model are helpful to describe the molecular behavior precisely and realistically with high reliability. Furthermore, compared to the experiment, simulation is capable of accurate and precise system design (e.g., no defects,

ULSAN NATIONAL INSTITUTE OF SCIENCE AND TECHNOLOGY

monodispersed molecular weight, required molecular architecture, no contamination, etc.) from the microscopic atomistic level to the macroscopic continuum level as shown in Figure 1.2.

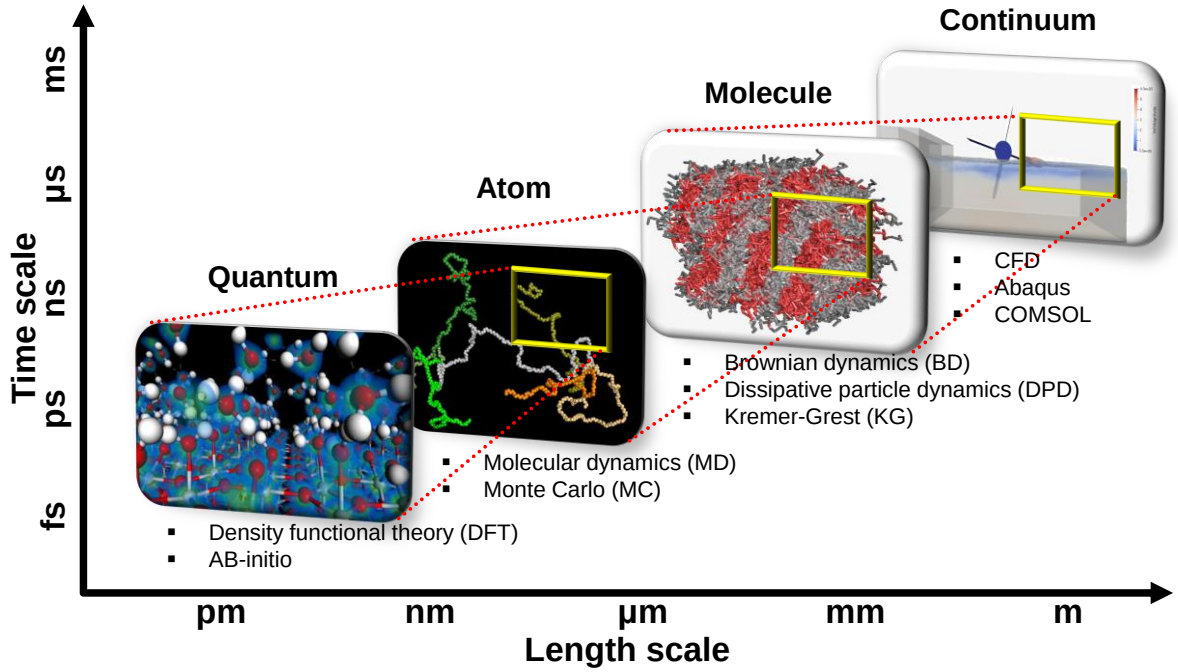


**Figure 1.2** Representative multi-scale simulation methods on various length and time scales.

Generally, as shown in Figure 1.2., a polymer system has several levels depending on time and length scales called multiscale, and its macroscopic properties and phenomena are the results of a combination of the characteristic structural and dynamical behaviors of molecule at each level. In short, the characteristic properties of each level of polymer system are composed of the physics origin at the lower levels. For a comprehensive understanding of the polymer system, it is necessary to examine the detailed behaviors of the overall scales of the system.

Based on the reliability of the model, which is attributed to the experiments and theories, the multiscale simulation method has been regarding as a powerful tool that provide a direct route from the microscopic details of a system to the macroscopic properties and phenomena of polymeric materials.

ULSAN NATIONAL INSTITUTE OF
SCIENCE AND TECHNOLOGY

## 1.3 References

[1] Bird R. B.; Armstrong R. C.; Hassager, O. *Dynamic of polymeric Liquids*; Wiley; New York, 1987; Vol. 1.

[2] Doi M.; Edwards, S. F. *The theory of polymer dynamics*; Clarendon Press; New York, 1986.

[3] Larson, R. G. *The structure and Rheology of Complex Fluids*; Oxford University Press; New York, 1999.

[4] Rubinstein M.; Colby, R. H. *Polymer Physics*; Oxford University Press; New York, 2003.

[5] Dealy J. M.; Larson, R. G. *Structure and rheology of molten polymers: from structure to flow behavior and back again*; Hanser Gardner Publications; Ohio, 2006.

[6] McLeish, T. C. B. Tube theory of entangled polymer dynamics. *Adv. Phys.* **2002**, *51*, 1379.

[7] Watanabe, H.; Matsumiya, Y.; van Ruymbeke, E.; Vlassopoulos, D.; Hadijichristidis, N. Viscoelastic and dielectric relaxation of a Cayley-tree-type polyisoprene: Test of molecular picture of dynamic tube dilation. *Macromolecules* **2008**, *41*, 6110.

[8] Robertson R. M.; Smith, D. E. Strong effects of molecular topology on diffusion of entangled DNA molecules. *Proc. Natl. Acad. Sci. U. S. A.* **2007**, *104*, 4824.

[9] Kapnistos, M.; Lang, M.; Vlassopoulos, D.; Phyckhout-Hintzen, W.; Richer, D.; Cho, D.; Chang T.; Rubinstein, M. Unexpected power-law stress relaxation of entangled ring polymers. *Nat. Mater.* **2008**, *7*, 997.

[10] Bird, R. B.; Curtiss, C. F.; Armstrong R. C.; Hassager, O. *Dynamics of Polymeric Liquids, Kinetic Theory*; Wiley; New York, 1987; Vol. 2.

[11] de Gennes, P. G. *Scaling Concepts in Polymer Physics*; Cornell University Press; Ithaca, 1979.

[12] Rouse, P. E. A theory of the linear viscoelastic properties of dilute solutions of coiling polymers. *J. Chem. Phys.* **1953**, *21*, 1272.

[13] Zimm, B. H. Dynamics of polymer molecules in dilute solution: viscoelasticity, flow birefringence and dielectric loss. *J. Chem. Phys.* **1956**, *24*, 269.

[14] de Gennes, P. G. Reptation of a polymer chain in the presence of fixed obstacles. *J. Chem. Phys.* **1971**, *55*, 572.

[15] Doi M.; Edwards, S. F. Dynamics of concentrated polymer systems. *J. Chem. Soc., Faraday Trans. 2: Molecular and Chemical Physics* **1978**, *74*, 1789; Part1, Part2, Part3, and Part4.

[16] Allen M. P.; Tildesley, D. J. *Computer simulation of liquids*; Clarendon Press; Oxford, 1987.

[17] Morrell, W. E.; Hildebrand, J. H. The distribution of molecules in a model liquid. *J. Chem. Phys.* **1936**, *4*, 224.

[18] Nose, S. A molecular dynamics method for simulations in the canonical ensemble. *Mol. Phys.* **1984**, *52*, 255-268.

[19] Hoover, W. G. Canonical dynamics: Equilibrium phase-space distributions. *Phys. Rev. A* **1985**,

ULSAN NATIONAL INSTITUTE OF
SCIENCE AND TECHNOLOGY

*31*, 1695.

[20] Baig, C.; Edwards, B. J. Keffer, D. J.; Cochran, H. D.; Harmandaris, V. A. Rheological and structural studies of linear polyethylene melts under planar elongational flow using non-equilibrium molecular dynamics simulations. *J. Chem. Phys.* **2006**, *124*, 084902.

[21] Siepmann, J. I.; Karaborni, S.; Smit, B. Simulating the critical behaviour of complex fluids. *Nature* **1993**, *365*, 330-332.

ULSAN NATIONAL INSTITUTE OF
SCIENCE AND TECHNOLOGY

# II. Influence of long- and short-chain branches on structural and rheological properties of polymer melts

***This chapter includes the materials from*:**

**Influence of molecular architecture on entanglement network: topological analysis of linear, long- and short-chain branched polyethylene melts via Monte Carlo simulation.**

**S. H. Jeong**, J. M. Kim, J. Yoon, Tzoumanekas, M. Kroger, and C. Baig, Soft Matter, 12, 3770-3786, (2016).

**Rheological influence of short-chain branching for polymeric materials under shear with variable branch density and branching architecture.**

**S. H. Jeong**†, J. M. Kim†, and C. Baig, Macromolecules, 50, 4491-4500 (2017).

**Rheological behaviors of H-shaped polymers incorporated with short branches under shear and elongational flows via FENE-Rouse model.**

**S. H. Jeong**†, J. M. Kim†, and C. Baig, J. Rheol., 62, 1115-1124 (2018).

---

## 2.1 Introduction

The many unique and useful physicochemical properties of polymeric material, which show different dynamical and rheological properties with varying microscopic molecular aspects such as chemical composition, molecular weight, and molecular architecture,[1-9] have enabled the application of polymeric materials to most fields of science and technology, including the large-scale use of plastic commodities in daily life, pharmaceutical biotechnology, and renewable energy engineering. Fundamentally, the physics origin for this versatile functionality of polymeric materials lies in the intrinsic variety of their internal molecular structures. Based on this fundamental, by altering the molecular structure without changing any of its chemical constituents, it is possible to manipulate the material properties to satisfy the given requirements. It thus not surprising to see remarkable advances in polymer synthesis techniques over the past decades that have led to the synthesis of a variety of molecular architectures.[10-14]

Apart from the molecular architecture, in the polymer physics theory, it is well established today that the dynamic mechanisms of a sufficiently long polymer molecule in a dilute state are very different from that in concentrated solutions or melts.[2,15,16] The former is generally described well by the Rouse and Zimm models,[17,18] which take into account only the chain connectivity by viewing a polymer molecule as a string of beads connected by the Hookean spring, and the latter can be described satisfactorily by the reptation or tube model.[19,20] Besides, for the long-chain branched polymers, there is a well-described model called as pom-pom model,[21] which is an extension of the tube model to branched polymers, adequately explains such rheological behavior by considering two additional

ULSAN NATIONAL INSTITUTE OF SCIENCE AND TECHNOLOGY

characteristic time scales: one associated with backbone stretching and the other associated with the arms withdrawal process.

However, despite these advances, which well-describe the fundamental aspects underlying the complex rheological properties and phenomena displayed by linear and long-chain branched polymers, a comprehensive understanding of the field of polymer rheology is still far from complete. One of the main lacking points is the role of short-chain branches, which has been disregarded in the customary entropic-based concepts because of insufficient length to have entropy.[15] In comparison to the linear and LCB polymers, which have sufficient lengths to apply the entropy-based treatment, the short-chain branches have very short lengths (e.g., tow, four, or six carbon atoms in polyethylene molecule). In this respect, recent numerical studies have firmly demonstrated the Brownian fast random dynamics of short-chain branches in association with their short characteristic relaxation time.[22] The significant random movements of short-chain branches were found to make the overall chain structure compact and less deformable in response to the applied shear flow; this can lead to less shear-thinning behavior of polymeric materials with respect to flow strength.[22-24]

The structural and rheological properties of the short-chain branched (SCB) polymers were strongly influenced by the branch density and spatial distribution of the short-chain branches along the backbone and long-chain branches.[23] Furthermore, distinct branching architectures significantly influenced the determination of characteristic molecular dynamics and mechanisms, in regard to chain rotation and tumbling behaviors under shear flow.[23,24] Comprehending the fundamental role of the short branches in conjunction with that of the long branches is indispensable for achieving a major goal to controls the material properties of branched polymers by altering the molecular architecture.

To this end, in this chapter, we have conducted extensive mesoscopic bead-spring Brownian dynamics (BD) simulations for a variety of well-defined SCB polymers with respect to the branch density and the branching architecture. Our results unambiguously confirm the distinctive dynamical role of short-chain branches, via their fast random motions, give rise to a compact and less deformed molecular structure in response to an applied flow field. Specifically, we show that the random dynamics of short-chain branches are associated with the structural resistance of the SCB polymers against the external flow, which becomes stronger as the branch density increases, irrespective of the total molecular weight or the backbone length. Furthermore, we observed a dramatic influence of the branching architecture, short-chain branching distribution along the backbone and long-chain branches (dangling arms), on the structural and rheological behaviors under the applied shear and uniaxial elongational flow fields.

Through a detailed analysis of the individual chain dynamics in a wide range of flow strengths, we reveal the fundamental physics and molecular mechanisms underlying these observations.

ULSAN NATIONAL INSTITUTE OF SCIENCE AND TECHNOLOGY

## 2.2 System studied and Method

To analyze the influence of branch density on the structural and rheological properties of the SCB system, we devised two different types of SCB polymer: (i) the first type where the backbone length and the number of short branches for a chain were both varied according to a specified branch density while the total chain length was constrained to 70 beads and (ii) the second type where the backbone length was fixed at 47 beads, but the number of short branches for a chain was varied, corresponding to the given branch densities. The branch density (the percentage of the backbone portion covered by short branches over the entire backbone) considered in this study spans the range of 6-100%.

To explore the effect of various branch architectures, we chose three representative types of the SCB polymer as depicted in scheme 2.1: (i) SCB_uniform where the short branches are uniformly distributed along the backbone, (ii) SCB_dumbbell where one-half of the short branches are located near one end of the backbone and the other half near another backbone end, and (iii) SCB_center where all the short branches are placed around the backbone center. The three representative SCB polymers were set to have the same molecular weight (corresponding to a total of 70 beads) and branch density (33%), which was appropriate to analyze the effects of short branches and the construction of the various types of molecular architectures of SCB polymers.

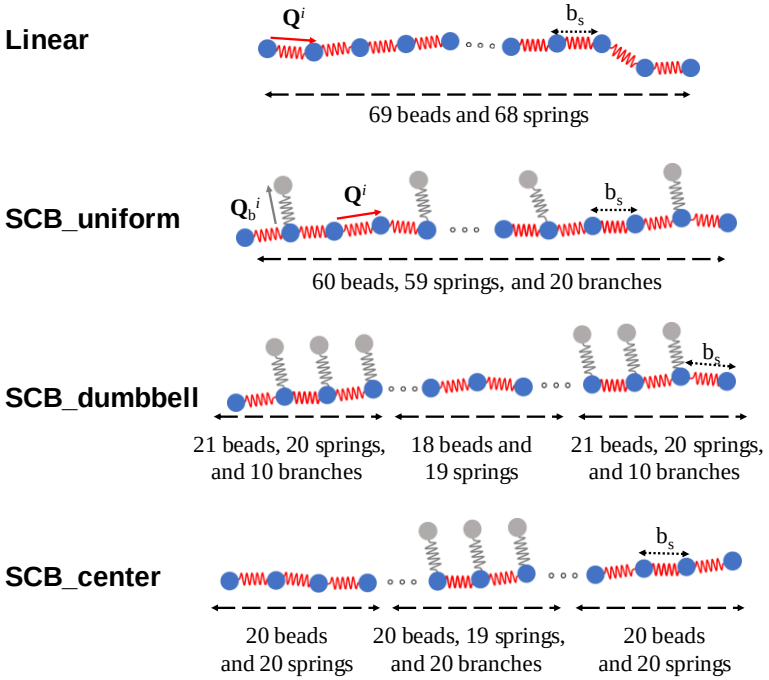


**Scheme 2.1** Simple molecular architecture schematics for the linear, SCB_uniform, SCB_dumbbell, and SCB_center polymers.

To examine the influence of the short chain branches on the LCB polymer, we chose two representative types of the short-chain branched H-shaped polymer systems with varying spatial distribution of short branches along the chain as depicted in scheme 2.2: (i) H-(SCB_arm) where the

ULSAN NATIONAL INSTITUTE OF SCIENCE AND TECHNOLOGY

short branches are evenly distributed along the four long arms of the H-polymer, and (ii) H-(SCB_backbone) where the short branches are uniformly distributed along the chain backbone of the H-polymer. Various rheological behaviors of each SCB H-polymer were analyzed in detail via a direct comparison with those of the original H-polymer [H-(original)] without short branches. For all three polymer systems, the length of the backbone and each of the four arms were fixed at 69 and 17 regular beads, respectively (corresponding to a total of 137 regular beads); i.e., thus, the ratio between the backbone and arm length was approximately equal to 4:1. The two SCB H-polymers were set to have a total of 32 short branches distributed along the backbone or arms [corresponding to ~23% (=32/137) short-branch number density]. That is, 32 short-branch beads were placed along the chain backbone for the H-(SCB_backbone) polymer and 8 short-branch beads along each of the four arms for the H-(SCB_arm) polymer.

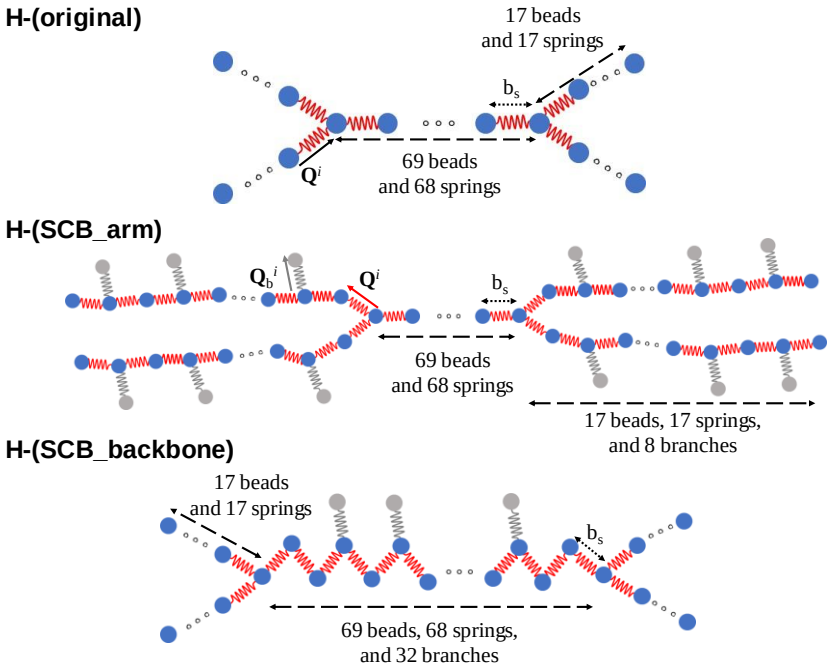


**Scheme 2.2** Simple molecular architecture schematics for the H-(original), H-(SCB_arm), and H-(SCB_ backbone) polymers.

On the basis of the fact that in the case of the polyethylene melt system short branches usually contain either 4 or 6 carbon atoms and the Kuhn segment for polyethylene chain contains about 12 carbon atoms, we devised the present coarse-grained bead-spring model where on branch bead corresponds to one-half regular (backbone) bead; i.e., for the present SCB systems, we chose one Kuhn segment composed of 12 $CH_2$ units for a bead in the backbone and long-chain branches, and one-half Kuhn segment composed of 6 $CH_2$ units for each branch bead. The magnitude of the branch mobility (specified by an adjustable parameter termed the "branch randomness factor (brfac)" that controls the characteristic relaxation time of short branches via the "$\tau_R$×brfac" in the evolution equation of connector

ULSAN NATIONAL INSTITUTE OF
SCIENCE AND TECHNOLOGY

vectors) was set to 0.05, which was determined to match the structural and rheological properties between the full atomistic and coarse-grained BD simulations for a representative SCB_uniform polymer system under shear. Note that a smaller value of "brfac" corresponds to a shorter characteristic relaxation time and thus a higher mobility of short branches.[23] The results derived for the SCB polymers were directly compared with those of the corresponding linear analogues. The bead-spring BD simulations for the linear and SCB polymers under shear and uniaxial elongational flow were carried out using finite extensible nonlinear elastic (FENE) force law, without including hydrodynamic interactions between the beads. In conjunction with the well-known fact that the Rouse model without including any contributions of hydrodynamic interaction (HI) and excluded volume (EV) describes well the linear viscoelastic behaviors for unentangled dense polymer solutions or melts where the effects of HI and EV are essentially negligible,[20] the results for polymeric systems modeled in this study can be qualitatively applied to unentangled polymer melts for which topological constraints (entanglement) between chains are ineffective. Because intermolecular interactions are no modeled, as in typical BD simulations for dilute solutions, the polymeric systems studied here are similar to untangled polymer melts, for which topological constraints (entanglement) between chains are ineffective.[25-29]

Further details of the simulation methodology are described in the Appendix and also the Supporting Information in refs. 22-24.

ULSAN NATIONAL INSTITUTE OF SCIENCE AND TECHNOLOGY

## 2.3 Results and Discussion

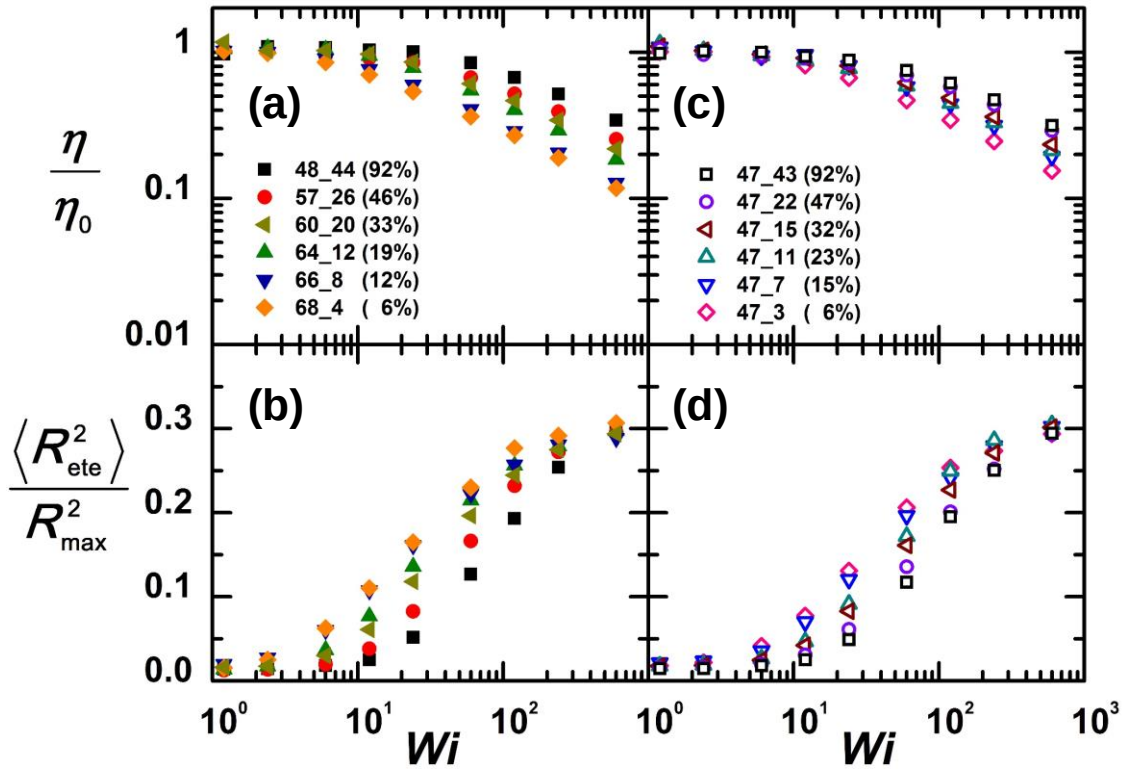


**Figure 2.1** Mean square chain end-to-end distance $\langle R_{ete}^2 \rangle$ and shear viscosity $\eta$ ($\equiv -\sigma_{xy}/\dot{\gamma}$ where $\sigma_{\alpha\beta}$ and $\dot{\gamma}$ denote stress tensor and applied shear rate, respectively) as a function of *Wi* for the SCB polymer systems with variable branch densities (the parentheses represent the percentage of the backbone portion covered by short branches). As for the numeric nomenclature shown in the figure legend, the first digit represents the number of beads contained in the backbone of a chain and the second digit the number of beads, each of which represents a short branch. Note that one branch bead corresponds to one-half backbone bead in the present coarse-grained model; e.g., for the SCB polymer denoted by "48_44", the total molecular weight of a chain corresponds to 70 (= 48 + 44×0.5) beads. The shear viscosity is normalized by the equilibrium value $\eta_0$ for each system, and $\langle R_{ete}^2 \rangle$ is normalized by the square of fully stretched length $R_{max}^2$ for each system.

We considered the influence of short-chain branching on the structural and rheological properties of the polymers by varying the branch density for two different cases: (i) one with the same total chain length (70 beads) and (ii) the other with the same backbone length (47 beads). In both cases, the short branches for all the SCB polymers were uniformly distributed along the backbone similar to the SCB_uniform as depicted in Scheme 2.1. For case (i), Figure 2.1a and 2.1b show the shear viscosity $\eta$ ($\equiv -\sigma_{xy}/\dot{\gamma}$ where $\sigma_{\alpha\beta}$ and $\dot{\gamma}$ denote stress tensors computed by well-known Irving-Kirkwood statistical-mechanical formula[30] and applied shear rate, respectively) and the mean-square chain end-to-end distance $\langle R_{ete}^2 \rangle$ based on the longest linear chain dimension(backbone) with various branch

ULSAN NATIONAL INSTITUTE OF SCIENCE AND TECHNOLOGY

densities as a function of the Weissenberg number *Wi* (defined as the product of the longest characteristic relaxation time of the system and the imposed strain rate).

As shown in Figure 2.1a, the SCB systems studied exhibit a typical shear-thinning behavior,[1] i.e., a decrease in the viscosity with increasing flow rate, and this thinning behavior is smaller for systems with higher branch densities. Because shear-thinning behavior is attributed to chain alignment and stretching toward flow (*x*-)direction, this result indicates that the degree of chain alignment and deformation in response to the flow weakness with increasing branch density at a given field strength. The structural characteristics associated with this rheological behavior are presented in Figure 2.1b, which presents that the variation of $\left\langle R_{\mathrm{ete}}^2 \right\rangle$ in response to the imposed flow strength becomes smaller with increasing branch density; i.e., chains with a higher branch density possess a more compact overall conformation and undergo less structural deformation against the external flow field. Altogether, these results demonstrate the strong influence of short branches on the overall structure and dynamics of polymer. As well known in recent studies,[22-24] the short branches generally execute the fast random thermal Brownian motions associated with their short characteristic relaxation time due to their very short chain length (e.g., 2, 4, and 6 carbon atoms in PE molecule).[5,31] It is therefore physically plausible that the fast motions in all directions executed by the short branches along the backbone generally tend to reduce the flow-induced alignment and structural deformation of chains away from their original (equilibrium) random orientation and random-coil conformation. The results presented in Figures 2.1a and 2.1b can be readily understood from this perspective.

Compared to case (i), Figures 2.1c and 2.1d show the corresponding structural and rheological result for case (ii) where the chain backbone length is constant. Similar to the trends shown for case (i), less shear thinning and structural deformation is evident for chains with higher branch densities for case (ii). This result can also be understood using the physical interpretation given earlier. Interestingly, for both cases (Figures 2.1b and 2.1d), the critical intermediate flow strength where $\left\langle R_{\mathrm{ete}}^2 \right\rangle$ begins to stretch rapidly increases for polymer systems with higher branch densities. The total resistive force of an SCB polymer chain against an external flow field is equal to the sum of all the individual contributions of short branches along the backbone. So, in this respect, it can be understood that the critical intermediate flow strength increases with increasing branch density.

ULSAN NATIONAL INSTITUTE OF SCIENCE AND TECHNOLOGY

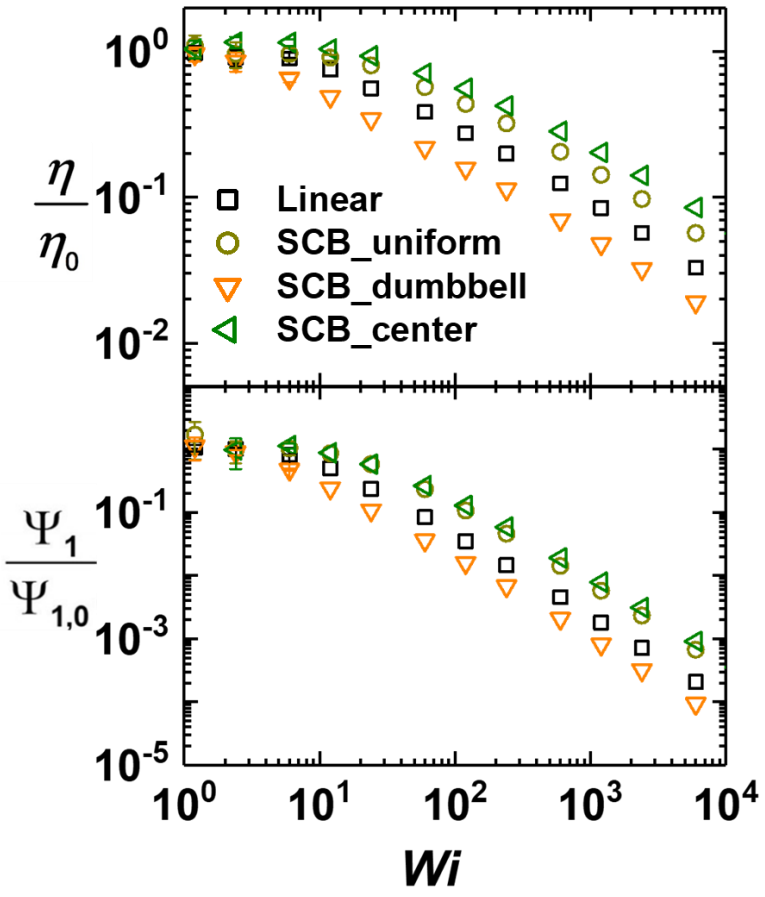


**Figure 2.2** (a) Shear viscosity $\eta$ (normalized by the equilibrium value $\eta_0$) and (b) the first normal stress coefficient $\Psi_1$ (normalized by the equilibrium value $\Psi_{1,0}$) as a function of *Wi* for the linear (black square), SCB_uniform (dark yellow circle), SCB_dumbbell (orange down triangle), and SCB_center (green left triangle) systems. All the linear and SCB chains have the same total molecular weight (70 beads). The error bars are smaller than the size of the symbols unless otherwise specified.

Extend from these fundamental physics of short branches, we have examined the structural and rheological influences of the molecular architecture of the SCB polymer by varying the distribution of the short branches along the backbone. Three representative SCB architectures are depicted schematically in Scheme 2.1: (i) SCB_uniform, (ii) SCB_dumbbell, and (iii) SCB_center. The branch density (33%) selected in this study was found to have a substantial effect on the structural and rheological responses of each type of SCB system studied. In Figure 2, we present the macroscopic rheological properties of shear viscosity $\eta$ and first normal stress coefficient $\Psi_1 \equiv -(\sigma_{xx} - \sigma_{yy})/\dot{\gamma}^2$ as a function of *Wi* for the linear, SCB_uniform, SCB_dumbbell, and SCB_center systems. Importantly, like the linear, all the SCB polymers exhibit a typical shear-thinning behavior in both viscosity and first normal stress coefficient[1], but the degree of shear-thinning was affected by the short branches and their attached sites (branching distribution) significantly.

ULSAN NATIONAL INSTITUTE OF SCIENCE AND TECHNOLOGY

Specifically, the SCB_uniform and SCB_center polymers display a less shear thinning than the linear analogue. This behavior is associated with the lower chain stretching and alignment in the flow direction at a given field strength, which arise from the strong random motions of the short branches. However, we also found that the SCB_center polymer showed a less shear-thinning behavior than the SCB_uniform polymer, indicating weaker chain deformations in the former compared to the latter. In sharp contrast, the SCB_dumbbell polymer exhibited a stronger shear-thinning behavior than the linear counterpart, indicating a larger degree of chain deformation and alignment of the SCB_dumbbell chains in response to the applied flow. All these findings indicate the significant effect of the short branches on the macroscopic rheological properties of polymers and provide useful information concerning the tuning of material properties by controlling the branching architecture (or branching distribution). By fitting the data within the shear-thinning regime to the standard power-law expression $\eta \sim Wi^{-b}$, the power-law index $b$ was calculated to be 0.41±0.02, 0.43±0.02, 0.46±0.01, and 0.51±0.01 for the SCB_center, SCB_uniform, linear, and SCB_dumbbell systems, respectively. These values are in accordance with the typical range $0.4 < b < 0.9$ obtained from experimental measurements for polymer melts. Similarly, the power-law index $b$ for $\Psi_1 \sim Wi^{-b}$ was found to be 0.95±0.03, 1.06±0.02, 1.16±0.02, and 1.23±0.01 for the SCB_center, SCB_uniform, linear, and SCB_dumbbell systems, respectively.[1]

ULSAN NATIONAL INSTITUTE OF SCIENCE AND TECHNOLOGY

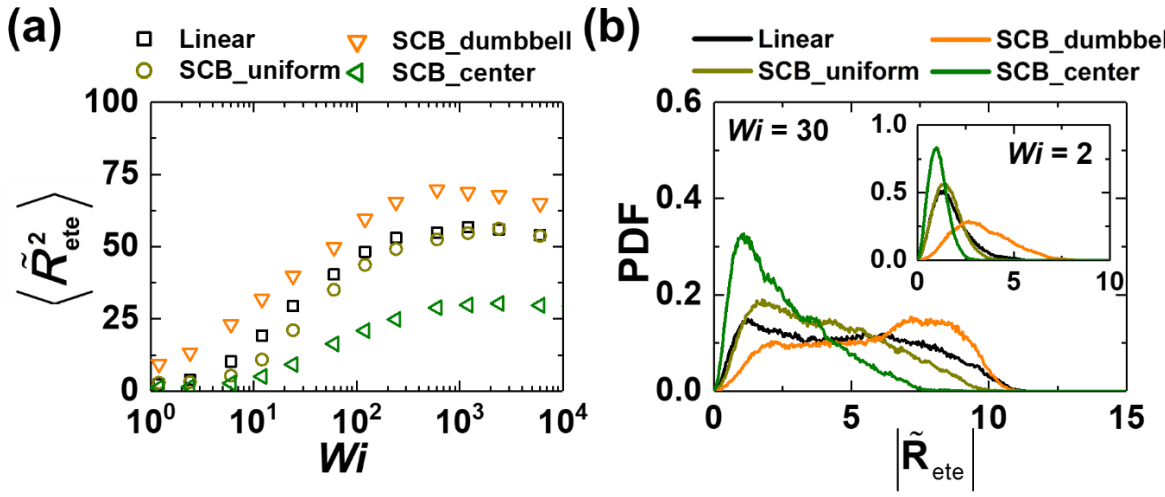


**Figure 2.3** (a) Mean-square chain end-to-end distance $\langle R^2_{ete} \rangle$ as a function of *Wi* and (b) the probability distribution function (PDF) of the chain end-to-end distance $|\mathbf{R}_{ete}|$ at a weak and an intermediate flow strengths, for the simulated linear, SCB_uniform, SCB_dumbbell, and SCB_center systems. The chain end-to-end distances are made dimensionless with $\langle \tilde{R}^2_{ete} \rangle = \langle R^2_{ete} \rangle$ ($K / k_B T$) and $|\tilde{\mathbf{R}}_{ete}| = |\mathbf{R}_{ete}| \sqrt{K / k_B T}$, where $K$, $k_B$, and $T$ denote the elastic spring constant, the Boltzmann constant, and temperature, respectively.

To help understanding the macroscopic rheological responses of the system, we have analyzed the variation in $\langle R^2_{ete} \rangle$ and the probability distribution function (PDF) of the chain end-to-end distance, $|\mathbf{R}_{ete}|$, with increases from low to intermediate values of *Wi* (indicative of the significant chain deformation induced by the applied flow) and attains a plateau value at high values of *Wi* via chain rotation and tumbling under shear.[32,33] The magnitude of $\langle R^2_{ete} \rangle$ is different for the polymer systems at a given flow strength. In case of the SCB_uniform and SCB_center polymers are smaller than those of the linear analogous. Notably, the $\langle R^2_{ete} \rangle$ value of the SCB_center polymer is only about half that of its linear counterpart in the intermediate-to-high flow regime. This is a remarkable structural characteristic of SCB_center polymer. In contrast, the SCB_dumbbell polymer exhibits much higher $\langle R^2_{ete} \rangle$ values than the linear and other SCB polymers over the whole range of *Wi*, indicative of its significantly larger chain stretching.

To further understanding the detailed structural characteristics, we also analyzed the PDF of $|\mathbf{R}_{ete}|$ for each system. At low *Wi* numbers (i.e., *Wi* = 2, shown in the inset of Figure 2.3b), the PDFs for all systems can be characterized as Gaussian-like around the equilibrium value of $|\mathbf{R}_{ete}|$. However, the PDF of the SCB_center polymer has a peak at a smaller value of $|\mathbf{R}_{ete}|$ with a narrower distribution

ULSAN NATIONAL INSTITUTE OF SCIENCE AND TECHNOLOGY

compared to that of the linear analogue; this indicates that the SCB_center polymer has a stiffer chain conformation (i.e., less deformation in response to the applied flow) compared to the linear polymer. In sharply contrast, the DPF of the SCB_dumbbell polymer has a smaller peak at a larger value of $|\mathbf{R}_{ete}|$ with a broader distribution than that of the linear polymer, indicating the more flexible (i.e., more deformation in response to the applied flow) structural characteristics of the SCB_dumbbell polymer. In addition, the SCB_uniform system has a somewhat stiffer chain conformation than that of the linear system. At an increased flow strength ($Wi$ = 30 in Figure 2.3b), the PDF profile of each system becomes substantially distorted from Gaussian shape near equilibrium, resulting from two effects: (i) chain extension in the flow direction and (ii) chain rotation and tumbling mechanisms on the vorticity plane. At this intermediate flow strength, the PDF of the linear polymer has a broad, flat distribution with two characteristic peaks: a rotation peak at low $|\mathbf{R}_{ete}|$ and a stretch peak at high $|\mathbf{R}_{ete}|$. In comparison, the PDF of the SCB_uniform polymer shows a declining ramp-shaped distribution without any distinctive stretch peak, and the overall weight of the PDF is skewed toward lower values of $|\mathbf{R}_{ete}|$, indicative of the more compact chain structure, which is again ascribed to the fast random motions of the short branches, rendering the chain backbone less stretchable against the applied flow. This feature is even more evident in the case of the SCB_center polymer, which exhibits a much stiffer chain conformation with a particularly large rotational peak.

In contrast, the PDF of the SCB_dumbbell system is characterized by a relatively weaker rotation peak at a higher value of $|\mathbf{R}_{ete}|$ and a stronger stretch peak at a larger value of $|\mathbf{R}_{ete}|$ than that of the corresponding linear system, indicating its less coiled and more stretched chain conformation with respect to the imposed flow field. These structural characteristics of the SCB polymers in comparison with the linear analogue are closely linked with the macroscopic rheological properties shown in Figure 2.2. That is, compared to that of the linear polymer, the reduced shear-thinning behaviors in the shear viscosity and the first normal stress coefficient displayed by the SCB_uniform and SCB_center polymers are associated with their less deformed chain structures in response to the applied flow, and the greater shear-thinning behavior of the SCB_dumbbell system is associated with larger chain deformations.

ULSAN NATIONAL INSTITUTE OF SCIENCE AND TECHNOLOGY

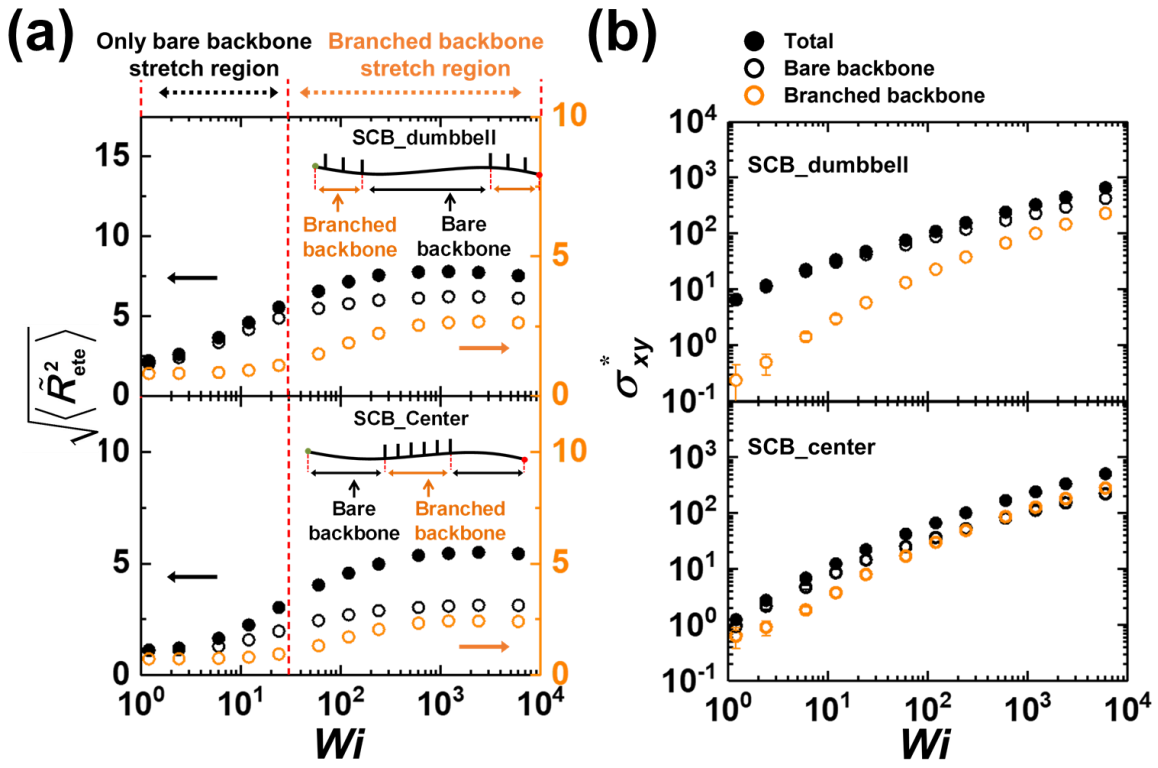


**Figure 2.4** (a) Root mean-square chain end-to-end distance $\left\langle R_{\mathrm{ete}}^2 \right\rangle$ of the whole backbone, the bare backbone part, and the branched backbone part as a function of *Wi* for the SCB_dumbbell (top panel) and SCB_center (bottom panel) systems. The vertical dotted line denotes the borderline between the two characteristic flow regimes: in the first regime (*Wi* < 30), only the bare backbone stretches, whereas in the second regime (*Wi* > 30), both the bare and branched backbone parts stretch. The horizontal arrows direct the proper *y*-axis of data points that have the same color. The chain end-to-end distance is made dimensionless likewise the same in Figure 2.3. (b) Shear stress $\sigma_{xy}$, contributions of the whole chain (black filled circle), the bare backbone (black open circle), and the branched backbone (orange open circle) for the SCB_dumbbell (top panel) and SCB_center (bottom panel) systems. The shear stress is made dimensionless with $\tilde{\sigma}_{xy} = \sigma_{xy}\sqrt{k_B T / K^3}$. The error bars are smaller than the size of the symbols unless otherwise specified.

The SCB polymers with a nonuniform branching architecture (e.g., SCB dumbbell and SCB_center) can be mapped into a sort of block copolymer, and the backbone part which is covered with short branches (the branched backbone) has distinct structural and dynamical characteristics from those of the backbone part without short branches (the bare backbone). Thus, representing the branched backbone as block "A" and the bare backbone as block "B", various molecular architectures of the nonuniform SCB polymers can be described as types of block copolymer comprising two kinds of monomer. For instance, the SCB_dumbbell and SCB_center polymers can be represented as "A-B-A" and "B-A-B" triblock copolymers, respectively.

In this respect, we analyzed the contributions of the bare and branched backbone parts to the structural and rheological properties. Figure 2.4a plots the variation of the root mean-square chain end-

ULSAN NATIONAL INSTITUTE OF SCIENCE AND TECHNOLOGY

to-end distance $\left\langle R_{ete}^2 \right\rangle$, with the imposed flow strength for the SCB_dumbbell and SCB_center. For *Wi* < 30, while there is a steep increase in $\left\langle R_{ete}^2 \right\rangle$ for the bare backbone with increasing shear rate, very little change in $\left\langle R_{ete}^2 \right\rangle$ is seen for the branched backbone, suggesting a rather compact configuration of the branched part, similar to those observed under equilibrium conditions. Therefore, the overall chain stretch of the SCB_dumbbell under shear in this flow regime is mainly associated with the extension of the bare backbone rather than the branched part. In the flow range of *Wi* > 30, $\left\langle R_{ete}^2 \right\rangle$ for the bare backbone increases rather slowly with increasing shear rate, reaching a plateau at *Wi* ≈ 200. In contrast, the branched backbone begins to stretch considerably with increasing flow field, approaching a plateau region at much higher field strengths (i.e., *Wi* ≥ 1000). Therefore, in this intermediate-to-high flow regime, the overall chain extension of the SCB_dumbbell polymer arises from the contributions of both the stretched bare- and branched backbone sections. Interestingly, compared to the SCB_dumbbell, the SCB_center polymer has similar behaviors of branched backbone and bare backbone depending on increasing shear rate. These results directly demonstrate that the role of short branches is not changing even when the distributed position is different. The bare backbone parts of the SCB_center exhibit a relatively slower increase in $\left\langle R_{ete}^2 \right\rangle$ than those of the SCB_dumbbell, indirectly indicative of additive tensile force on SCB_dumbbell due to the branched end parts.

The results from a similar analysis of the shear stress $\sigma_{xy}$ for the SCB_dumbbell and SCB_center systems are presented in Figure 2.4b. For *Wi* < 30, most of the total shear stress of each system is from the bare backbone with only a minor contribution from the branched part [note that the trend of increasing $\sigma_{xy}$ for the branched backbone is largely associated with the chain orientation (the *xy*-orientational correlation) in the flow (*x*-)direction without any significant chain stretching, as shown in Figure 2.4a]. This negligible stress contribution from the branched backbone is again ascribed to its compact structure being less vulnerable to deformation in response to the imposed flow because of the strong resistance against the field exerted by the highly mobile short chains. In addition, in the case of SCB_dumbbell, the large-scale hydrodynamic friction carried by each of the two branched backbone parts located around the backbone ends creates a tensile force pulling the middle part of backbone ends creates a tensile force pulling the middle part of backbone in opposite directions, resulting in orientation in the flow direction and increased stretching of the bare backbone, thus increasing the total stress of system. From the perspective of block copolymer, the two “A” blocks located at either end of the two chain ends are believed to have a tightly coiled compact structure due to the random motions exerted by the short branches. As such, the compact “A” blocks can be considered as superbeads with a large hydrodynamic bead friction, producing an effective tensile force on the “B” block positioned in the middle of the chain backbone, thus leading to a large-scale chain stretch. This physical aspect is

ULSAN NATIONAL INSTITUTE OF
SCIENCE AND TECHNOLOGY

consistently mirrored in the largely extended chain conformation and stronger shear-thinning behavior of viscosity.

In sharply contrast, the “A” block in the middle of the SCB_center polymer (which is a type of “B-A-B” type of triblock copolymer) is leading a very small-scale hydrodynamic friction of the two “B” blocks (bare backbone parts). Similarly, the "A" block in the SCB_center also having a tightly coiled compact structure due to the short branches, and it behaves like a superbead. However, different from the SCB_dumbbell, the superbead in the middle of the chain backbone constantly disturbs the alignment and stretch of the overall chain structure. It is mirrored in the small-scale hydrodynamic friction of the total and bare backbone part and compact structure properties in Figure 2.4b and 2.3, respectively. The detailed dynamics mechanisms of individual chains for each polymeric system underlying these structural and rheological properties are discussed later (Figure 2.6).

ULSAN NATIONAL INSTITUTE OF SCIENCE AND TECHNOLOGY

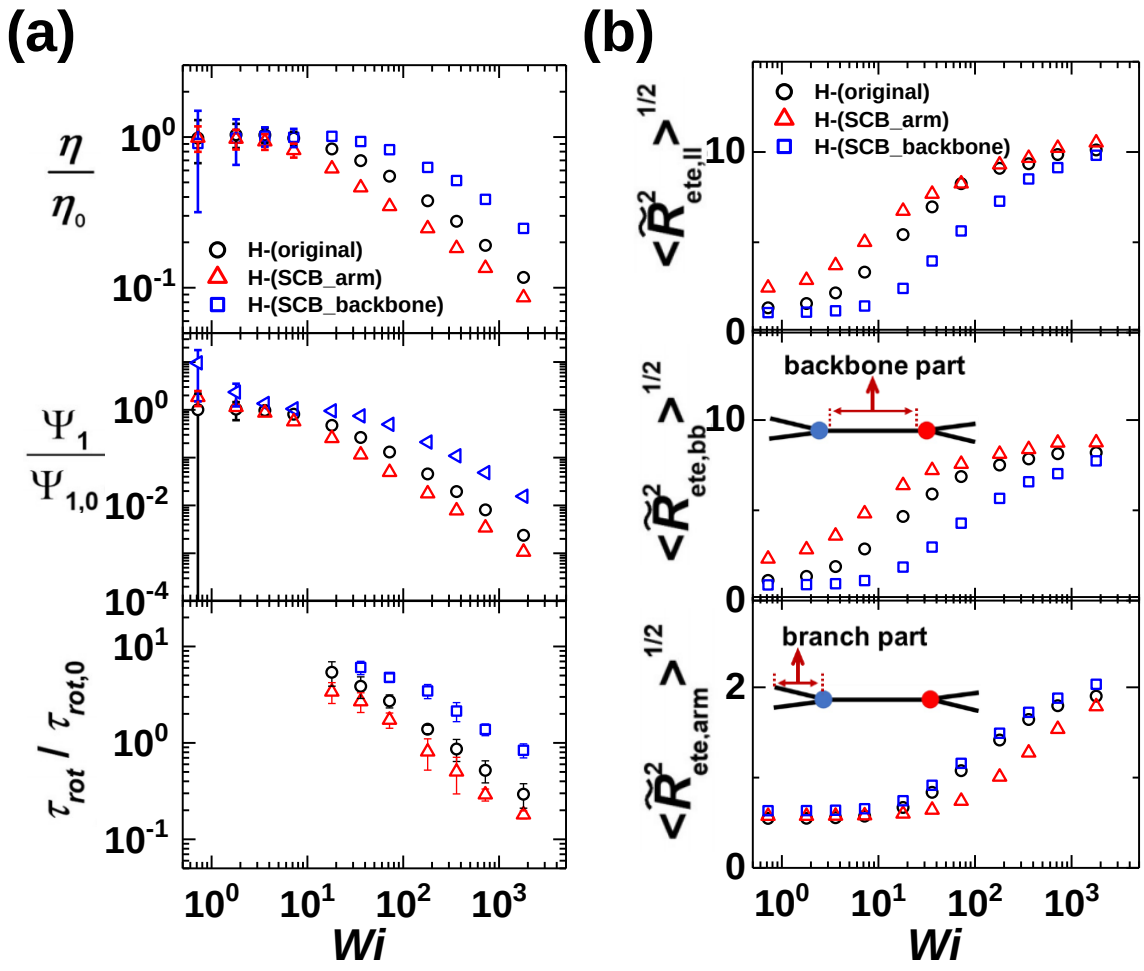


**Figure 2.5** (a) viscosity $\eta$ (normalized by the equilibrium value) (top panel), the first normal stress coefficient $\Psi_1$ (normalized by the equilibrium value) (middle panel), and rotation time (normalized by the equilibrium value) (bottom panel) as a function of *Wi* for the H-(original) (black circle)), H-(SCB_arm) (red triangle), and H_(SCB_backbone) (blue left triangle). Here rotation time was computed by the power spectral density (PSD) analysis through Fourier transformation of the time autocorrelation function $\langle \mathbf{u}(t)\cdot\mathbf{u}(0)\rangle$ where $\mathbf{u}(t)$ represents the unit backbone end-to-end vector. (b) Root mean-square chain end-to-end distance of the longest linear chain dimension $\langle R^2_{\text{ete,ll}}\rangle$ (top panel), the backbone $\langle R^2_{\text{ete,bb}}\rangle$ (middle panel), and the arm $\langle R^2_{\text{ete,arm}}\rangle$ (bottom panel). The backbone and arm parts are schematically indicated by the inset. The chain end-to-end distance is made dimensionless likewise the same in Figure 2.3.

Extend from the linear backbone, to examine the influence of the short branches on the structural and rheological behaviors of LCB polymeric systems under shear flows, we also have examined the short-chain branched LCB polymers. Three representative LCB architectures are depicted schematically in Scheme 2.2: (i) H-(original), (ii) H-(SCB_arm), and (iii) H-(SCB_backbone).

Figure 2.5a shows the variation of shear viscosity as a function of the *Wi*. It is noted that since the main purpose in this study is to examine the distinctive rheological behaviors of the H-(SCB)

ULSAN NATIONAL INSTITUTE OF SCIENCE AND TECHNOLOGY

polymers with varying the branching architecture of short branches along the backbone or arms, we employed $\tau_R$ of H-(original) polymer as a reference in defining the *Wi* number for all systems. Taking $\tau_R$ of the H-(original) polymers as a reference, the shifting factor in *Wi* was estimated as 1.5, 1. And 0.33 for the H-(SCB_arm), H-(original), and H-(SCB_backbone) polymers, respectively. The variation of relaxation time with short-chain branching architectures indicates the significant role of highly mobile short branches in determining overall chain structures and dynamics under equilibrium and non-equilibrium conditions, which will become clear in the main results. While all three H-polymer systems display a typical shear-thinning behavior (i.e., a decrease in the viscosity with increasing shear rate),[1] the H-(SCB_backbone) polymer exhibits a considerably lower degree of shear-thinning behavior compared to the H-(original) polymer. Further, the shear thinning begins at a higher *Wi* number for the H-(SCB_backbone) than the H-(original) polymer. This phenomenon is attributed to the relatively less degree of chain alignment and structural deformation for the H-(SCB_backbone) polymer at a given flow strength. In contrast, the H-(SCB_arm) polymer shows a higher degree of shear-thinning behavior than the H-(original), indicative of its more flexible structural characteristic, vulnerable to chain orientation and deformation in response to the applied flow. Consistent behaviors are further seen in the first normal stress coefficient and the characteristic rotational time of system as a function of *Wi* number in Figure 2.5a. By fitting the data within the shear-thinning regime to the standard power-law expression $\eta \sim Wi^{-b}$, the power-law index *b* was calculated to be 0.38±0.02, 0.41±0.01, and 0.34±0.02 for the H-(original), H-(SCB_arm), and H-(SCB_backbone), respectively. These values are in accordance with the typical range $0.4 < b < 0.9$ obtained from experimental measurements for polymer melts. Similarly, the power-law index *b* for $\Psi_1 \sim Wi^{-b}$ was found to be 1.07±0.02, 1.16±0.01, and 0.96±0.02 for the H-(original), H-(SCB_arm), and H-(SCB_backbone) systems, respectively.

In association with these rheological aspects, Figure 2.5b shows the variation of chain dimension with applied shear rate in terms of the root mean-square chain end-to-end distance based on the longest linear chain dimension $\left\langle R^2_{\text{ete,ll}} \right\rangle$ (containing 103 beads) (top panel). It is clear that in comparison with the H-(original) polymer, the H-(SCB_backbone) polymer exhibits smaller values of $\left\langle R^2_{\text{ete,ll}} \right\rangle$ whereas the H-(SCB_arm) polymer displays larger values of $\left\langle R^2_{\text{ete,ll}} \right\rangle$ whereas the H-(SCB_arm) polymer displays larger values of $\left\langle R^2_{\text{ete,ll}} \right\rangle$ in the whole range of flow strengths. All these results directly indicate the key effect of short branches on the overall structural and rheological properties of polymeric materials. As shown in previous studies and Figures 2.1 and 2.2, short branches generally execute the fast random thermal Brownian motions (irrespective of the practical flow fields) in association with their very short characteristic relaxation time scales due to their very short length.[5,31] Such highly mobile branches located along the backbone or arms constantly disturb the overall chain orientation and structure, leading to more compact and less deformed chain conformation against the

ULSAN NATIONAL INSTITUTE OF SCIENCE AND TECHNOLOGY

applied flow. This is further supported by the results for the average length of the chain backbone $\left\langle R^2_{\text{ete,bb}} \right\rangle$ and the arms $\left\langle R^2_{\text{ete,arm}} \right\rangle$, middle panel and bottom panel in Figure 2.5b, respectively. Evidently, $\left\langle R^2_{\text{ete,bb}} \right\rangle$ and $\left\langle R^2_{\text{ete,arm}} \right\rangle$ are the smallest for the H-(SCB_backbone) (for which short branches are located along the backbone) and H-(SCB_arm) (for which short branches are located along the arms) polymers, respectively.

As another interesting structural feature, the average backbone length appears quite larger for the H-(SCB_arm) polymer than for the H-(original) (middle panel, Figure 2.5b). This is attributed to the large-scale hydrodynamic friction carried by each of the four arms in conjunction with their tightly coiled compact "superbead" character that arise from the fast random motions of the attached short branches likewise SCB_dumbbell polymer in Figure 2.3. As such, the two SCB arms emanating from each of the backbone ends (branch or junction points) create an effective tensile force pulling out the backbone in opposite directions, resulting in an increased backbone stretch alongside with an increased chain orientation in the flow direction. This is consistently mirrored in the stronger shear-thinning behavior of the H-(SCB_arm) polymer shown in Figure 2.5a. Furthermore, the aforementioned delayed shear-thinning behavior for the H-(SCB_backbone) polymer in comparison to the H-(original) is directly associated with the delayed structural deformation of the SCB backbone (middle panel, Figure 2.5b). Additionally, it is noted that while the chain backbone stretches earlier than the arms for the H-(original) and the H-(SCB_arm) polymers via the hydrodynamic tensile force exerted on the backbone by the dangling arms, the backbone and arm stretch occur almost simultaneously in the case of the H-(SCB_backbone) polymer due to its delayed backbone deformation via the short-branch dynamics.

ULSAN NATIONAL INSTITUTE OF SCIENCE AND TECHNOLOGY

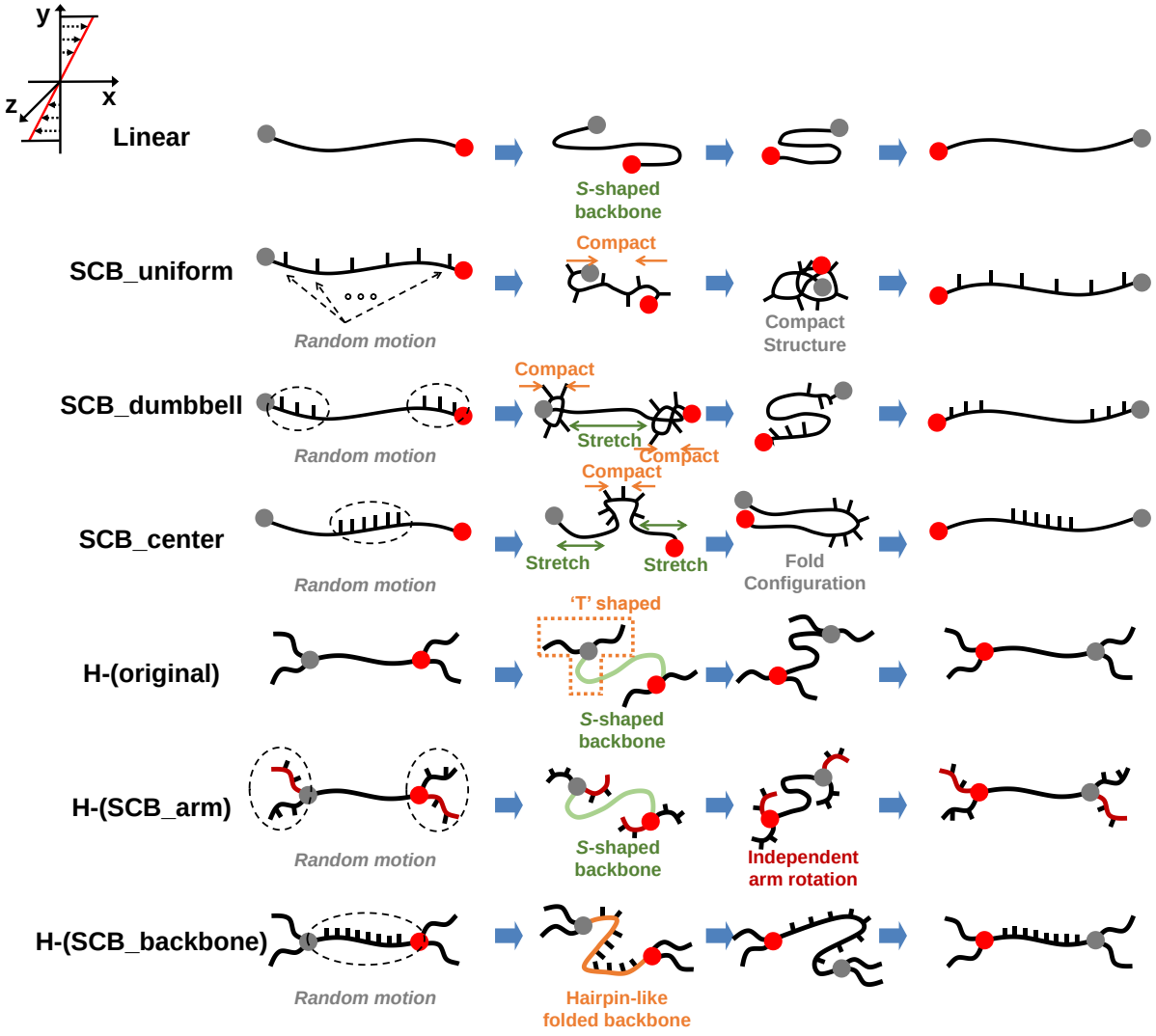


**Figure 2.6** Schematic illustrations for the fundamental molecular mechanisms underlying the rotational and tumbling dynamics of an individual chain for the linear, SCB_uniform, SCB_dumbbell, SCB_center, H-(original), H-(SCB_arm), and H-(SCB_backbone) systems under shear flow.

All the mesoscopic structural behaviors provide useful information on the chain rotation and tumbling dynamics for each system under strong flow fields. Knowledge of such molecular mechanisms is crucial to understanding the fundamental physics behind the apparently complex rheological properties and phenomena displayed by various polymeric materials with different molecular architectures.

Based on the structural and rheological characteristics revealed in this study, in Figure 2.6, we describe the representative rotational and tumbling mechanism characteristic of each polymer system schematically, which were obtained via analysis of the individual chain dynamics directly along the coarse-grained BD simulation trajectory. First, as for the linear polymer, we start from the most stable state of the chain conformation with orientation in the flow ($x$-)direction. When one or two free chain ends come into the shear ($xz$-)plane layered along the velocity gradient ($y$-)direction, which results in

ULSAN NATIONAL INSTITUTE OF SCIENCE AND TECHNOLOGY

the unfavorable alignment (the head part goes slowed down, the tail part accelerated, or both) of the chain end-to-end vector with respect to the flow (*x*-)direction, the chain undergoes a rotational movement that has an *S*-shaped or a hairpin-like conformation due to the different flow strengths along the velocity gradient (*y*-)direction. Eventually, this leads to an end-over-end tumbling dynamics[34-37] as seen in Figure 2.6. After that the chain end-to-end vector comes back into the region of stable positive orientation and aligns with the flow (*x*-)direction until the next rotation. The SCB_uniform polymer undergoes rotation mechanism similar to that of the linear polymer. However, the fast random motion of short branches in all directions results in a rather collapsed chain structure during the tumbling process. In addition, these random movements of the short branches are considered to frequently disturb the stable chain orientation, resulting in an unstable negative chain orientation and promoting the chain tumbling dynamics. At the same time, the random motion of the short branches is supposed to interrupt, to some extent, the chain rotation during the tumbling process. For the SCB_dumbbell polymer, we also expect an *S*-shaped or a hairpin-like tumbling behavior of the chain. However, the compact molecular structure of the two branched backbones near the backbone ends results in a stretched dumbbell configuration of the chain during the tumbling process. In the case of SCB_center, the situation is very different because of the location of the branched backbone in the middle of the backbone. We believe that the compact structure of the backbone center and the stretched configuration of the two outside bare backbone parts for the SCB_center polymer results in a hairpin-like fold (instead of an *S*-shaped) configuration of the chain during the tumbling process. Additionally, we expect a dynamical situation that because of the stiffer (and thus dynamically slower) chain structure in the middle of the backbone, the freely moving chain ends undergoing Brownian fluctuations often result in a negative orientation of the end-to-end vector, but without causing an actual chain tumbling cycle.

Compared to these linear backbone polymers, the H-(original) polymer exhibits an *S*-shaped (or a hairpin-like) rotational behavior for the backbone part, which is similar to that for the linear polymer. It is further noticed that the long arms of the H-(original) polymer, being aligned to the flow (*x*-)direction, rotate concurrently with the backbone. In comparison, while the H-(SCB_arm) polymer displays a similar *S*-shaped (or a hairpin-like) rotational behavior for the backbone, each SCB arm that is structurally compact due to the short branches exhibits a rather self-rotational movement without regard to the backbone motion. This independent rotational characteristic between the backbone and arms in the case of the H-(SCB_arm) polymer is clearly reflected in the uncorrelated variations between the backbone and arm lengths. Further interesting feature is observed for the H-(SCB_backbone) polymer, which exhibits a hairpin-like folded or a compact coiled (rather than an *S*-shaped) configuration for the backbone during the tumbling process, in association with the relatively more compact and rigid molecular structures of the SCB backbone against the flow. Furthermore, the arms, mostly being aligned to the flow direction with relatively large length (Figure 2.5b).

ULSAN NATIONAL INSTITUTE OF
SCIENCE AND TECHNOLOGY

To visualize the underlying molecular mechanisms of the tumbling dynamics of an individual chain, the readers are referred to the Supporting Information of included materials in this chapter,[23,24] in which movies of the representative polymers under shear are presented.

ULSAN NATIONAL INSTITUTE OF SCIENCE AND TECHNOLOGY

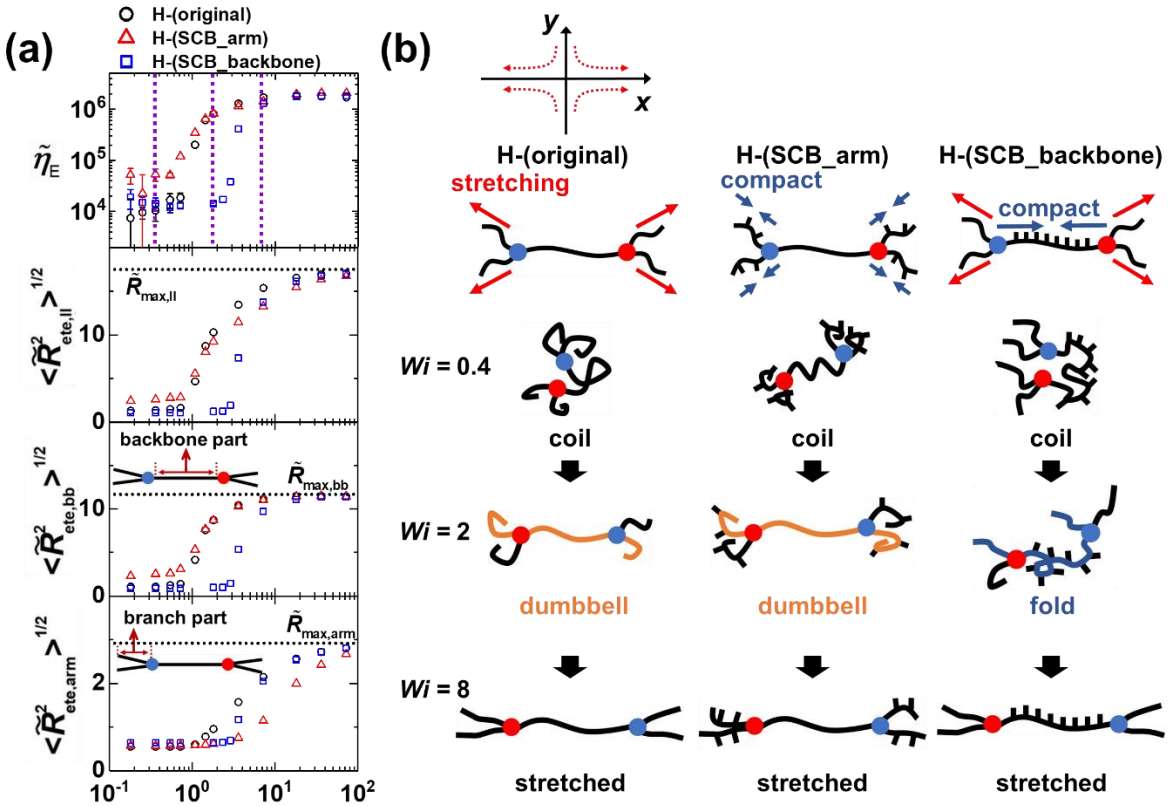


**Figure 2.7.** (a) Elongational viscosity $\eta_E$ [$\equiv -(\sigma_{xx}-\sigma_{yy})/4\dot{\varepsilon}$ where $\dot{\varepsilon}$ is the applied strain rate] and the root mean-square chain end-to-end distance of the longest linear chain dimension $\langle R^2_{ete,ll}\rangle$, the backbone $\langle R^2_{ete,bb}\rangle$, and the arm $\langle R^2_{ete,arm}\rangle$ as a function of *Wi* under uniaxial elongational flow. These chain end-to-end distances are made dimensionless likewise the same in Figure 2.3. The elongational viscosity is made dimensionless with $\tilde{\eta}_E = \eta_E(\sqrt{16\tilde{\tau}_R^2 k_B T/\zeta^2 K})$ where $\tilde{\tau}_R$ is the dimensionless Rouse time of the connector vector $\mathbf{Q}$. The horizontal dotted lines indicate the fully stretched length $\mathbf{R}_{max} = \mathbf{Q}\times(N_{bead}-1)$ of each dimension. (b) Simple schematics illustrating the dynamical features of the backbone and arms under elongational flow for H-(original), H-(SCB_arm), and H-(SCB_backbone) systems at the weak (*Wi* = 0.4), intermediate (*Wi* = 2), and high (*Wi* = 8) flow strengths. The vertical dotted lines in (a) indicate three representative (weak, intermediate, and high) flow strengths.

We now turn our attention to the rheological features of each H-polymer system in response to uniaxial elongational flow. As aforementioned, since the H-(SCB_arm) and H-(SCB_center) have very similar SCB architecture to the SCB_dumbbell and SCB_center, we only employed H-shaped polymers here. Figure 2.7a displays the elongational viscosity $\eta_E$ [$\equiv -(\sigma_{xx}-\sigma_{yy})/4\dot{\varepsilon}$ where $\dot{\varepsilon}$ is the applied strain rate] and the root mean-square chain end-to-end distance of the longest linear chain dimension $\langle R^2_{ete,ll}\rangle$, the backbone $\langle R^2_{ete,bb}\rangle$, and the arm $\langle R^2_{ete,arm}\rangle$ as a function of as a function of the imposed flow strength. It is evident that all the H-shaped polymers exhibit a typical tension-thickening behavior, i.e., an increase in the viscosity with increasing flow strength.

ULSAN NATIONAL INSTITUTE OF SCIENCE AND TECHNOLOGY

The elongational viscosity appears to be larger for the H-(SCB_arm) polymer and smaller for the H-(SCB_backbone), in comparison to that for the H-(original) polymer, especially in the low-to-intermediate flow regimes. This can be readily understood based on the stretching behavior of the backbone as depicted in Figure 2.7a. As expected, the backbone stretching for the H-(SCB_backbone) polymer is smaller than that for the H-(original) polymer via the random movements by the highly mobile short branches up to an intermediate flow strength ($Wi$ < 10), thus leading to a reduced elongational viscosity for the H-(SCB_backbone) system. In contrast, the backbone stretching for the H-(SCB_arm) polymer is higher than that for the H-(original) polymer in the weak flow regime, leading to an enhanced elongational viscosity; again, this is ascribed to a dominant effect of the large-scale hydrodynamic friction carried by the two SCB arms characterized as a superbead on each side of the backbone ends, which effectively creates a tensile force stretching out the backbone in opposite directions.

However, as the elongational flow strength increases, even the arms become increasingly extended. The stretched arm in the flow direction would exert a large hydrodynamic elongational (tensile) force on the backbone via the large $x$-direction streaming velocity at a given elongation rate. The arms located on the opposite sides of the backbone would therefore tend to stretch out the backbone. Consequently, the backbone stretch is influenced by the two distinct hydrodynamic tensile force (one associated with the superbead character of the compact SCB arm structure and another associated with the kinematically imposed flow-induced elongational force), both of which combine to give a total effective tensile force acting on the backbone. The flow-induced hydrodynamic force becomes large and comparable to the superbead-relative force as the arms get significantly stretched in the intermediate flow regime; this is well confirmed by the results shown in Figure 2.7a. Furthermore, under strong elongational flow fields, both the arms and the backbone, containing short branches, become fully stretched; as a result, all the three H-polymer systems exhibit a similar degree of chain deformation and elongational viscosity, as seen in Figure 2.7a. Incidentally, notice the overall very similar trend between elongational viscosity and $\left\langle R^2_{\mathrm{ete,bb}} \right\rangle$ in the whole range of flow strengths, indicative of a prominent role of the backbone stretch in determining rheological properties of LCB polymers under elongational flow.[15,21] Figure 2.7b shows the detailed molecular conformation schematics under uniaxial elongation.

Importantly, the critical flow strength appears to be larger for the H-(SCB_backbone) polymer incomparison to the H-(original) and H-(SCB_arm) polymers, due to the stronger structural resistance of the backbone against the imposed flow field via the fast random motions of short branches even under elongational flow.

ULSAN NATIONAL INSTITUTE OF
SCIENCE AND TECHNOLOGY

## 2.4 Conclusion

In this work, we carried out a comprehensive analysis of the effect of short- and long-chain branching on the structural and rheological properties by using bead-spring BD simulations with varying molecular architectures. Our results show that in comparison with the long-chain [linear and H-shaped polymers] polymers, the SCB polymers with uniformly (or randomly) distributed short branches along the backbone have a compact and less aligned molecular structure in response to the applied flow field, which is attributed to the fast random mobile of short branches. This resistive structural characteristic of the SCB polymer against the flow is found to increase with increasing branch density, irrespective of the total molecular weight or backbone length. The physical origin behind this behavior lies in the dynamical role of the short branches via their intrinsically fast random Brownian kinetics, which correspond to their very short characteristic relaxation time. These highly mobile short branches moving in all directions, reduce the degree of chain deformation and alignment with respect to the flow. This structural rigidity against a shear flow field leads to a less shear-thinning behavior in the shear viscosity and the firs normal stress coefficient for the SCB_uniform system compared with the linear analogue.

To explore the effect of the molecular architecture on the structural and rheological behaviors of the SCB system, we studied various types of SCB polymers with different distributions of short branches along the backbone. Compared with the linear and H-(original), the SCB_center and H-(SCB_backbone) polymers, which have short branches in the middle of the backbone, undergo a significantly lower chain deformation in response to the shear flow field. More importantly, the part analysis (compared the bare backbone part and branched backbone part) indicates that the fast dynamics of branched parts in the middle of the backbone constantly disturb the alignment of the overall backbone toward flow direction. This feature is consistently linked with the less shear-thinning behavior of those systems. This aspect inherent to the SCB_center and H-(SCB_backbone) polymers lead to distinctive chain rotation and tumbling mechanisms under shear, i.e., a hairpin-like fold configuration during tumbling process instead of an *S*-shaped configuration in the case of the linear and SCB_uniform polymers. In sharp contrast, the SCB_dumbbell and H-(SCB_arm) polymer chains, which have short branches in both end parts of the backbone, undergo significantly greater structural deformations at a given flow strength than the corresponding linear and H-(original), respectively. This is supposed to arise from a tensile force (which pulls out the middle part of the backbone in opposite directions) exerted by the branched backbone end parts separately located around the two ends of the backbone. Consistently, the SCB_dumbbell polymer exhibits a relatively weaker rotation peak and stronger stretch peak in the probability distribution with respect to the chain end-to-end distance, indicative of the flexible structural characteristic vulnerable to deformation by the flow. In conjunction with this, the SCB_dumbbell and H-(SCB_arm) polymers have a high shear-thinning behavior compared to the linear and H-(original) analogous, respectively. In line with these structural and rheological aspects, in

ULSAN NATIONAL INSTITUTE OF
SCIENCE AND TECHNOLOGY

comparison with the linear and H-(original) polymers, the SCB_dumbbell and H-(SCB_arm) polymers contain large portions of the stretched and dumbbell configurations and a significantly low content of the coil configuration over the whole range of flow strengths; this characteristic is consistently mirrored by the chain rotation and tumbling mechanisms. For instance, the H-(SCB_arm) polymer reveals highly independent (or uncorrelated) rotational behaviors between the backbone and the arms, in comparison to the H-(original) and H-(SCB_backbone) polymers. The SCB_dumbbell polymer exhibits similar behaviors to its.

Similar molecular features were further observed in the elongational flow field for the SCB H-polymer systems. The H-(SCB_backbone) polymer exhibits a weaker and delayed stretch behavior in the coil-to-stretch process of the backbone and the longest chain dimension as a function of *Wi*, in comparison to the H-(original). On the other hand, under the elongational flow, the backbone stretch of the H-(SCB_arm) polymer exhibits a steeper and faster stretch behavior than H-(original) polymer in the weak flow regime, leading to an enhanced elongational viscosity. Importantly, the fundamental role of short branches in determining the rheological properties of the linear and LCB polymers remains unchanged, irrespective of the flow type and strength applied in practice.

Although, currently, the findings in this study cannot be compared against experiment because of the lack of synthesis methods to prepare the well-defined SCB polymers studied here, we expect these polymers to have practical applications in the near future, especially considering the rapid experimental advances in catalysts and chemical synthesis that enable a precise control of the branch density and branching architecture. Present findings are considered to be beneficial in achieving our goal to manipulate material properties under various external flow field through a systematic alteration of the polymer molecular architecture.

ULSAN NATIONAL INSTITUTE OF SCIENCE AND TECHNOLOGY

## 2.5 References


[1] Bird R. B.; Armstrong R. C.; Hassager, O. *Dynamic of polymeric Liquids*; Wiley; New York, 1987; Vol. 1.

[2] Doi M.; Edwards, S. F. *The theory of polymer dynamics*; Clarendon Press; New York, 1986.

[3] Larson, R. G. *The structure and Rheology of Complex Fluids*; Oxford University Press; New York, 1999.

[4] Rubinstein M.; Colby, R. H. *Polymer Physics*; Oxford University Press; New York, 2003.

[5] Dealy J. M.; Larson, R. G. *Structure and rheology of molten polymers: from structure to flow behavior and back again*; Hanser Gardner Publications; Ohio, 2006.

[6] McLeish, T. C. B. Tube theory of entangled polymer dynamics. *Adv. Phys.* **2002**, *51*, 1379.

[7] Watanabe, H.; Matsumiya, Y.; van Ruymbeke, E.; Vlassopoulos, D.; Hadijichristidis, N. Viscoelastic and dielectric relaxation of a Cayley-tree-type polyisoprene: Test of molecular picture of dynamic tube dilation. *Macromolecules* **2008**, *41*, 6110.

[8] Robertson R. M.; Smith, D. E. Strong effects of molecular topology on diffusion of entangled DNA molecules. *Proc. Natl. Acad. Sci. U. S. A.* **2007**, *104*, 4824.

[9] Kapnistos, M.; Lang, M.; Vlassopoulos, D.; Phyckhout-Hintzen, W.; Richer, D.; Cho, D.; Chang T.; Rubinstein, M. Unexpected power-law stress relaxation of entangled ring polymers. *Nat. Mater.* **2008**, *7*, 997.

[10] Carlmark, A.; Hawker, C.; Hult, A.; Malkoch, M. new methodologies in the construction of dendritic materials. *Chem. Soc. Rev.* **2009**, *38*, 352.

[11] Voit, B. I.; Lederer, A. Hyperbranched and highly branched polymer architectures-Synthetic strategies and major characterization aspects. *Chem. Rev.* **2009**, *109*, 5924.

[12] Piel, C.; Starck, P.; Seppälä, J. V.; Kaminsky, W. Thermal and mechanical analysis of metalloscene-catalyzed ethene-*a*-olefin copolymers: The influence of the length and number of crystallizing side chains. *J. Polym. Sci., Part A: Polym, Chem.* **2006**, *44*, 1600.

[13] Kudo, H.; Makino, S.; Kameyama, A.; Nishikubo, T. Synthesis of cyclic polymers: Ring-expansion reaction of cyclic *S*-Dithioester with Thiiranes. *Macromolecules* **2005**, *38*, 5964.

[14] Hirao, A.; Kawasaki, K.; Higashihara, T. Synthesis of well-defined star-branched polymers by coupling reaction of star-branched polymer anions comprised of three polymer segments with chain-end-functionalized polystyrenes with a definite number of benzyl bromide moieties. *Macromolecules* **2004**, *37*, 5179.

[15] Bird, R. B.; Curtiss, C. F.; Armstrong, R. C.; Hassager, O. *Dynamics of Polymeric Liquids*, Vol. 2 Wiley: New York, 1987.

[16] de Gennes, P. G. *Scaling Concepts in Polymer Physics*; Cornell University Press; Ithaca, 1979.

[17] Rouse, P. E. A theory of the linear viscoelastic properties of dilute solutions of coiling polymers.

ULSAN NATIONAL INSTITUTE OF SCIENCE AND TECHNOLOGY

*J. Chem. Phys.* **1953**, *21*, 1272.

[18] Zimm, B. H. Dynamics of polymer molecules in dilute solution: viscoelasticity, flow birefringence and dielectric loss. *J. Chem. Phys.* **1956**, *24*, 269.

[19] de Gennes, P. G. Reptation of a polymer chain in the presence of fixed obstacles. *J. Chem. Phys.* **1971**, *55*, 572.

[20] Doi M.; Edwards, S. F. Dynamics of concentrated polymer systems. *J. Chem. Soc., Faraday Trans. 2: Molecular and Chemical Physics* **1978**, *74*, 1789; Part1, Part2, Part3, and Part4.

[21] McLeish, T. C. B. Tube theory of entangled polymer dynamics. *Adv. Phys.* **2002**, *51*, 1379.

[22] Kim, J. M.; Baig, C. Communication: Role of short chain branching in polymer structure and dynamics. *J.Chem.Phys.* **2016**, *144*, 081101

[23] Jeong, S. H.; Kim, J. M.; Baig, C. Rheological influence of short-chain branching for polymeric materials under shear with branch density and branching architecture. *Macromolecules* **2017**, *50*, 4491.

[24] Jeong, S. H.; Kim, J. M.; Baig, C. Rheological behaviors of H-shaped polymers incorporated with short branches under shear and elongational flows via FENE-Rouse model. *J. Rheol.* **2018**, *62*, 1115.

[25] Lopez Cascales, J. J.; Garcia de la Torre, J. Hydrodynamic interaction effects on the conformation of flexible chains in simple shear flow. *Macromolecules* **1990**, *23*, 809.

[26] Fetsko, S. W.; Cummings, P. T. Brownian dynamics simulation of bead-spring chain models for dilute polymer solutions in elongational flow. *J. Rheol.* **1995**, *39*, 285.

[27] Petera, D.; Muthukumar, M. Brownian dynamics simulation of bead-rod chains under shear with hydrodynamic interaction. *J. Chem. Phys.* **1999**, *111*, 7614.

[28] Sendner, C.; Netz, R. R. Single flexible and semiflexible polymers at high shear: Non-monotonic and non-universal stretching response. *Eur. Phs. J. E: Soft Matter Biol. Phys.* **2009**, *30*, 75.

[29] Kim, J. M.; Stephanou, P. S.; Endwards, B. J.; Khomami, B. A mean-field anisotropic diffusion model for unentangled polymeric liquids and semi-dilute solutions: Model development and comparison with experimental and simulation data. *J. Non-Newtonian Fluid Mech.* **2011**, *166*, 593.

[30] Irving, J. H.; Kirkwood, J. G. The statistical mechanical theory of transport processes. IV. The equations of hydrodynamics. *J. Chem. Phys.* **1950**, *18*, 817.

[31] Tukur, N. M.; Sharkh, B. F. A.; Osei-Twum, E. Y.; Hussein, I. A. Impact of short chain branching on conformations of metallocene LLDPE melts: NMR, light scattering and MD simulation study. *Macromol. Symp.* **2008**, *263*, 121

[32] Baig, C.; Edwards, B. J.; Keffer, D. J.; Cochran, H. D.; Harmandaris, V. A. Rheological and

ULSAN NATIONAL INSTITUTE OF SCIENCE AND TECHNOLOGY

structural studies of linear polyethylene melts under planar elongational flow using non-equilibrium molecular dynamics simulations. *J. Chem. Phys.* **2006**, *124*, 084902.

[33] Kim, J. M.; Keffer, D. J.; Kroger, M.; Edwards, B. J. Rheological and entanglement characteristics of linear-chain polyethylene liquids in planar Couette and planar elongational flows. *J. Non-Newtonian Fluid Mech.* **2008**, *152*, 168.

[34] Kim, J. M.; Edwards, B. J.; Keffer, D. J.; Khomami, B. Dynamics of individual molecules of linear polyethylene liquids under shear: Atomistic simulation and comparison with a free-draining bead-rod chain. *J. Rheol.* **2010**, *54*, 283.

[35] Teixeira, R. E.; Babcock, H. P.; Shaqfeh, E. S. G.; Chu, S. Shear thinning and tumbling dynamics of single polymers in the flow-gradient plane. *Macromolecules* **2005**, *38*, 581.

[36] Xu, Z.; Kim, S.; de Pablo, J. J. Anisotropic friction and excluded volume effects in freely jointed bead-rod polymer chain models. *J. Chem. Phys.* **1994**, *101*, 5293.

[37] Schroeder, C. M.; Teixeira, R. E.; Shaqfeh, E. S. G.; Chu, S. Characteristic periodic motion of polymers in shear flow. *Phys. Rev. Lett.* **2005**, *95*, 018301.

ULSAN NATIONAL INSTITUTE OF SCIENCE AND TECHNOLOGY

# III. Topological interaction and dynamic mechanisms of ring polymer solutions and melts under shear flow

***This chapter includes the materials from*:**

**Intrinsic surface characteristics and dynamic mechanisms of ring polymer solutions and melts under shear flow.**

**S. H. Jeong**†, S. Cho†, E. J. Roh†, T. Y. Ha†, J. M. Kim†, and C. Baig, Macromolecules, 53, 10051-10060, (2020).

---

## 3.1 Introduction

Over the past decades, numerous research has been carried out to understand the structural and rheological behaviors of closed-loop geometry called ring polymers in dilute solutions and melts.[1-4] Compared to linear polymers, which have free ends, the closed-loop geometry of ring polymers having no free ends brings up distinctive structural and dynamical properties. Practically, the ring-shaped structure of polymeric material is directly relevant to biological systems, and they serve as a model system for biophysical problems, such as chromatin packing in nucleosomes and circular plasmid DNA.[5-8] Generally, it is well known that the ring polymers possess a relatively compact structure than linear analogous, which is attributed to the no endpoints. For instance, in various experiments and simulations, the ring polymer exhibited an unusual chain-dimension scaling behavior with respect to molecular weight $M_w$, e.g., $1/3 \leq \nu \leq 0.4$ for the chain radius of gyration $R_g \approx M_w^{\nu}$, which is in sharp contrast to $\nu = 0.5$ for linear melts.[3,9-13] In association with this structural behavior, pure ring melts typically exhibit a smaller viscosity, faster relaxation, and larger diffusivity behaviors than linear analogous. Numerous theoretical approaches and models have also been supported these structural and dynamical behaviors, such as the Flory-like mean-field approach, lattice animal model, and crumpled globule model.[13-18] And also, in the perspective of the physical characteristics between different ring chains, such as concatenation or penetration, there were some theoretical and numerical works looking into the minimal surface area of ring polymers and the effective topological constraints.[19-23] Notably, the well-known theories, such as retraction, reptation, and tube theory, which describe the structural and rheological behaviors of entangled long-chain or linear polymer systems, cannot be applied to the ring system because of the absence of chain ends that need for reptation through a tube (one-dimensional curvilinear primitive path).

Recent nonequilibrium molecular dynamics (NEMD) simulation study for ring polymer melt under shear and planar elongational flows reported that ring polymers exhibit a stronger resistance to structural deformation against the flow field, leading to a definitively lower degree of chain stretch and alignment toward flow direction.[24] This feature results in less shear-thinning and extension-thinning behaviors for ring systems compared with their linear analogs.[24] Similar characteristics were observed

ULSAN NATIONAL INSTITUTE OF SCIENCE AND TECHNOLOGY

in experiments.[25,26] Another NEMD study showed that confined ring melts under shear flow exhibit a weaker interfacial (wall) slip in the weak-to-intermediate flow regime than the linear analogous.[27] This weaker slip behavior of ring polymer is attributed to the longer chain dimension of the ring polymers in the neutral (*z*-)direction at the wall, resulting in large polymer-wall friction. This study further revealed representative molecular mechanisms of ring polymer on the interfacial wall, such as loop wagging, loop migration, and loop tumbling dynamics. Other simulation studies have reported various distinctive dynamical mechanisms for ring chains, such as threading (or penetration) dynamics,[21,22] tank-treading dynamics,[28,29] and hydrodynamic inflation.[26,30-33] Other coarse-grained NEMD simulations using the Kremer–Grest model for ring melts under uniaxial extensional flow showed the formation of supramolecular rings linked with multiple individual ring chains, resulting in a distinctively high strain-hardening of viscosity, as reported in previous experiments.[34,35]

These distinctive and significant features of ring polymers originate from the intrinsic topological constraints of the closed-loop geometry. Despite numerous experiments and numerical studies, the general structural behaviors and dynamical mechanisms of ring polymer under a nonequilibrium state have not yet been fully understood. Here, to comprehensively analyze and find the representative mechanisms of ring polymers, we focus on revealing the physics origin of the structural and dynamical features of ring polymers under shear flow. For this, we carried out detailed atomistic NEMD simulations of ring melts and coarse-grained bead-rod Brownian dynamics (BD) simulations of dilute ring solutions undergoing steady shear flow. Based on the closed molecular geometry, which could be separating inside and outside, we have suggested a new viewpoint that ring polymers possess intrinsic two-dimensional surfaces in contrast with linear polymers that form one-dimensional lines. From this perspective, we: (i) proposed representative physical measures that can effectively characterize the general ring structures and dynamics; (ii) developed an efficient numerical scheme that allowed us to accurately measure various complex curved surfaces formed by flexible ring polymers; and (iii) analyzed the fundamental dynamical mechanisms of ring chains under shear flow and quantified them with respect to the flow strength and intermolecular interactions.

ULSAN NATIONAL INSTITUTE OF SCIENCE AND TECHNOLOGY

## 3.2 System studied and Method

A monodisperse $C_{400}H_{800}$ (unconcatenated) ring polyethylene (PE) melt system were employed for the atomistic NEMD simulations, which were performed at a constant temperature $T$ = 450K and density $\rho$ = 0.764 g cm$^{-3}$ (corresponding to a pressure $P$ = 1 atm) by using the $p$-SLLOD equations of motion,[36] implemented by the Nosé-Hoover thermostat.[37,38] The standard Lees-Edwards sliding-brick boundary conditions were used for the shear flow.[39] The set of equations of motion in the NEMD simulation was numerically integrated using the reversible reference system propagator algorithm ($r$-RESPA)[40] with two different time scales: 0.47 fs for three bonded (bond-stretching, bond-bending, and bond-torsional) interactions and 2.35 fs for two nonbonded inter- and intramolecular Lennard–Jones (LJ). The well-known Siepmann-Karaboni-Smit (SKS) united-atom potential model[41] was adopted for all the NEMD systems except that the original rigid bond was replaced by a flexible one with harmonic potential. A sufficiently large number of molecules (162 chains) were used in the NEMD simulations with a box dimension of 260.7 Å × 86.9 Å × 86.9 Å ($x \times y \times z$) where the $x$-, $y$-, and $z$-directions were chosen as the flow, velocity gradient, and neutral directions, respectively. The box dimension was enlarged in the flow ($x$-)direction to avoid any system-size effects, especially at high-flow fields where the chains are highly aligned and stretched in the flow direction. The box dimensions in the $y$- and $z$-directions were more than three times the chain radius of gyration $R_g \approx 22$ Å of the system at equilibrium.

A dilute ring solution system devoid of intermolecular interactions was investigated via standard coarse-grained BD simulations[42] [including the excluded volume (EV) and hydrodynamic interaction (HI) effects] for a bead-rod chain containing 66 beads connected by rigid rods. The Week-Chandler-Andersen Lennard-Jones model[43] and Rotne-Prager-Yamakwa tensor[44,45] were adopted to account for the EV and HI effects, respectively. According to a previous study,[46] one rod approximately corresponds to 6 $CH_2$ atoms for PE molecules in shear flow, thus the bead-rod ring chain roughly matches $C_{400}H_{800}$. The evolution of the dilute system was described by a diffusion equation with generalized coordinates via an equivalent stochastic differential equation derived by Öttinger.[42,47] The stochastic differential equation in the bead-rod BD simulations was numerically integrated with incorporating the iterative method of Liu.[48]

Both the dilute and melt ring systems were subjected to a steady shear flow over a wide flow strength range, corresponding to a Weissenberg number $Wi \equiv \tau_R \dot{\gamma}$ (the product of the longest relaxation time $\tau_R$ of the system and the applied shear rate $\dot{\gamma}$) for $0 \le Wi \le 1000$ with $\tau_R$ = 9.8 ± 0.4 ns and $\tau_R$ = 218 ± 10 ns for $C_{400}$ ring and linear PE melts, respectively, and $\tau_R$ = 63.3 ± 1.0 $\xi a^2 / k_B T$ and $\tau_R$ = 124 ± 2.0 $\xi a^2 / k_B T$ for the dilute ring and linear systems, respectively. The $\tau_R$ of each system was estimated by the integral below the stretched-exponential curve describing the decay of the time autocorrelation function of the unit chain end-to-end vector for linear polymers and the unit ring diameter vector for ring polymers.[24] $\xi$ and $a$ denote the bead friction coefficeint and the rod length,

ULSAN NATIONAL INSTITUTE OF
SCIENCE AND TECHNOLOGY

respectively. $k_B$ and $T$ represent Boltzmann's constant and termperature, respectively. A detailed comparison was made between the atomistic NEMD simulations of the ring melt and the BD simulations of the dilute ring systems for various structural and dynamical properties. The results provide useful information that can be used to predict the structural and dynamical characteristics of semi-dilute polymer solutions with respect to the polymer concentration. Additional details of the models and simulation methods are described in the Supporting Information. Additional details of the models and simulation methods are described in the Appendices 2 and 3.

ULSAN NATIONAL INSTITUTE OF SCIENCE AND TECHNOLOGY

## 3.3 Results and Discussion

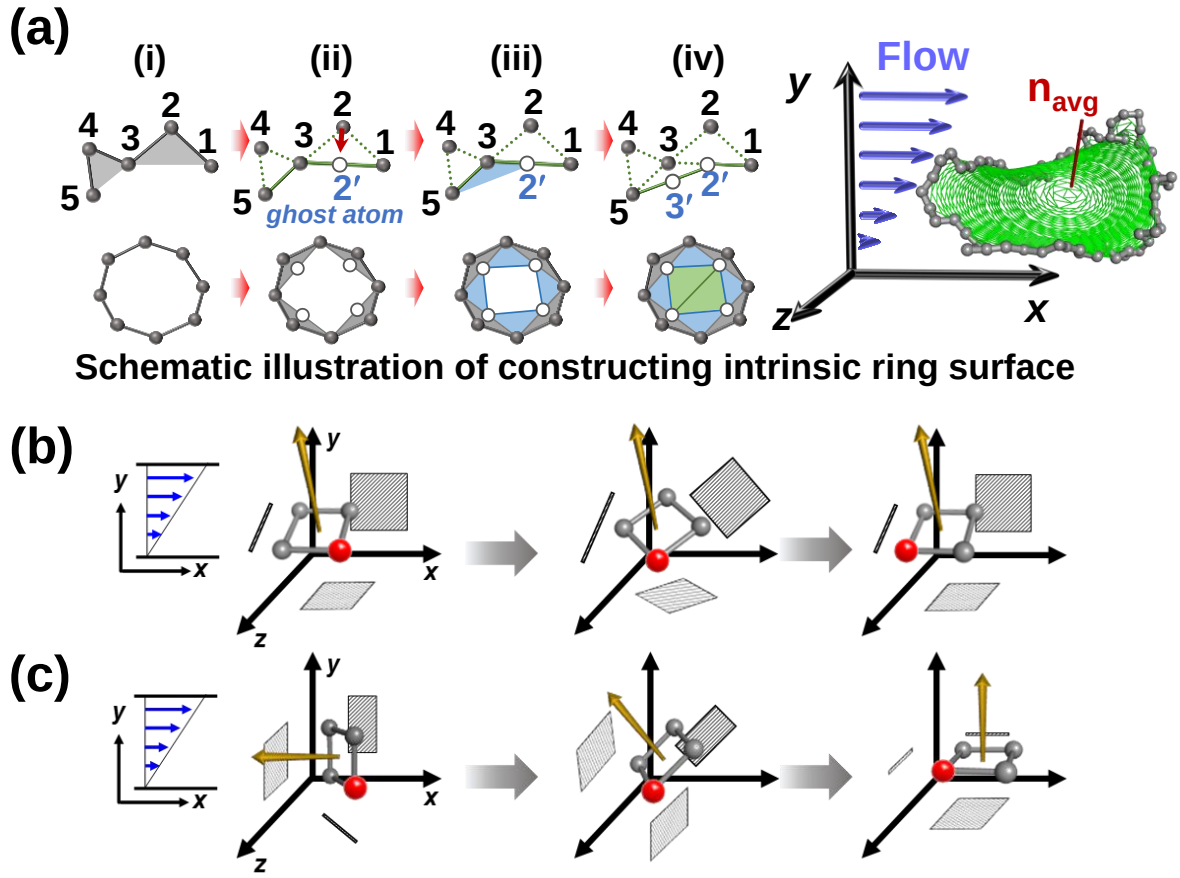


**Figure. 3.1** (a) Simple schematic description of the intrinsic surface constructing algorithm for the ring polymer. Rotational illustrations of the toy model under shear flow without the Brownian random force: (b) When there is no surface area facing the *yz*-plane at the initial state. (c) When there is non-zero surface area facing the *yz*-plane at the initial state. The yellow arrows in the illustrations indicate the normal vector of the toy model.

Starting from the viewpoint that the ring polymer, with its closed molecular geometry, naturally defines an intrinsic two-dimensional topological surface, we devised a simple and efficient numerical algorithm that could accurately describe the geometrically complex curved surfaces exhibited by flexible ring polymers. Figure 3.1a illustrates the main steps of the algorithm and how it allows for the extraction of the characteristic surfaces of the ring chains. Specifically, (i) we start to construct all the non-overlapping local triangular planes, each of which are constituted by three consecutive neighboring atoms (or beads) along the ring backbone; these triangles effectively depict the outermost ring surface. (ii)-(iv) We then apply the same procedure to successively build the inner surfaces of the ring in a step-by-step manner by forming new triangles with the remaining active atoms (which define a new inner closed-loop), excluding the middle (apex) atoms of the previous triangles. Here, to accurately extract the geometrical surfaces of the rings, ghost atoms were added in the middle of each line if the line connecting two neighboring atoms was longer than the original bond length. This

ULSAN NATIONAL INSTITUTE OF SCIENCE AND TECHNOLOGY

procedure was repeated until only three atoms remained at the end to form the last triangle. This simple algorithm was numerically fast and could properly represent a variety of geometrically complex surfaces formed by ring polymers, as exemplified in snapshot of Figure 3.1a.

From the constructed ring surface composed of numerous (locally-planar) small triangles, we obtained detailed geometric information of the ring in three-dimensional space, including the intrinsic surface shape and surface area. In particular, we could readily determine a set of the local normal vectors corresponding to each triangle over the entire ring surface. Here, we propose the average normal vector $\mathbf{n}_{\text{avg}}$ of the entire surface as a useful physical measure that can effectively characterize the global orientation of a ring chain. The chain end-to-end vector $\mathbf{R}_{\text{ete}} = \sum_{i=1}^{N_b} \mathbf{r}_i = N_b \left( \sum_{i=1}^{N_b} \mathbf{r}_i \Big/ N_b \right)$ with each bond vector $\mathbf{r}_i$ and total number of local bonds $N_b$ geometrically represents the average bond vector for the whole one-dimensional linear chain; while $\mathbf{n}_{\text{avg}} = \sum_{i=1}^{N_s} \mathbf{n}_i = N_s \left( \sum_{i=1}^{N_s} \mathbf{n}_i \Big/ N_s \right)$ with each surface normal vector $\mathbf{n}_i = \mathbf{r}'_{ia} \times \mathbf{r}'_{ib}$ for two bond vectors $\mathbf{r}'_{ia}$ and $\mathbf{r}'_{ib}$ constituting a triangle and the total number of local triangular surfaces $N_s$ represents the average surface normal vector for the entire two-dimensional surface formed by a ring chain (Figure 3.1a). Therefore, the $\mathbf{n}_{\text{avg}}$ of the ring polymer that defines the two-dimensional characteristic surface is considered to intrinsically correspond with $\mathbf{R}_{\text{ete}}$ for the linear polymer. Additionally, the magnitudes of $\mathbf{r}_i$ and $\mathbf{n}_i$ geometrically represent the local bond length and local triangular surface area ($=|\mathbf{n}_i|/2$), respectively. We demonstrate that these surface properties are very useful for analyzing the fundamental structural and dynamical characteristics of ring polymers under flow conditions.

Next, we analyze the basic structural characteristics of the surface orientation and stretch for ring systems under shear flow. For an in-depth understanding of the fundamental aspects of actual ring polymers, we first set up a simple 'toy model' with a fixed two-dimensional flat square surface comprising four beads and rigid rods, simply mimicking a closed-loop geometry of ring polymers (see Figures 3.1b and 3.1c). This model was analyzed by applying free-draining (without EV and HI) bead-rod BD simulations. From the BD simulations, it can be clearly seen that the rigid surface tends to lie down preferentially in the *xz*-plane. Furthermore, the simulations without random thermal noise show that the most stable position of the two-dimensional surface is the lying position in the *xz*-plane, except for certain special initial surface orientations (To visualize the underlying molecular mechanisms, the readers are referred to the Supporting Information of included material in this chapter). While the geometric surface formed by the actual flexible ring polymers is generally curved and much more complex, their fundamental orientational characteristics are considered to be essentially similar to those of the aforementioned rigid structure.

ULSAN NATIONAL INSTITUTE OF SCIENCE AND TECHNOLOGY

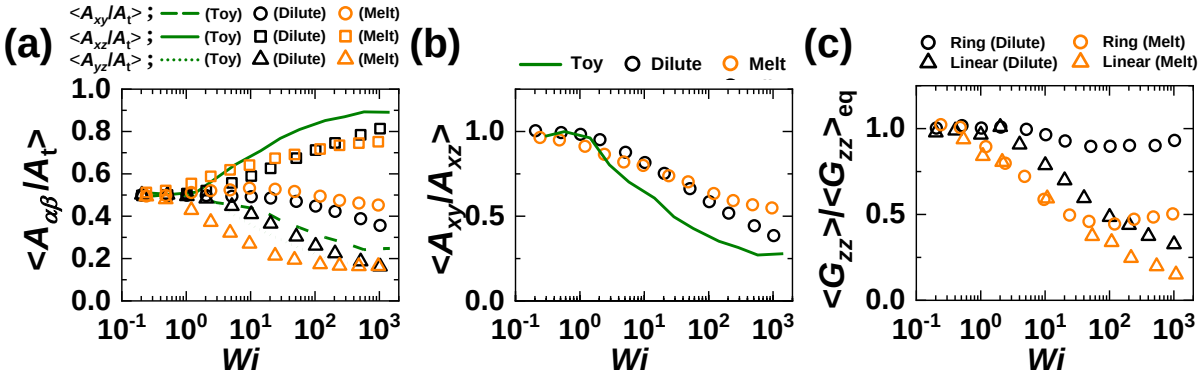


**Figure 3.2** (a) Projected areas of the intrinsic surface of the ring into three *xy*- (circles and dashed line), *xz*- (squares and solid line), and *yz*- (triangles and dotted line) planes for toy model (dark green lines), dilute system (black symbols), and melt system (orange symbols) as a function of Weissenberg number (*Wi*). The projected areas were normalized by the total area of the intrinsic ring surface $A_t$. (b) The ratio between $A_{xy}$ and $A_{xz}$ as a function of *Wi* for toy model (dark green line), dilute system (black circles), and melt system (orange circles). (c) The neutral direction (*zz*-)component of the gyration tensor $G_{\alpha\beta}$ $[=\frac{1}{N}\sum_{i=1}^{N}(\mathbf{r}_{i,\alpha}-\mathbf{r}_{c,\alpha})(\mathbf{r}_{i,\beta}-\mathbf{r}_{c,\beta})$, where $\mathbf{r}_i$, $\mathbf{r}_c$, and $N$ denote the position of particle $i$, the center of mass of the chain, and the number of particles per chain, respectively] for linear (triangles) and ring (circles) polymers with respect to *Wi*. The error bars are smaller than the size of the symbols unless otherwise specified.

This was confirmed by the results for the projected areas of the curved ring surface for each system, i.e., $A_{xy}$ on the *xy*-plane, $A_{yz}$ on the *yz*-plane, and $A_{xz}$ on the *xz*-plane (Fgirue 3.1a). It is noted that the main purpose of this study is to examine the distinctive structural behaviors of the intrinsic surface of ring-shaped polymers. So, we analyzed each projected area normalized by $A_t$ for ring systems, in comparison with the toy model which had a constant $A_t$. Notably, both the dilute and melt ring systems exhibited rapid overall increasing and decreasing behaviors for $\langle A_{xz}/A_t \rangle$ and $\langle A_{xy}/A_t \rangle$, respectively, as the flow strength increased. This behavior by the actual ring polymers is fully consistent with that of the toy model, indicating essentially the same fundamental orientational characteristics (preferentially lying in the *xz*-plane) of the ring surface under shear flow. However, the degree of $\langle A_{xz}/A_t \rangle$ and $\langle A_{xy}/A_t \rangle$ variation appears to be somewhat smaller for actual systems compared with the toy model. This observation in real ring polymers can be attributed to local surface fluctuations in association with many local loops that protrude in the velocity-gradient (*y*)-direction along their flexible backbone. We further notice a larger $\langle A_{xy}/A_t \rangle$ and smaller $\langle A_{yz}/A_t \rangle$ for the ring melt compared with the dilute ring system in the intermediate-to-strong flow regime. This can be closely associated with the higher degree of ring polymer center-loop tumbling dynamics (via strong intermolecular collisions) in the melt relative to a dilute solution; this will be further discussed in the following sections (Figure 3.3).

ULSAN NATIONAL INSTITUTE OF SCIENCE AND TECHNOLOGY

Additionally, Figure 3.1b shows the ratio between $\langle A_{xy} \rangle$ and $\langle A_{xz} \rangle$ representing the degree of surface orientation relative to the kinematically stable *xz*-plane under shear flow as a function of the applied flow strength. While both the dilute and melt ring systems show an overall decreasing behavior of $\langle A_{xy} \rangle / \langle A_{xz} \rangle$ with increasing shear rate, which is consistent with the toy model, it is weaker for the former compared with the latter. This is because of the significant dynamical role of local loops in actual ring polymers, resulting in considerable surface fluctuations.

As a distinctive structural feature of ring polymers, we observe that $\langle G_{zz} \rangle / \langle G_{zz} \rangle_{eq}$ of the gyration tensor **G** is considerably larger for a ring polymer than for a linear polymer for both dilute and melt systems in the intermediate-to-strong flow regime (Figure 3.1c). Furthermore, in contrast with the overall monotonically decreasing tendency of $\langle G_{zz} \rangle / \langle G_{zz} \rangle_{eq}$ with increasing shear rate for the linear system, ring systems exhibit a plateau region for $\langle G_{zz} \rangle / \langle G_{zz} \rangle_{eq}$ in certain intermediate flow regimes and even exhibit an increasing behavior under higher flow strengths. Further, the dilute ring systems also possess significantly larger values of $\langle G_{zz} \rangle / \langle G_{zz} \rangle_{eq}$ in comparison to the ring melt systems in the whole flow regime. This result for dilute ring systems appears to be consistent with the existing experimental[26] and numerical[30-33] observations of hydrodynamic inflation in the neutral (*z*-)direction for a diluted ring chain under shear and planar elongational flows. The rather large values for $G_{zz}$ as well as $A_{yz}$ and $A_{xz}$ for the ring polymers are expected to have a significant rheological influence. For instance, these geometrical characteristics would generally promote the degree of transient structural coupling between chains during their rotational and tumbling dynamics in shear flow, which results in an effective increase of momentum transfer and correlation between chains, thereby enhancing the overall stress (or viscosity) of the melt system. This has been confirmed by the lower shear-thinning behavior of the ring melt in comparison with the linear melt in the intermediate-to-strong flow regime (see ref 24) for the detailed structural and rheological properties of $C_{78}$ and $C_{400}$ PE ring melts for both shear and planar elongation flows).

ULSAN NATIONAL INSTITUTE OF SCIENCE AND TECHNOLOGY

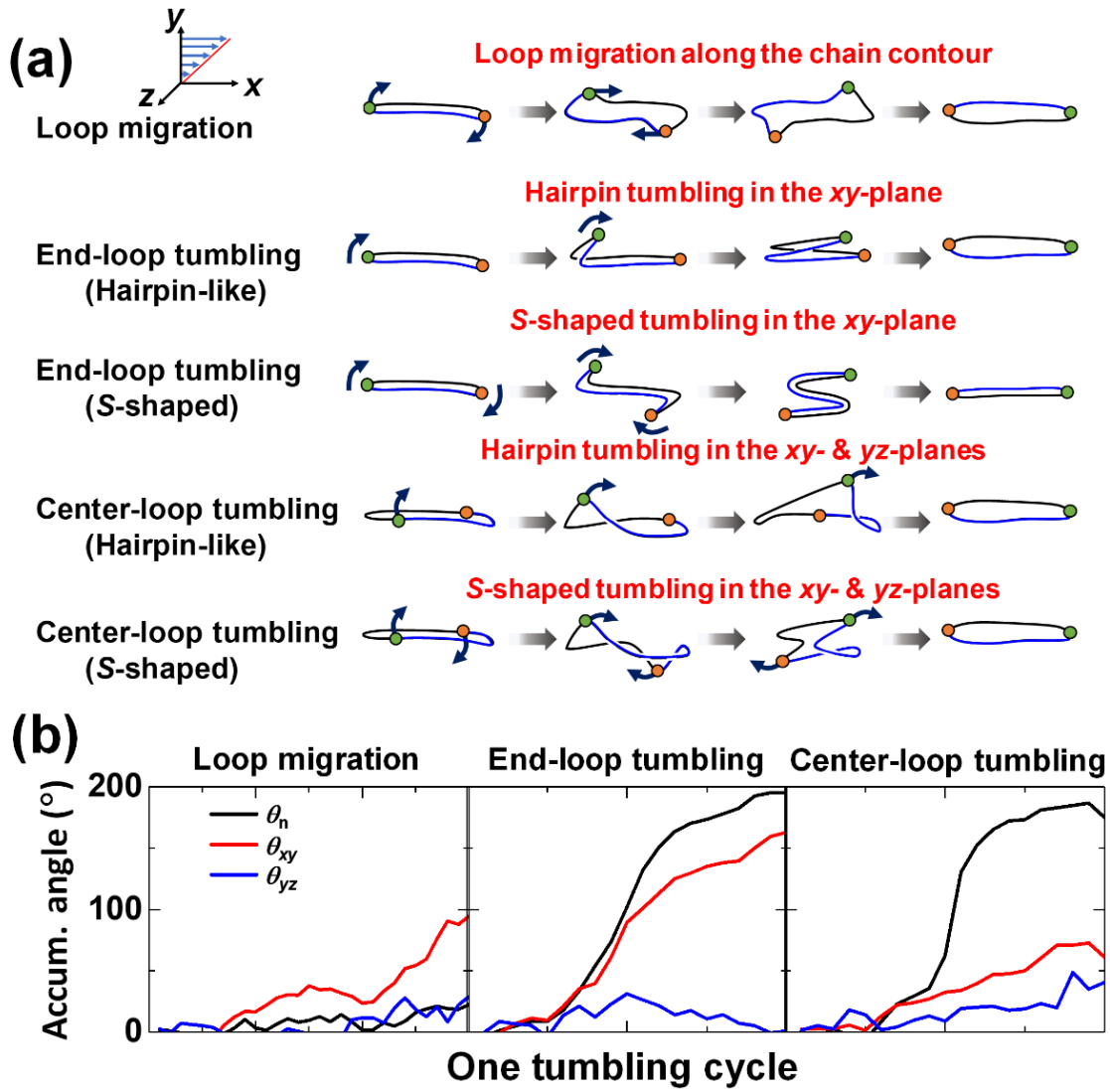


**Figure 3.3** (a) Schematic illustrations for the representative molecular mechanisms for the ring polymer under shear flow. The colored backbone and beads in the schematics are markings to help understand the dynamics of the ring polymers that have no endpoints. (b) Averaged angle accumulation during a cycle of loop migration (left panel), end-loop tumbling (middle panel), and center-loop tumbling (right panel) for $\theta_n$ of $\mathbf{n}_{avg}$, $\theta_{xy}$ of $\mathbf{Q}_{xy}$ projected on the $xy$-plane, and $\theta_{yz}$ of $\mathbf{Q}_{yz}$ projected on the $yz$-plane. Notice that the relative position vector $\mathbf{Q}_i$ of $i^{th}$ atom or bead in a chain is represented by $\mathbf{Q}_i = \mathbf{r}_i - \mathbf{r}_c$ where $\mathbf{r}_c$ denotes the center of mass position vector of a chain.

Figure 3.3a shows the characteristic rotational and tumbling dynamics mechanisms of ring chains under shear flow, which were obtained via a comprehensive analysis of the individual chain dynamics directly from the NEMD simulations. We note that these primary mechanisms are common to both dilute and melt systems, although the relative proportion of each mechanism with respect to the flow strength is quantitatively different between the two systems, as discussed later. While the chain ends have a dominant role in initiating the rotational and tumbling dynamics in linear polymers (characterizing one-dimensional curved line dynamics), the local loops protruding along the closed ring

ULSAN NATIONAL INSTITUTE OF SCIENCE AND TECHNOLOGY

backbone play a crucial role in activating the dynamic mechanisms in ring polymers (characterizing two-dimensional curved surface dynamics). It is noted that short- or long-lived loops can be locally and randomly created via thermal Brownian motion, applied flow field, and intermolecular collisions. In the intermediate flow regime, local loops protruding in the velocity-gradient (*y*-)direction tend to propagate along the closed ring surface boundary (loop-migration) and/or move in space (loop-tumbling) with the flow field. For the loop-migration mechanism, the overall surface structure of the ring is maintained quite well; hence, $\mathbf{n}_{avg}$ is practically unchanged. This means that $\mathbf{n}_{avg}$ does not detect the loop-migration dynamics (this is also true with $\mathbf{R}_{ete}$ for linear polymers), and this characteristic can be used to distinguish between the loop-migration and loop-tumbling mechanisms for ring rotation. For the loop-tumbling dynamics, ring polymers exhibit two distinct mechanisms: end-loop and center-loop tumbling. The end-loop (*S*-shaped or hairpin-like) tumbling mechanism of the stretched rings along the flow direction is essentially similar to the typical end-over-end tumbling mechanism for linear chains. However, from a geometrical viewpoint, the former characterizes the overall surface dynamics, while the latter represents the whole line dynamics. Importantly, ring polymers reveal an additional tumbling mechanism driven by the loops located in the middle of the stretched ring backbone. In contrast with the end-loop tumbling mechanism where the overall chain rotation occurs exclusively in the *xy*-plane, the center-loop mechanism has diagonal chain rotation lying through both the *xy*- and *yz*-planes. This center-loop driven tumbling leads to a variety of distinctive average and transient structural and dynamical characteristics for ring polymers in shear flow. $\mathbf{n}_{avg}$ can adequately represent both loop-tumbling mechanisms for ring polymers, similarly to $\mathbf{R}_{ete}$ for linear polymers.[49]

In Figure 3.3b we illustrate how the representative surface measures such as $\mathbf{n}_{avg}$ and the relative position vectors [$\mathbf{Q}_i = \mathbf{r}_i - \mathbf{r}_c$, for $i = 1, 2, \ldots, N_a$, where $N_a$ and $\mathbf{r}_c$ are the number of atoms (or beads) per chain and center of mass position vector of a chain, respectively] projected on the *xy*-plane ($\mathbf{Q}_{xy,i}$) and *yz*-plane ($\mathbf{Q}_{yz,i}$) can be used to characterize the aforementioned dynamics mechanisms of ring polymers in terms of the angle accumulation during chain rotation and tumbling. The accumulated angle $\theta_n(\Delta t)$ of $\mathbf{n}_{avg}$ is the summation of the angle of $\mathbf{n}_{avg}$ with respect to $\mathbf{n}_{avg}$ at a time origin of $t'$ during $\Delta t = t - t'$. Similarly, the accumulated angle $\theta_{\alpha\beta,i}(\Delta t)$ of $\mathbf{Q}_{\alpha\beta,i}$ projected on the $\alpha\beta$-plane is the summation of angle of $\mathbf{Q}_{\alpha\beta,i}$ with respect to $\mathbf{Q}_{\alpha\beta,i}$ at a time origin of $t'$ during $\Delta t = t - t'$. Thus, $\theta_{\alpha\beta}(\Delta t) = \sum_{i=1}^{N_a} \theta_{\alpha\beta,i}(\Delta t) \Big/ N_a$ with $\alpha$, $\beta = x$, $y$, or $z$ represents the average accumulated angle of $\mathbf{Q}_{\alpha\beta,i}$ projected on the $\alpha\beta$-plane. For the loop-migration case, the angles $\theta_n$ and $\theta_{yz}$ are not accumulated, while $\theta_{xy}$ is gradually accumulated indicating mainly *xy*-plane rotation for loop-migration dynamics. In sharp contrast, for both the end-loop and center-loop tumbling mechanisms, the angle accumulated by $\mathbf{n}_{avg}$ amounts to ~180°, reflecting the upside-down tumbling event for the overall ring surface. Furthermore,

ULSAN NATIONAL INSTITUTE OF
SCIENCE AND TECHNOLOGY

$\theta_{xy}$ is rapidly accumulated close to 180° for end-loop tumbling, which basically corresponds to the angle of $\mathbf{R}_{ete}$ accumulated during end-over-end tumbling of the linear polymer. In comparison, similarly to each other, $\theta_{xy}$ and $\theta_{yz}$ are gradually accumulated compared with $\mathbf{n}_{avg}$ for the center-loop tumbling mechanism. Therefore, we can distinguish among the characteristic rotation and tumbling mechanisms of ring polymers by properly analyzing these geometrical surface measures.

ULSAN NATIONAL INSTITUTE OF
SCIENCE AND TECHNOLOGY

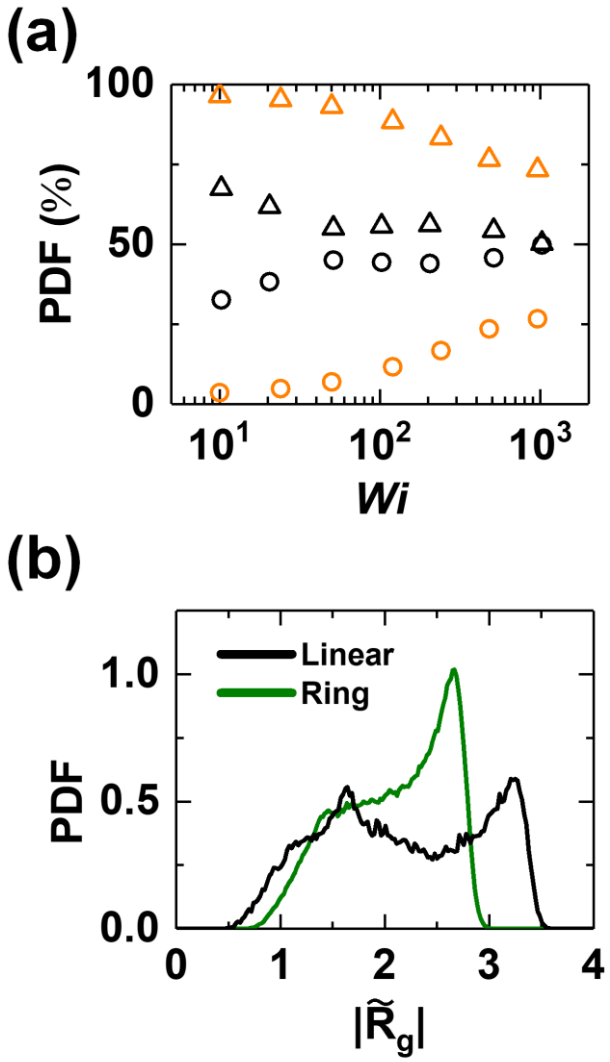


**Figure 3.4** (a) The probability of the end-loop (circle) and center-loop (triangle) tumbling with respect to *Wi* for the dilute (black) and melt (orange) ring systems. (b) Probability distribution function (PDF) of the chain radius of gyration $R_g$ (normalized by the equilibrium value) for the $C_{400}$ ring (black line) and linear (dark green line) PE melts in the strong flow regime at *Wi* = 100 and 2000, respectively, where the polymer chains in each system become maximally stretched and oriented in the flow direction. The error bars are smaller than the size of the symbols unless otherwise specified.

Based on these observations, we further specifically clarified and quantified the relative proportions of the two loop-tumbling mechanisms for the dilute and melt ring systems: (i) end-loop tumbling — accumulated angle of $\theta_n \sim 180°$, $\theta_{xy} \sim 180°$, and $\theta_{yz} \sim 0°$ (ii) center-loop tumbling — accumulated angle of $\theta_n \sim 180°$, ($\theta_{xy}$ and $\theta_{yz}$) > 45°. Overall, center-loop tumbling appears more dominant than end-loop tumbling for both systems in the whole flow regime, indicating the significant role of local loops for the ring polymer (Figure 3.4a). However, the melt system exhibits a particularly higher proportion of the center-loop mechanism because of a significantly high number of loops along

ULSAN NATIONAL INSTITUTE OF SCIENCE AND TECHNOLOGY

the ring backbone via strong intermolecular interactions.[50] This implies that the relative portion of center-loop tumbling over that of end-loop tumbling would generally increase with increasing polymer concentration for semi-dilute ring systems. As the flow strength increases, the portion of the end-loop and center-loop mechanisms generally increases and decreases, respectively, for both systems. This is mainly because both the amount and magnitude of local loops tend to decrease because of higher chain stretch and alignment in the flow direction. Notably, the dilute system exhibits a rather steep decrease followed by a plateau in the intermediate-to-strong flow regime, indicating somewhat fast saturation of the loop characteristics along with overall chain stretching and orientation. In comparison, the melt system displays a gradual decrease of center-loop tumbling in the intermediate flow regime and relatively faster decrease in the strong flow regime. It should be noted that center-loop tumbling is still dominant over end-loop tumbling for the melt system, even at strong flow fields because of many activated local loops formed via strong intermolecular collisions. Furthermore, the hairpin-like end-loop tumbling dynamics become dominant over the *S*-shaped one in the strong flow regime for both dilute and melt systems, similar to linear polymers.[51-54]

In contrast with linear polymers, this dynamical feature directly affects the overall shape of the probability distribution $P\left(R_g\right)$ of the chain radius of gyration ($R_g$) for the ring polymer (Figure 3.4b). Because stretched ring structures can be maintained during center-loop tumbling dynamics without the compact folded conformation that occurs during the end-loop tumbling dynamics (which is similar to the end-over-end tumbling dynamics of linear polymer), ring melt is supposed to exhibit a weaker rotation peak and relatively larger stretched portions in $P\left(R_g\right)$ compared with the linear analog, which is evident in Figure 3.4b.

Based on these results of high (qualitative) similarity in those characteristics between dilute and melt ring systems, we mention that all the findings for dilute and melt ring systems may be readily translated to predict the variation of the ring structure and dynamics with the polymer concentration for semi-dilute systems under shear flow. We note, however, that this simple projection on the polymer concentration effect in semi-dilute ring systems concerns only the intrinsic ring surfaces structures and dynamic mechanisms characterized here.

ULSAN NATIONAL INSTITUTE OF SCIENCE AND TECHNOLOGY

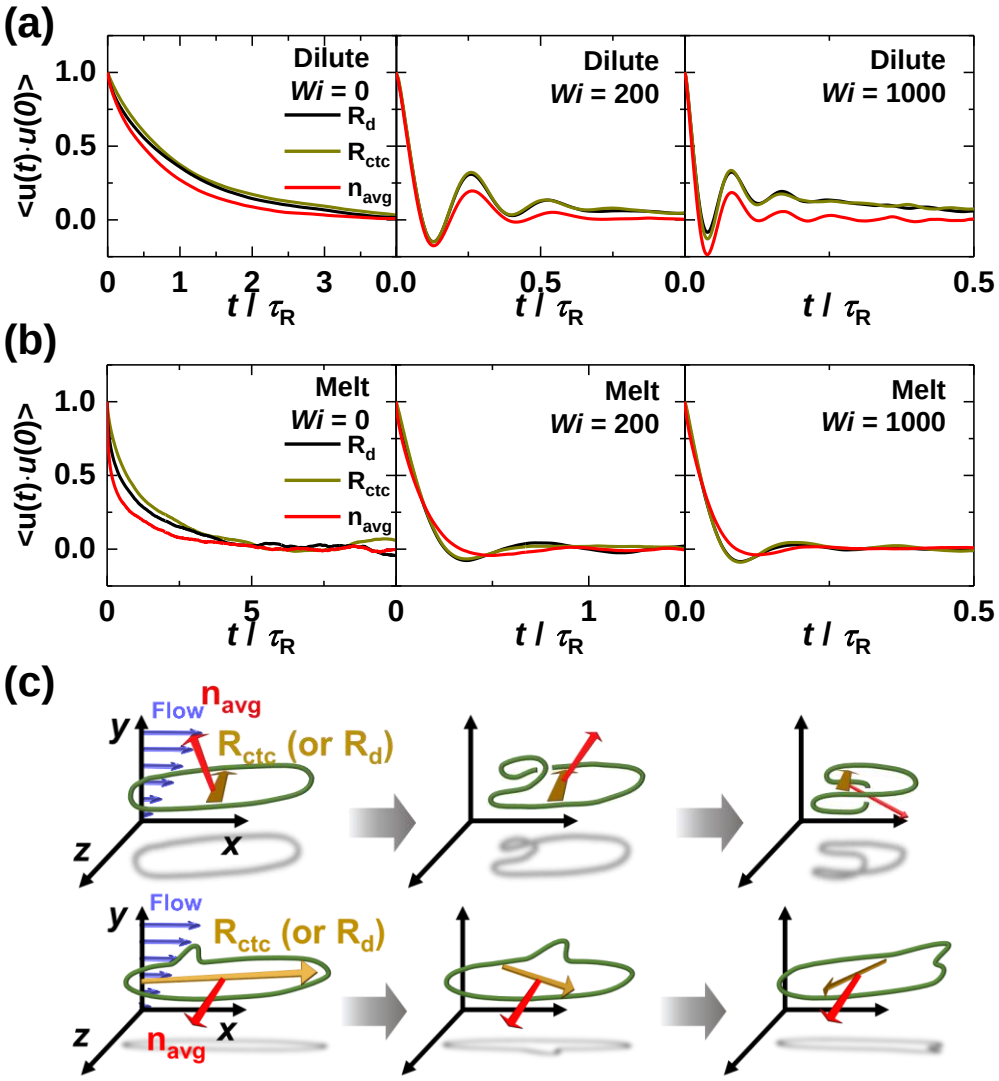


**Figure 3.5** Time correlation functions (TCFs) ($\langle \mathbf{u}(t)\cdot\mathbf{u}(0)\rangle$, where $\mathbf{u}$ is a unit vector) for the ring-diameter vector $\mathbf{R}_d$ (black lines), center-to-center vector $\mathbf{R}_{ctc}$ (yellow lines), and averaged normal vector $\mathbf{n}_{avg}$ (red lines) at equilibrium ($Wi = 0$), intermediate ($Wi = 200$), and strong flow ($Wi = 1000$) strengths as a function of the reduced time $t/\tau_R$ for (a) dilute and (b) melt ring systems. (c) Simple schematic illustrations of the dynamics of $\mathbf{R}_{ctc}$ (yellow arrow) and $\mathbf{n}_{avg}$ (red arrow) during a cycle of end-loop tumbling (top schematics) and loop-migration (bottom schematics).

We have also analyzed the characteristic rotational frequency of ring polymers as a function of flow strength by measuring the time-correlation function (TCF) $\langle \mathbf{u}(t)\cdot\mathbf{u}(0)\rangle$ of the unit vector $\mathbf{u}$ based on the three descriptors (Figures 3.5a and 3.5b): the chain center-to-center vector $\mathbf{R}_{ctc}$, ring diameter vector $\mathbf{R}_d$, and $\mathbf{n}_{avg}$ of the ring surface. Our results show that at equilibrium conditions ($Wi = 0$), the TCFs for the three descriptors give rise to quantitatively somewhat different behaviors from each other, and this becomes more noticeable for the melt system. Specifically, the TCFs of $\mathbf{R}_{ctc}$ and $\mathbf{n}_{avg}$ are the slowest and fastest, respectively. This can be understood by considering that while $\mathbf{R}_{ctc}$ is least affected by the local fluctuation of loops along the ring backbone, $\mathbf{n}_{avg}$ can be rather sensitive to

ULSAN NATIONAL INSTITUTE OF
SCIENCE AND TECHNOLOGY

topological fluctuations of the overall crumpled ring surface in its coiled conformation. The melt system displays larger discrepancies between the descriptors than the dilute system, because of a higher degree of local loops via intermolecular interactions.

For nonequilibrium systems under shear flow, the TCF of each descriptor exhibits damped sinusoidal wave characteristics indicative of the flow-induced chain rotation. The first undershoot peak of the TCF corresponds approximately to the average chain rotation or tumbling time. The undershoot time appears to be quantitatively similar for all the descriptors of the dilute system over the entire intermediate-to-strong flow regime. However, the following points need to be noted. As mentioned earlier, $\mathbf{n}_{avg}$ does not detect the chain rotation via the loop-migration mechanism. Therefore, the rotational time estimated by the TCF of $\mathbf{n}_{avg}$ can be somewhat larger than the true one. We also consider that the TCFs of $\mathbf{R}_d$ and $\mathbf{R}_{ctc}$ may predict a larger rotational time than the actual one; this is because of their incomplete rotation when the two vectors are not perfectly well aligned to the loop tumbling direction, e.g., $\mathbf{R}_d$ and $\mathbf{R}_{ctc}$ would not change at all during loop tumbling if they were aligned perpendicularly to the tumbling direction (Figure 3.5c). Therefore, it can be said that all three descriptors $\mathbf{n}_{avg}$, $\mathbf{R}_d$, and $\mathbf{R}_{ctc}$ may slightly underestimate the characteristic rotational frequency for the ring chains under shear flow. The correlation between the TCFs of the $\mathbf{n}_{avg}$, $\mathbf{R}_d$, and $\mathbf{R}_{ctc}$ for the dilute ring system indicates that the degree of underestimation for the descriptors might have been quantitatively similar to each other. In this respect, the relatively slower TCF decay of $\mathbf{n}_{avg}$ compared with $\mathbf{R}_d$ and $\mathbf{R}_{ctc}$ in the melt system can be understood by considering the higher degree of loop-migration dynamics via many local loops along the ring backbone. It should be noted that the TCFs for $\mathbf{R}_d$ and $\mathbf{R}_{ctc}$ are quantitatively very similar to each other throughout the intermediate-to-strong flow regime, where the flow-induced whole chain rotation becomes dominant over the thermally-driven local structural fluctuations. We additionally note that the TCF curves of $\mathbf{R}_d$ and $\mathbf{R}_{ctc}$ lie a little above that of $\mathbf{n}_{avg}$ for the dilute system, and this can be attributed to the aforementioned incomplete vector (de)correlation in the *z*-direction when they are not perfectly aligned to the tumbling direction (see Figures 3.5c).

ULSAN NATIONAL INSTITUTE OF SCIENCE AND TECHNOLOGY

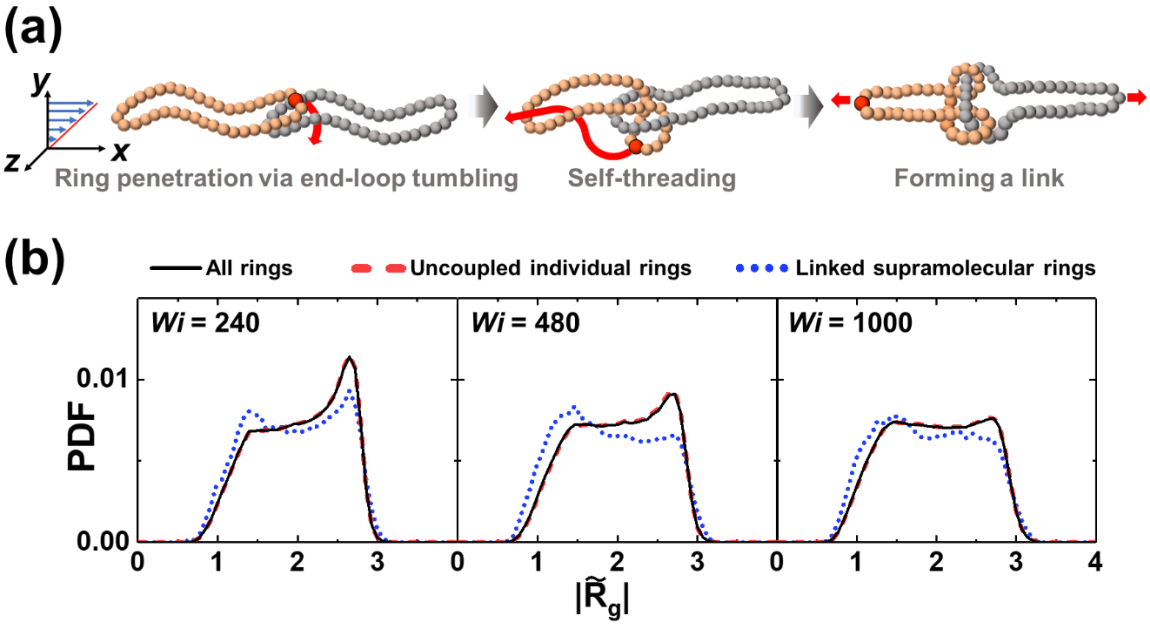


**Figure 3.6** (a) Schematic illustrations of link formation between inter-ring chains under shear flow. (b) PDFs of the chain radius of gyration (normalized by the equilibrium value) of all rings (black solid lines), the uncoupled individual rings (red dashed lines), and the linked supramolecular rings (blue dotted lines) for the melt ring system in the strong-flow regime ($Wi$ = 240, 480, and 1000), where the average chain stretching and orientation toward flow ($x$-)direction are nearly saturated.

A recent coarse-grained NEMD study based on the Kremer–Grest model for ring melts under uniaxial elongation flow reported the formation of 'supramolecular' rings in the system via topological linking between different ring molecules.[34] The authors of this study argued that this peculiar phenomenon underlies the anomalously large strain-hardening behavior of extensional viscosity even for $Wi \ll 1$, as observed in experiments.[34,35] To assess the rheological influence of supramolecular rings for shear flow in comparison to that for elongational flow, here we examined the degree of inter-ring linking and the structural behavior of linked rings by applying the present numerical algorithm to extracting the geometrical curved surfaces of the ring chains. Specifically, we first extracted the characteristic surfaces of the ring chains by applying the proposed numerical algorithm for each system configuration along the simulation trajectory. We then detected only the *mutually* threaded rings via geometrical analysis of the surface interpenetration (i.e., crossing between the individual triangle planes made by different ring chains). Finally, we closely tracked in time each linking state how long it survives and determined the sufficiently strong interpenetrated rings. Figure 3.6a schematically describes a representative mechanism for generating a topologically linked, supramolecular ring chain between two individual rings.[34] In shear flow, ring polymers frequently rotate in the shear or flow-gradient ($xy$-)plane. Thus, two adjacent rings in the melt system tend to be coupled with each other (interpenetrating) via their individual rotational and tumbling dynamics. Furthermore, the end-loop tumbling mechanism can even promote a strong topological linking (e.g., complex interpenetration with self-threading) between

ULSAN NATIONAL INSTITUTE OF SCIENCE AND TECHNOLOGY

the two rings to form a sort of reef-knot structure[34] (Figure 3.6a).

We note that a mutually threaded ring chain can be separated into its individual parts after some time by the continuous rotational dynamics of chains in shear flow. To have a meaningful rheological influence, the supramolecular linking must be maintained for a sufficiently long time. Therefore, we counted the strongly interpenetrated (mutually threaded) rings whose linking state lasted a time period longer than the longest relaxation time of the system (i.e., $\tau_R = 9.8 \pm 0.4$ ns for the $C_{400}H_{800}$ ring melt). With these criteria, strongly linked supramolecular rings were detected only in a rather strong shear-flow regime ($Wi > 100$) where the chains were nearly aligned and stretched, and their end-loop tumbling dynamics became quite effective for inducing a strong topological linking between adjacent ring chains. The proportion of effectively linked rings was found to be quite small (~3%) in the present sheared ring melts, and this appears to be considerably smaller than the proportion (~10–15%) reported by the coarse-grained MD study[34] for uniaxial elongational flow. Furthermore, all the effective supramolecular rings observed in shear flow were essentially composed of only two ring chains, which is in sharp contrast to those formed by multiple (more than three) rings in the case of elongational flow.[34] We consider that individual chain rotation and tumbling dynamics can induce the link formation between adjacent rings, but at the same time it can also help the linked rings separate into their individual parts. This is because under shear flow while some chains are oriented and stretched around the flow direction, other chains may rotate and tumble. It is thus considered that chains are not much structurally and dynamically correlated with each other in shear flow. By contrast, chains in elongational flows may be structurally and dynamically more correlated with each other, because all the chains are nearly oriented and stretched along the extension direction while they get close to each other in the contraction direction(s). This characteristic possibly may have led to a higher degree of dynamical correlation between ring chains, resulting in the multiple inter-ring link formation, as reported by the recent numerical study[34] for ring melts under uniaxial elongational flow.

Figure 3.6b compares the probability distribution functions (PDFs) of the chain radius of gyration $R_g$ between the effectively linked supramolecular rings and the uncoupled individual rings. Under shear flow, compared to the reported results of the ring melt system under uniaxial elongational flow, the PDFs of uncoupled rings appear insignificant structural differences to the coupled ring chains. In comparison to the uncoupled rings, even though the whole PDF curve of the linked rings appears to shift a little to the left, with a slightly stronger rotation peak and weaker stretch peak, this structural feature is in contrast to the existence of a noticeably long tail in the PDF of the linked rings observed in the previous coarse-grained MD study for uniaxial elongational flow. We thus consider that pure ring melts in shear flow do not seem to exhibit such distinctive rheological behavior as that observed in extensional flow.

However, if there is some constraint, which disturbs disentangling linked supramolecular ring under shear flow, we can look forward to some distinctive structural and rheological behaviors attributed

ULSAN NATIONAL INSTITUTE OF
SCIENCE AND TECHNOLOGY

to the supramolecules of linked ring chains. For instance, the short-chain branched rings can hold inter-ring chains to each other like the cogs in gear.

ULSAN NATIONAL INSTITUTE OF
SCIENCE AND TECHNOLOGY

## 3.4 Conclusion

In conclusion, we carried out a comprehensive study on the intrinsic structural characteristics and dynamic mechanisms of ring polymers under shear flow with both dilute and melt conditions. Our analysis began with the advanced viewpoint that ring polymers intrinsically possess two-dimensional surface characteristics because of their closed-loop geometry, which is in contrast with the one-dimensional line characteristics of linear polymers. Based on this view, we introduced several representative physical measures that could effectively describe the structural and dynamical characteristics of ring polymers, such as the total and projected surface areas and the average normal vector $\mathbf{n}_{avg}$ of the ring surface, which corresponds with the chain end-to-end vector $\mathbf{R}_{ete}$ of a linear polymer. Knowing the variation of these surface measures in response to the applied flow was found to be very informative for analyzing the characteristic molecular dynamics mechanisms of ring chains.

Rotational dynamics of ring polymers are characterized by three distinct mechanisms: loop migration, end-loop tumbling, and center-loop tumbling. In essence, the loops in ring polymers play a dynamically similar role as the chain ends in linear polymers. Therefore, the structural and dynamical characteristics of local loops are critically important to determine the overall ring structure and dynamics under flowing conditions. For instance, compared with the dilute ring system, ring melts have a relatively large number of local loops via intermolecular collisions, hence, they exhibit a significantly higher portion of the center-loop tumbling mechanism over the end-loop mechanism. The high degree of center-loop tumbling for the ring melt system under shear flow underlines the fact that it exhibits a noticeably weaker rotation peak and a stronger (and broader) stretch peak in the PDF of $R_g$ compared with the linear analog.[24] These findings can provide useful direction for predicting the structural and dynamical characteristics of semi-dilute polymer solutions with respect to the polymer concentration.

An efficient numerical scheme was also developed that allowed us to effectively describe the complex curved surface formed by flexible ring chains. Applying this algorithm, we could accurately measure the overall surface shape and total or projected areas. The obtained surface information was found to be very useful for analyzing the characteristic dynamic mechanisms of ring polymers under shear flow. This scheme can be further applied to extract the intrinsic geometrical characteristics for various ring-type polymers (e.g., tadpole-like polymers) and ring/linear blend systems. Furthermore, the numerical algorithm can be used to directly quantify the degree of penetration between different ring chains, thereby enabling a systematic analysis of the dynamical role of interchain penetration for ring melt systems; this has been an important (and rather controversial) rheological issue in the last decades.[1,12,18,21-23,34,35]

The new curved surface criteria and categorization of the ring-polymer dynamics proposed in this work can serve as fundamental descriptors for analyzing various ring-shaped polymers and systems, such as branched ring polymers, ring-shaped biological molecules, and two-dimensional polymers. It would be also interesting to look into the concentration effects on the intrinsic ring structures and

ULSAN NATIONAL INSTITUTE OF
SCIENCE AND TECHNOLOGY

dynamics for semi-dilute ring solutions (via, e.g., DPD[55] or MPCD[56] methods with more accurately implementing the solvent effects) in a future study.

ULSAN NATIONAL INSTITUTE OF
SCIENCE AND TECHNOLOGY

## 3.5 References

[1] Kapnistos, M.; Lang, M.; Vlassopoulos, D.; Pyckhout-Hintzen, W.; Richter, D.; Cho, D.; Chang, T.; Rubinstein, M. Unexpected power-law stress relaxation of entangled ring polymers. *Nat. Mater.* **2008**, *7*, 997-1002.

[2] Roovers, J. The melt properties of ring polystyrenes. *Macromolecules* **1985**, *18*, 1359-1361.

[3] Halverson, J. D.; Lee, W. B.; Grest, G. S.; Grosberg, A. Y.; Kremer, K. Molecular dynamics simulation study of nonconcatenated ring polymers in a melt. I. Statics. *J. Chem. Phys.* **2011**, *134*, 204904.

[4] Pasquino, R.; Vasilakopoulos, T. C.; Jeong, Y. C.; Lee, H.; Rogers, S.; Sakellariou, G.; Allgaier, J; Takano, A.; Brás, A. R.; Chang, T.; Gooßen, S; Pyckhout-Hintzen, W.; Wischnewski, A.; Hadjichristidis, N.; Richter, D.; Rubinstein, M.; Vlassopoulos, D. Viscosity of ring polymer melts. *ACS Macro Lett*. **2013**, *2*, 874-878.

[5] Trabi, M.; Craik, D. J. Circular proteins-no end in sight. *Trends Biochem. Sci.* **2002**, *27*, 132-138.

[6] Sanchez, T.; Kulic, I. M.; Dogic, Z. Circularization, photomechanical switching, and a supercoiling transition of actin filaments. *Phys*. *Rev*. *Lett*. **2010**, *104*, 098103.

[7] Cremer, T.; Cremer, C. Chromosome territories, nuclear architecture and gene regulation in mammalian cells. *Nat*. *Rev*. *Genet*. **2001**, *2*, 292-301.

[8] Halverson, J. D.; Smrek, J.; Kremer, K.; Grosberg, A. Y. From a melt of rings to chromosome territories: the role of topological constraints in genome folding. *Rep*. *Prog*. *Phys*. **2014**, *77*, 022601.

[9] Brown, S.; Lenczycki, T.; Szamel, G. Influence of topological constraints on the statics and dynamics of ring polymers. *Phys*. *Rev*. *E* **2001**, *63*, 052801.

[10] Arrighi, V.; Gagliardi, S.; Dagger, A. C.; Semlyen, J. A.; Higgins, J. S.; Shenton, M. J. Conformation of cyclics and linear chain polymers in bulk by SANS. *Macromolecules* **2004**, *37*, 8057-8065.

[11] Tsolou, G.; Stratikis, N.; Baig, C.; Stephanou, P. S.; Mavrantzas, V. G. Melt structure and dynamics of unentangled polyethylene rings: Rouse theory, atomistic molecular dynamics simulation, and comparison with the linear analogues. *Macromolecules* **2010**, *43*, 10692-10713.

[12] Vettorel, T.; Grosberg, A. Y.; Kremer, K. Statistics of polymer rings in the melt: a numerical simulation study. *Phys*. *Biol*. **2009**, *6*, 025013.

[13] Rosa, A.; Everaers, R. Ring polymers in the melt state: the physics of crumpling. *Phys*. *Rev*. *Lett*. **2014**, *112*, 118302.

[14] Cates, M.; Deutsch, J. Conjectures on the statistics of ring polymers. *J*. *Phys*. *(France)* **1986**, *47*, 2121-2128.

[15] Obukhov, S. P.; Rubinstein, M.; Duke, T. Dynamics of a ring polymer in a gel. *Phys*. *Rev*. *Lett*. **1994**, *73*, 1263.

ULSAN NATIONAL INSTITUTE OF SCIENCE AND TECHNOLOGY

[16]Milner, S. T.; Newhall, J. D. Stress relaxation in entangled melts of unlinked ring polymers. *Phys*. *Rev*. *Lett*. **2010**, *105*, 208302.

[17]Grosberg, A. Y.; Nechaev, S. K.; Shakhnovich, E. I. The role of topological constraints in the kinetics of collapse of macromolecules. *J*. *Phys*. *(France)* **1988**, *49*, 2095-2100.

[18]Sakaue, T. Statistics and geometrical picture of ring polymer melts and solutions. *Phys*. *Rev*. *E* **2012**, *85*, 021806.

[19]Lang, M. Ring conformations in bidisperse blends of ring polymers. *Macromolecules* **2013**, *46*, 1158-1166.

[20]Smrek, J.; Grosberg, A. Y. Minimal surfaces on unconcatenated polymer rings in melt. *ACS Macro Lett*. **2016**, *5*, 750-754.

[21]Tsalikis, D. G.; Mavrantzas, V. G.; Vlassopoulos, D. Analysis of slow modes in ring polymers: Threading of rings controls long-time relaxation. *ACS Macro Lett*. **2016**, *5*, 755-760.

[22]Smrek, J.; Kremer, K.; Rosa, A. Threading of unconcatenated ring polymers at high concentrations: double-folded vs time-equilibrated structures. *ACS Macro Lett*. **2019**, *8*, 155-160.

[23]Schram, R. D.; Rosa, A.; Everaers, R. Local loop opening in untangled ring polymer melts: a detailed “Feynman test” of models for the large scale structure. *Soft Matter* **2019**, *15*, 2418-2429.

[24]Yoon, J.; Kim, J.; Baig, C. Nonequilibrium molecular dynamics study of ring polymer melts under shear and elongation flows: A comparison with their linear analogs. *J*. *Rheol*. **2016**, *60*, 673-685.

[25]Yan, Z. C.; Costanzo, S.; Jeong, Y.; Chang, T.; Vlassopoulos, D. Linear and nonlinear shear rheology of a marginally entangled ring polymer. *Macromolecules* **2016**, *49*, 1444-1453.

[26]Li, Y.; Hsiao, K. W.; Brockman, C. A.; Yates, D. Y.; Robertson-Anderson, R. M.; Kornfield, J. A.; San Francisco, M. J.; Schroeder, C. M.; Mckenna, G. B. When ends meet: Circular DNA stretches differently in elongational flows. *Macromolecules* **2015**, *48*, 5997-6001.

[27]Jeong, S.; Cho, S.; Kim, J. M.; Baig, C. Interfacial molecular structure and dynamics of confined ring polymer melts under shear flow. *Macromolecules* **2018**, *51*, 4670-4677.

[28]Chen, W.; Chen, J.; An, L. Tumbling and tank-treading dynamics of individual ring polymers in shear flow. *Soft Matter* **2013**, *9*, 4312-4318.

[29]Tsamopoulos, A. J.; Katsarou, A. F.; Tsalikis, D. G.; Mavrantzas, V. G. Shear rheology of unentangled and marginally entangled ring polymer melts from large-scale nonequilibrium molecular dynamics simulations. *Polymers* **2019**, *11*, 1194.

[30]Hsiao, K. W.; Schroeder, C. M.; Sing, C. E. Ring polymer dynamics are governed by a coupling between architecture and hydrodynamic interactions. *Macromolecules* **2016**, *49*, 1961-1971.

[31]Liebetreu, M.; Ripoll, M.; Likos, C. N. Trefoil knot hydrodynamic delocalization on sheared ring polymers. *ACS Macro Lett*. **2018**, *7*, 447-452.

[32]Young, C. D.; Qian, J. R.; Marvin, M.; Sing, C. E. Ring polymer dynamics and tumbling-stretch

ULSAN NATIONAL INSTITUTE OF SCIENCE AND TECHNOLOGY

transitions in planar mixed flows. *Phys*. *Rev*. *E* **2019**, *99*, 062502

[33]Liebetreu, M.; Likos, C. N. Hydrodynamic inflation of ring polymers under shear. *Commun*. *Mater*. **2020**, *1*, 1-11.

[34]O' Connor, T. C.; Ge, T.; Rubinstein, M.; Grest, G. S. Topological linking drives anomalous thickening of ring polymers in weak extensional flows. *Phys*. *Rev*. *Lett*. **2020**, *124*, 027801.

[35]Huang, Q.; Ahn, J.; Parisi, D.; Chang, T.; Hassager, O.; Panyukov, S.; Rubinstein, M.; Vlassopoulos, D. Unexpected stretching of entangled ring macromolecules. *Phys*. *Rev*. *Lett*. **2019**, *122*, 208001.

[36]Baig, C.; Edwards, B. J.; Keffer, D. J.; Cochran, H. D.; Harmandaris, V. Rheological and structural studies of linear polyethylene melts under planar elongational flow using nonequilibrium molecular dynamics simulations. *J. Chem. Phys.* **2006**, *124*, 084902.

[37]Nosé, S. A molecular dynamics method for simulations in the canonical ensemble. *Mol. Phys.* **1984**, *52*, 255-268.

[38]Hoover, W. G. Canonical dynamics: Equilibrium phase-space distributions. *Phys. Rev. A* **1985**, *31*, 1695.

[39]Lees, A. W.; Edwards, S. F. The computer study of transport processes under extreme conditions. *J. Phys. C: Solid State Phys.* **1972**, *5*, 1921.

[40]Tuckerman, M.; Berne, B. J.; Martyna, G. J. Reversible multiple time scale molecular dynamics. *J. Chem. Phys.* **1992**, *97*, 1990-2001.

[41]Siepmann, J. I.; Karaborni, S.; Smit, B. Simulating the critical behaviour of complex fluids. *Nature* **1993**, *365*, 330-332.

[42]Öttinger, H. C. *Stochastic Processes in Polymeric Fluids*; Springer: Berlin, 1996.

[43]Weeks, J. D.; Chandler, D.; Andersen, H. C. Role of repulsive forces in determining the equilibrium structure of simple liquids. *J*. *Chem*. *Phys*. **1971**, *54*, 5237-5247.

[44]Rotne, J.; Prager, S. Variational treatment of hydrodynamic interaction in polymers. *J*. *Chem*. *Phys*. **1969**, *50*, 4831-4837.

[45]Yamakawa, H. Transport properties of polymer chains in dilute solution: hydrodynamic interaction. *J*. *Chem*. *Phys*. **1970**, *53*, 436-443.

[46]Ramachandran, R.; Beaucage, G.; Kulkarni, A. S.; McFaddin, D.; Merrick-Mack, J.; Galiatsatos, V. Persistence length of short-chain branched polyethylene. *Macromolecules* **2008**, *41*, 9802-9806.

[47]Bird, R. B.; Curtiss, C. F.; Armstrong, R. C.; Hassager, O. *Dynamics of Polymeric Liquids*, Vol. 2 Wiley: New York, 1987.

[48]Liu, T. W. Flexible polymer chain dynamics and rheological properties in steady flows. *J*. *Chem*. *Phys*. **1989**, *90*, 5826-5842.

[49]Similarly to the linear polymers [Cho, S.; Jeong, S.; Kim, J. M.; Baig, C. *Sci*. *Rep*. **2017**, *7*, 9004], the hairpin-like end-loop and center-loop tumbling dynamics relative to the corresponding *S*-shaped ones become dominant as the flow strength increases for both dilute and melt ring polymers,

ULSAN NATIONAL INSTITUTE OF SCIENCE AND TECHNOLOGY

since a strong flow field does not allow enough time for the head and tail loops of ring chains along the tumbling direction to symmetrically execute their relative movements during the overall tumbling time span. That is, either head or tail loop alone leads the overall chain tumbling motion rather quickly without waiting for the other one to move in the relatively opposite tumbling direction.

[50] Additionally, in comparison to the dilute ring system, the ring melt exhibits the relatively narrower and sharper local loops as a result of strong intermolecular collisions under shear flow, which appear to further promote the center-loop tumbling dynamics.

[51] Xu, Z.; Kim, S.; de Pablo, J. J. Anisotropic friction and excluded volume effects in freely jointed bead–rod polymer chain models. *J. Chem. Phys.* **1994**, *101*, 5293-5304.

[52] Schroeder, C. M.; Teixeira, R. E.; Shaqfeh, E. S. G.; Chu, S. Characteristic periodic motion of polymers in shear flow. *Phys. Rev. Lett.* **2005**, *95*, 018301.

[53] Teixeira, R. E.; Babcock, H. P.; Shaqfeh, E. S. G.; Chu, S. Shear thinning and tumbling dynamics of single polymers in the flow-gradient plane. *Macromolecules* **2005**, *38*, 581-592.

[54] Kim, J. M.; Edwards, B. J.; Keffer, D. J.; Khomami, B. Dynamics of individual molecules of linear polyethylene liquids under shear: Atomistic simulation and comparison with a free-draining bead-rod chain. *J. Rheol.* **2010**, *54*, 283-310.

[55] Liu, M. B.; Liu, G. R.; Zhou, L. W.; Chang, J. Z. Dissipative particle dynamics (DPD): an overview and recent developments. *Arch. Computat. Methods Eng.* **2015**, *22*, 529-556.

[56] Malevanets, A.; Kapral, R. Mesoscopic model for solvent dynamics. *J. Chem. Phys.* **1999**, *110*, 8605-8613.

ULSAN NATIONAL INSTITUTE OF SCIENCE AND TECHNOLOGY

# IV. Appendix

## 1. Coarse grained bead-spring Brownian dynamics (BD) simulation

As is well known[1], the Gaussian approximation of chain configurations leading to the (linear) Hookean harmonic entropic spring force law can be approximately valid for long polymer chains only at equilibrium or near equilibrium states where chains are not much deformed (stretched). The linear spring approximation becomes seriously inaccurate for describing largely deformed chain structures and the concomitant rheological properties under rather strong external flow fields, in which case the inverse Langevin (or Finite Extensible Nonlinear Elastic (FENE)-type) function derived based on rigorous statistical mechanical procedures should be used; the inverse Langevin (or FENE) force law is correctly reduced to the linear Hookean one for small deformation of chain structure. Therefore, in order to adequately describe the structural and rheological behaviors for polymeric fluids in a wide range of flow strengths under shear and elongational flow, a standard FENE force law was adopted for the bead-spring BD simulations of H-polymer systems in this study. The FENE spring force law for each spring $\left(F_i^s\right)$ is written as

$$\boldsymbol{F}_i^S = -Kh_i\boldsymbol{Q}_i\,, \qquad h_i = \frac{1}{1-\left|Q_i\right|^2/b_s}, \quad i = 1,2,\ldots\ldots,N-1 \tag{A1.1}$$

where $\boldsymbol{Q}_i$ and $K$ denote the connector vector and elastic spring constant of the $i^{\text{th}}$ spring, respectively. $b_s$ refers to the maximum extensibility of all springs and $h_i$ defines specific form of the spring. $N$ represents the total number of beads in a chain and the number of springs is thus equal to $N$–1.

From the force balance on a bead[2], the evolution equation of a connector vector ($\boldsymbol{Q}_{\alpha,i} = \boldsymbol{r}_{\alpha,i+1} - \boldsymbol{r}_{\alpha,i}$, where $\alpha = x, y, z$) is derived as

$$d\boldsymbol{Q}_{\alpha,i} = \left[\boldsymbol{\kappa}_{\alpha\beta}\boldsymbol{Q}_{\beta,i} + \zeta_{\alpha\beta}^{-1}\sum_{k=1}^{N-1}\boldsymbol{A}_{ik}\boldsymbol{F}_{\beta,k}^S\right]dt + B_{\alpha\beta}\left(d\boldsymbol{W}_{\beta,i+1} - d\boldsymbol{W}_{\beta,i}\right) \tag{A1.2}$$

$$\boldsymbol{A}_{ik} = \begin{cases} 2 & if \ \left|i-k\right| = 0 \\ -1 & if \ \left|i-k\right| = 1 \\ 0 & otherwise \end{cases}$$

where $\boldsymbol{A}_{ik}$ and $\tilde{\boldsymbol{\kappa}}$ denote the Rouse matrix[3] and velocity gradient tensor of flow field, respectively. Note that Eq. (A2) can be made dimensionless with

$\boldsymbol{Q}_i = \sqrt{\frac{k_BT}{K}}\tilde{\boldsymbol{Q}}_i$ , $\tau_R = \frac{\zeta_0}{4K}$ , $t = \frac{\tau_R}{\tilde{\tau}_R}\tilde{t} = \frac{\zeta_0}{4K\tilde{\tau}_R}\tilde{t}$ , $d\boldsymbol{W}_i = \sqrt{dt}\times d\tilde{\boldsymbol{W}}_i$ , $\zeta_{\alpha\beta}^{-1} = B_{\alpha\gamma}B_{\gamma\beta}^T$ , $B_{\alpha\beta}$ $= \sqrt{2k_BT\zeta_0^{-1}}\tilde{B}_{\alpha\beta}$ , and $\boldsymbol{F}^S = \sqrt{Kk_BT}\times\tilde{\boldsymbol{F}}^S$ . For branch (or junction) points in the backbone, the contributions by the branches were added to Eq. (A1.2):

ULSAN NATIONAL INSTITUTE OF SCIENCE AND TECHNOLOGY

$$d\tilde{\mathbf{Q}}_{\alpha,i}=\left[\tilde{\boldsymbol{\kappa}}_{\alpha\beta}\tilde{\mathbf{Q}}_{\beta,i}+\frac{1}{4\tilde{\tau}_R}\sum_{k=1}^{N-1}\mathbf{A}_{ik}\tilde{\mathbf{F}}^{S}_{\alpha,k}+\frac{A_0}{4\tilde{\tau}_R\times brfac}\tilde{\mathbf{F}}^{S,branch}_{\alpha}\right]dt+\sqrt{\frac{1}{2\tilde{\tau}_R}}\left(d\tilde{\mathbf{W}}_{\alpha,i+1}-d\tilde{\mathbf{W}}_{\alpha,i}\right) \quad \text{(A1.3)}$$

$$A_0=\begin{cases}+1 & \textit{if a branch is attached to } \mathbf{r}_i \textit{ of } \mathbf{Q}_i\\ -1 & \textit{if a branch is attached to } \mathbf{r}_{i+1} \textit{ of } \mathbf{Q}_i\end{cases}$$

where the 'brfac' represents an adjustable parameter that controls the characteristic relaxation time (or mobility) of branches via $\tilde{\tau}_R\times brfac$. Smaller value of brfac corresponds a shorter characteristic relaxation time or higher mobility of branches. In case of brfac = 1, the branch has the same monomeric relxation time to other Kuhn segments. The value of brfac was set to 0.05 indirectly by comparing between the mesoscopic BD and atomistic NEMD reuslts for represenetative structural or dynamical results. For branches, the backbone contributions should be added to Eq. (A1.2) as follows:

$$\begin{aligned}d\tilde{\mathbf{Q}}^{branch}_{\alpha,i}=&\left[\tilde{\boldsymbol{\kappa}}_{\alpha\beta}\tilde{\mathbf{Q}}^{branch}_{\beta,i}+\frac{1}{4\tilde{\tau}_R\times brfac}\tilde{\mathbf{F}}^{S,branch}_{\alpha,i}+\frac{1}{4\tilde{\tau}_R}\left(\tilde{\mathbf{F}}^{S,backbone2}_{\alpha}-\tilde{\mathbf{F}}^{S,backbone1}_{\alpha}\right)\right]dt\\&+\sqrt{\frac{1}{2\tilde{\tau}_R\times brfac}}d\tilde{\mathbf{W}}^{branch}_{\alpha,i}-\sqrt{\frac{1}{2\tilde{\tau}_R}}d\tilde{\mathbf{W}}^{backbone}_{\alpha}\end{aligned} \quad \text{(A1.4)}$$

The velocity gradient tensor ($\tilde{\boldsymbol{\kappa}}$) for shear and uniaxial elongational flows is defined as

$$\tilde{\boldsymbol{\kappa}}=\begin{pmatrix}0 & \dot{\tilde{\gamma}} & 0\\ 0 & 0 & 0\\ 0 & 0 & 0\end{pmatrix} \text{ for the shear flow,}$$

$$\tilde{\boldsymbol{\kappa}}=\begin{pmatrix}\dot{\tilde{\varepsilon}} & 0 & 0\\ 0 & -\frac{1}{2}\dot{\tilde{\varepsilon}} & 0\\ 0 & 0 & -\frac{1}{2}\dot{\tilde{\varepsilon}}\end{pmatrix} \text{ for the uniaxial elongational flow.}$$

All the evolution equations of the connector vectors were integrated with a modified semi-implicit predictor-corrector method in this work [the original semi-implicit predictor-corrector method can be found in reference 4]. The predictor step was described as follows:

$$\hat{\mathbf{Q}}_{\alpha,i}=\tilde{\mathbf{Q}}_{\alpha,i}+\left[\tilde{\boldsymbol{\kappa}}_{\alpha\beta}\tilde{\mathbf{Q}}_{\beta,i}+\frac{1}{4\tilde{\tau}_R}\sum_{k=1}^{N-1}\mathbf{A}_{ik}\tilde{\mathbf{F}}^{S}_{\alpha,k}+\frac{A_0}{4\tilde{\tau}_R\times brfac}\tilde{\mathbf{F}}^{S,branch}_{\alpha}\right]dt+\sqrt{\frac{1}{2\tilde{\tau}_R}}\left(d\tilde{\mathbf{W}}_{\alpha,i+1}-d\tilde{\mathbf{W}}_{\alpha,i}\right) \quad \text{(A1.5)}$$

Where $\tilde{\mathbf{Q}}^{t}_{\alpha,i}$ and $\tilde{\mathbf{F}}^{S,t}_{\alpha,i}$ denote the connector vector and the elastic spring force for the $i^{\text{th}}$ segment at time $t$. The first corrector step was carried out by

$$\begin{aligned}\bar{\mathbf{Q}}^{t+\delta t}_{\alpha,i}-\frac{\delta t}{4\tilde{\tau}_R}\bar{\mathbf{F}}^{S,t+\delta t}_{\alpha,i}=\tilde{\mathbf{Q}}^{t}_{\alpha,i}+&\left[\tilde{\boldsymbol{\kappa}}_{\alpha\beta}\left(\tilde{\mathbf{Q}}^{t}_{\beta,i}+\hat{\mathbf{Q}}^{t+\delta t}_{\beta,i}\right)+\frac{1}{4\tilde{\tau}_R}\left(-\tilde{\mathbf{F}}^{S,t}_{\alpha,i-1}+2\tilde{\mathbf{F}}^{S,t}_{\alpha,i}-\tilde{\mathbf{F}}^{S,t}_{\alpha,i+1}\right)\right.\\&\left.+\frac{1}{4\tilde{\tau}_R}\left(-\hat{\mathbf{F}}^{S,t+\delta t}_{\alpha,i-1}-\hat{\mathbf{F}}^{S,t+\delta t}_{\alpha,i+1}\right)\right]\frac{\delta t}{2}+\sqrt{\frac{1}{2\tilde{\tau}_R}}\left(d\tilde{\mathbf{W}}_{\alpha,i+1}-d\tilde{\mathbf{W}}_{\alpha,i}\right)\end{aligned} \quad \text{(A1.6)}$$

ULSAN NATIONAL INSTITUTE OF SCIENCE AND TECHNOLOGY

By rearranging the Eq. (A1.6), we can obtain a cubic equation for the magnitude of $\bar{\boldsymbol{Q}}_{\alpha,i}$ as

$$\left|\bar{Q}_{\alpha,i}^{t+\delta t}\right|^3 - \boldsymbol{RHS}\left|\bar{Q}_{\alpha,i}^{t+\delta t}\right|^2 - b_s\left(1+\frac{\delta t}{4\tilde{\tau}_R}\right)\left|\bar{Q}_{\alpha,i}^{t+\delta t}\right| + b_s \times \boldsymbol{RHS} = 0 \tag{A1.7}$$

where the **RHS** is the magnitude of the right hand side of Eq. (A1.6). By solving Eq. (A1.7), unique solution between 0 and $\sqrt{b_s}$ is obtained with the value of $\left|\bar{Q}_{\alpha,i}^{t+\delta t}\right|$ never going beyond $\sqrt{b_s}$. The second predictor step was given as

$$\begin{aligned}\boldsymbol{Q}_{\alpha,i}^{t+\delta t} - \frac{\delta t}{4\tilde{\tau}_R}\boldsymbol{F}_{\alpha,i}^{S,t+\delta t} = \tilde{\boldsymbol{Q}}_{\alpha,i}^{t} + \Bigg[\tilde{\boldsymbol{\kappa}}_{\alpha\beta}\left(\tilde{\boldsymbol{Q}}_{\beta,i}^{t} + \bar{\boldsymbol{Q}}_{\beta,i}^{t+\delta t}\right) + \frac{1}{4\tilde{\tau}_R}\left(-\tilde{\boldsymbol{F}}_{\alpha,i-1}^{S,t} + 2\tilde{\boldsymbol{F}}_{\alpha,i}^{S,t} - \tilde{\boldsymbol{F}}_{\alpha,i+1}^{S,t}\right)\\ + \frac{1}{4\tilde{\tau}_R}\left(-\bar{\boldsymbol{F}}_{\alpha,i-1}^{S,t+\delta t} - \tilde{\boldsymbol{F}}_{\alpha,i+1}^{S,t}\right)\Bigg]\frac{\delta t}{2} + \sqrt{\frac{1}{2\tilde{\tau}_R}}\left(d\tilde{\boldsymbol{W}}_{\alpha,i+1} - d\tilde{\boldsymbol{W}}_{\alpha,i}\right)\end{aligned} \tag{A1.8}$$

Rearranging Eq. (A1.8) gives rise to a cubic equation for the magnitude of $\boldsymbol{Q}_{\alpha,i}^{t+\delta t}$

$$\left|Q_{\alpha,i}^{t+\delta t}\right|^3 - \boldsymbol{R}\left|Q_{\alpha,i}^{t+\delta t}\right|^2 - b_s\left(1+\frac{\delta t}{4\tilde{\tau}_R}\right)\left|Q_{\alpha,i}^{t+\delta t}\right| + b_s \times \boldsymbol{R} = 0\,. \tag{A1.9}$$

Similar to first corrector step, the value of $\left|Q_{\alpha,i}^{t+\delta t}\right|$ can be obtained solving Eq. (A1.9). Given all the information of $\left|Q_{\alpha,i}^{t+\delta t}\right|$ and $\left|\bar{Q}_{\alpha,i}^{t+\delta t}\right|$, we can set the residual $\varepsilon$ as,

$$\varepsilon = \sqrt{\sum_{i=1}^{N_s}\left[Q_{\alpha,i}^{t+\delta t} - \bar{Q}_{\alpha,i}^{t+\delta t}\right]^2}\quad . \tag{A1.10}$$

If the residual is greater than a specific tolerance $\left(\varepsilon > 10^{-5}\right)$, $\boldsymbol{Q}_{\alpha,i}^{t+\delta t}$ was copied onto $\bar{\boldsymbol{Q}}_{\alpha,i}^{t+\delta t}$ and the second predictor step was repeated until a full convergence.

For the SCB polymer systems, the maximum extensibility parameter of the entire chain ($b_m$) and that of each spring ($b_s$) were calculated as

$$b_m = \frac{3\times R_{\max}^2}{\left\langle R_{\text{ete}}^2\right\rangle_{\text{eq}}},\quad b_s = \frac{b_m}{N_s^2} = \frac{185.3}{60^2} \approx 0.051, \tag{A1.11}$$

$$\left|Q_{\max}\right| = \sqrt{b_s} \approx 0.2269, \qquad \left|Q_{\max}^{\text{SCB}}\right| = \left|Q_{\max}\right|/2,$$

where $R_{\max}$ and $N_s$ are the fully stretched chain length and the number of springs of the chain end-to-end dimension of the SCB chain, respectively (i.e., $N_s$ = 60; 59 springs in the backbone).

For an H-shaped chain, the $b_m$ and $b_s$ were calculated as

$$b_s = \frac{b_m}{N_s^2} = \frac{306.44}{102^2} \approx 0.02945, \tag{A1.12}$$

ULSAN NATIONAL INSTITUTE OF SCIENCE AND TECHNOLOGY

$$\left|Q_{\max}\right| = \sqrt{b_s} \approx 0.171621, \qquad \left|Q_{\max}^{\mathrm{SCB}}\right| = \left|Q_{\max}\right| / 2,$$

where $R_{\max}$ and $N_s$ are the fully stretched chain length and the number of springs of the longest linear dimension of the H-shaped chain, respectively (i.e., $N_s$ = 102; 68 springs in the backbone plus 17 springs in each of the two arms). $\left\langle R_{\mathrm{ete}}^2 \right\rangle_{\mathrm{eq}}$ was chosen as the mean square chain end-to-end distance of the linear chain corresponding to the longest linear dimension of the H-shaped polymer[5,6].

ULSAN NATIONAL INSTITUTE OF SCIENCE AND TECHNOLOGY

## 2. Non-equilibrium Molecular Dynamics (NEMD) simulation

Atomistic nonequilibrium molecular dynamics (NEMD) simulations of the ring and linear polyethylene (PE) melt systems were performed in the canonical (*NVT*) ensemble composed with the constant temperature $T = 450$ K and density $\rho = 0.764$ g cm$^{-3}$ (corresponding to the pressure $P = 1$ atm)[5,6] by using the *p*-SLLOD equations of motion,[3] implemented by the Nosé-Hoover thermostat[7,8]:

$$\dot{\mathbf{r}}_{ia} = \frac{\mathbf{p}_{ia}}{m_{ia}} + \mathbf{r}_{ia} \cdot \nabla\mathbf{u}$$

$$\dot{\mathbf{p}}_{ia} = \mathbf{F}_{ia} - \mathbf{p}_{ia} \cdot \nabla\mathbf{u} - m_{ia} \cdot \nabla\mathbf{u} \cdot \nabla\mathbf{u} - \dot{\varsigma}\mathbf{p}_{ia} \tag{A2.1}$$

$$\dot{\varsigma} = \frac{p_\varsigma}{Q}, \quad p_\varsigma = \sum_i \sum_a \frac{p_{ia}^2}{m_{ia}} - DNk_BT, \quad Q = DNk_BT\tau^2$$

Here, $N$ and $V$ are the total number of atoms and volume of the system, respectively. $\mathbf{r}_{ia}$, $\mathbf{p}_{ia}$, $m_{ia}$, and $\mathbf{F}_{ia}$ are the position vector, momentum vector, mass, and force vector of atom $a$ in molecule $i$, respectively. The $\varsigma$ and $p_\varsigma$ are the coordinate- and momentum-like variables, respectively, of the Nosé-Hoover thermostat, and $Q$ is the mass parameter of the thermostat with its relaxation time parameter $\tau$ (which was set equal to 0.24 ps for all NEMD simulations). $k_B$ refers to the Boltzmann constant and $D$ denotes the dimensionality of the system. The velocity gradient tensor $\nabla\mathbf{u}$ is expressed as

$$\nabla\mathbf{u} = \begin{pmatrix} 0 & 0 & 0 \\ \dot{\gamma} & 0 & 0 \\ 0 & 0 & 0 \end{pmatrix}, \tag{A2.2}$$

where $\dot{\gamma}$ is the applied shear rate ($x$ and $y$ are the flow and velocity gradient directions, respectively). The standard Lees-Edwards sliding-brick boundary conditions[9] were used for the shear flow. The set of equations of motion in the NEMD simulation was numerically integrated using the reversible reference system propagator algorithm (*r*-RESPA)[10] with two different time scales: 0.47 fs for three bonded (bond-stretching, bond-bending, and bond-torsional) interactions and 2.35 fs for two nonbonded inter- and intramolecular Lennard–Jones (LJ) interactions (see the Supporting Information of ref 2 for the *r*-RESPA formula).

The well-known Siepmann-Karaboni-Smit (SKS) united-atom potential model[11] was adopted for all the NEMD systems except that the original rigid bond was replaced by a flexible one with harmonic potential. In this model, the nonbonded intermolecular and intramolecular interactions are represented by the 6-12 LJ potential:

$$U_{\mathrm{LJ}}(r_{ij}) = 4\varepsilon_{ij}\left[\left(\frac{\sigma_{ij}}{r_{ij}}\right)^{12} - \left(\frac{\sigma_{ij}}{r_{ij}}\right)^{6}\right], \tag{A2.3}$$

where $\varepsilon_{ij}=(\varepsilon_i\varepsilon_j)^{1/2}$ and $\sigma_{ij}=(\sigma_i+\sigma_j)/2$ adopting the standard Lorentz-Berthelot mixing rules for

ULSAN NATIONAL INSTITUTE OF SCIENCE AND TECHNOLOGY

interactions between atomistic units *i* and *j*. $r_{ij}$ indicates the distance between $\mathbf{r}_i$ and $\mathbf{r}_j$ ($r_{ij} = |\mathbf{r}_i - \mathbf{r}_j|$). For the $CH_2$ united atom in ring molecules, $\varepsilon/k_B$ = 47 K and $\sigma$ = 3.93 Å. A cut-off distnace equal to 2.5 $\sigma$ was used in the simulations. The bond-stretching interaction energy $U_{\text{str}}$ was described by a harnomic potential:

$$U_{\text{str}}(l) = \frac{k_{\text{str}}}{2}(l - l_{eq})^2, \tag{A2.4}$$

where the equilibrium bond length $l_{\text{eq}}$ = 1.54 Å and the bond-stretching constant $k_{\text{str}}/k_B$ = 452,900 K/Å$^2$. The bond-bending interaction energy $U_{\text{ben}}$ was also described as harmonic potential:

$$U_{\text{ben}}(\theta) = \frac{k_{\text{ben}}}{2}(\theta - \theta_{eq})^2, \tag{A2.5}$$

where the equilibrium bending angle $\theta_{\text{eq}}$ = 114° and the bond-bending constant $k_{\text{ben}}/k_B$ = 62,500 K/rad$^2$ from van der Ploeg et al..[12] The bond-torsional interaction energy $U_{\text{tor}}$ was described by the potential proposed by Jorgensen et al.[13]

$$U_{\text{tor}}(\phi) = \sum_{n=0}^{3} a_n \cos^n \phi, \tag{A2.6}$$

where the bond-torsional constants were set as $a_0/k_B$ = 1010 K, $a_1/k_B$ = 2019 K, $a_2/k_B$ = 136.4 K, and $a_3/k_B$ = –3165 K.

Sufficiently large number of molecules were employed in the simulations with the box dimensions being set to 260.7 Å × 86.9 Å × 86.9 Å ($x \times y \times z$). The system box dimension was enlarged in the flow *x*-direction to avoid any system-size effects, especially for high flow fields where chains are highly aligned and stretched. The box dimensions were set based on the mean-square chain radius of gyration, $\left\langle R_{\mathbf{g}}^2 \right\rangle_{eq}^{1/2}$ ≈ 22.1 Å for $C_{400}H_{800}$ ring melts, so the box dimensions in the velocity gradient (*y*-) and neutral (*z*-) directions were set to more than three times $\left\langle R_{\mathbf{g}}^2 \right\rangle_{eq}^{1/2}$. The longest characteristic relaxation time $\tau_R$ of the system was estimated by the integral below the stretched-exponential curve[14-16] describing the time autocorrelation function for the unit ring diameter vector $\mathbf{R}_{\text{d}}$ for ring polymer and unit chain end-to-end vector $\mathbf{R}_{\text{ete}}$ for linear polymer;[6] $\tau_R$ = 9.8 ns and $\tau_R$ = 218 ns for the $C_{400}$ ring and linear PE melt systems, respectively.[17]

ULSAN NATIONAL INSTITUTE OF SCIENCE AND TECHNOLOGY

## 3. Coarse grained bead-rod Brownian dynamics (BD) simulation

The dilute ring polymer system was modeled as a freely rotating bead-rod chain possessing the same persistence length (i.e., 1 rod ≈ 6 atoms for PE)[18] as the PE molecule used in the NEMD simulations for dense polymeric liquids under strong shear flow. The bead-rod ring chain consisted of 66 beads and 66 rods (corresponding to 400 $CH_2$ monomer for PE) where the beads act as interaction points for the Brownian random force, excluded volume (EV), and hydrodynamic interaction (HI) effects and the rigid rods serve as constraints to keep every bead at a constant distance. This system is described by a diffusion equation with generalized coordinates.[2] The equivalent stochastic differential equation was derived by Öttinger[19,20]:

$$\begin{aligned} d\mathbf{r}_i = & \sum_j \mathbf{P}_{ij} \cdot \left\{ \left[ \mathbf{v}_0 + \boldsymbol{\kappa} \cdot \mathbf{r}_j + \sum_l \mathbf{D}_{jl} \cdot \left( \mathbf{F}_l + \mathbf{F}_l^{(e)} + \mathbf{F}_l^{(m)} \right) \right] dt + \sqrt{2k_B T} \sum_l \mathbf{B}_{jl} \cdot d\mathbf{W}_l \right\} \\ & - k_B T \sum_{v=1}^{d'} \sum_{kjl} \left[ \mathbf{P}_{ij} \cdot \mathbf{D}_{kl} \right] : \frac{\partial^2 g_v}{\partial \mathbf{r}_l \partial \mathbf{r}_j} \frac{\partial \mathbf{R}_i}{\partial g_v} dt \\ & - k_B T \sum_{v=1}^{d'} \sum_{kjl} \mathbf{P}_{ik} \cdot \mathbf{D}_{kl} \cdot \frac{\partial^2 g_v}{\partial \mathbf{r}_l \partial \mathbf{r}_j} \cdot \frac{\partial \mathbf{R}_i}{\partial g_v} dt + k_B T \sum_{kjl} \mathbf{P}_{kj}^{\mathrm{T}} : \left( \tfrac{\partial}{\partial \mathbf{r}_k} \mathbf{D}_{jl} \right) \cdot \mathbf{P}_{il}^{\mathrm{T}} dt \end{aligned} \quad , \quad \text{(A3.1)}$$

where $\mathbf{r}_i$ is the position vector of bead $i$ ($i$ and $j$ = 1, 2, … $N_{\mathrm{bead}}$ with the number of beads $N_{\mathrm{bead}}$ per chain). $\mathbf{P}$ is the dynamical projection tensor, $\mathbf{D}$ the mobility tensor, and tensor $\mathbf{B}$ the decomposed tensor of the mobility tensor ( $\mathbf{D}_{ij} = \sum_k \mathbf{B}_{ik} \cdot \mathbf{B}_{jk}^{\mathrm{T}}$ ). $\boldsymbol{\kappa}$ is the velocity gradient tensor [same as A2.2], and $\mathbf{F}_i$, $\mathbf{F}_i^{(e)}$, and $\mathbf{F}_i^{(m)}$ are internal interaction, external forces, and metric forces on bead $i$, respectively. $\mathbf{W}_i$ is the time-dependent random variable of bead $i$ and $g_v$ are the constraints [$g_v(\{\mathbf{r}_i\}) = 0$ for $v$ = 1, …, $d'$ where $d'$ is the number of independent constraints]. $k_B$ refers to the Boltzmann constant. This stochastic differential equation was integrated in the following order. First, move the particle position without the constraints,

$$\mathbf{r}'_i = \mathbf{r}_i + \left[ \mathbf{v}_0 + \boldsymbol{\kappa} \cdot \mathbf{r}_i + \sum_j \mathbf{D}_{ij} \cdot \left( \mathbf{F}_j + \mathbf{F}_j^{(e)} + \mathbf{F}_j^{(m)} \right) \right] \Delta t + \sqrt{2k_B T} \sum_j \mathbf{B}_{ij} \cdot \Delta \mathbf{W}_j \,, \quad \text{(A3.2)}$$

where $\Delta\mathbf{W}_i$ is the increment of the Wiener process for the time step ($\langle \Delta\mathbf{W}_i \rangle = 0$ and $\langle \Delta\mathbf{W}_i(0) \Delta\mathbf{W}_j(\Delta t) \rangle = \delta_{ij}\delta(\Delta t)$). All the variables on the right-hand side of (A3.2) are evaluated at the beginning of the time step. After taking the unconstrained move, the final bead position was found with constraint forces:

$$\mathbf{r}_i \left( t + \Delta t \right) = \mathbf{r}'_i - \sum_{v=1}^{d'} \gamma_v \left[ \sum_j \mathbf{D}_{ij} \cdot \frac{\partial g_v}{\partial \mathbf{r}_j} \right]_c \,, \quad \text{(A3.3)}$$

where the terms in $[\ ]_c$ are evaluated at the position $[(1-c)\mathbf{r}_i + c\,\mathbf{r}_i']$ ($c$ was set equal to 0.5 for all BD simulations) and $\gamma_v$ is Lagrange multipliers for the constraint sets $\{g_v\}$ (order of $\gamma$ is $\Delta t$). The Lagrange multipliers can be obtained by using the iterative method of Liu.[21] The iteration procedure for the

ULSAN NATIONAL INSTITUTE OF SCIENCE AND TECHNOLOGY

Lagrange multipliers starts from the constraint equation $\left(\mathbf{r}_{i+1}-\mathbf{r}_i\right)^2-a^2=0$ ($a$ is the bond length for a rigid rod):

$$\mathbf{r}_i\left(t+\Delta t\right)=\mathbf{r}'_i-\sum_{v=1}^{d'}\gamma_v\left[\sum_j\mathbf{D}_{ij}\cdot\frac{\partial g_v}{\partial\mathbf{r}_j}\right]_c, \tag{A3.4}$$

$$\mathbf{r}_{i+1}\left(t+\Delta t\right)=\mathbf{r}'_{i+1}-\sum_{v=1}^{d'}\gamma_v\left[\sum_j\mathbf{D}_{i+1j}\cdot\frac{\partial g_v}{\partial\mathbf{r}_j}\right]_c, \tag{A3.5}$$

$$\mathbf{u}_i\left(t+\Delta t\right)=\mathbf{u}'_i-\sum_{v=1}^{d'}\gamma_v\left[\sum_j\left(\mathbf{D}_{i+1j}-\mathbf{D}_{ij}\right)\cdot\frac{\partial g_v}{\partial\mathbf{r}_j}\right]_c, \tag{A3.6}$$

$$\left(\mathbf{u}'_i\right)^2-a^2-2\sum_{v=1}^{d'}\gamma_v\left[\sum_j\left(\mathbf{D}_{i+1j}-\mathbf{D}_{ij}\right)\cdot\frac{\partial g_v}{\partial\mathbf{r}_i}\right]_c\cdot\mathbf{u}'_i+\left\{\sum_{v=1}^{d'}\gamma_v\left[\sum_j\left(\mathbf{D}_{i+1j}-\mathbf{D}_{ij}\right)\cdot\frac{\partial g_v}{\partial\mathbf{r}_j}\right]_c\right\}^2=0, \tag{A3.7}$$

where the $\mathbf{r}_{i+1}$ and $\mathbf{r}_i$ are connected with rigid bond, and $\mathbf{u}_i$ is the bond vector between the position vectors ($\mathbf{u}_i=\mathbf{r}_{i+1}-\mathbf{r}_i$). The simple iteration equation was obtained by dividing the two $\gamma$ terms in eq A3.7. The $n^{\text{th}}$ approximation of the Lagrange multiplier is given by:

$$\begin{aligned}&\left(\mathbf{u}'_i\right)^2-a^2+\left\{\sum_{v=1}^{d'}\gamma_v^{(n-1)}\left[\sum_j\left(\mathbf{D}_{i+1j}-\mathbf{D}_{ij}\right)\cdot\frac{\partial g_v}{\partial\mathbf{r}_j}\right]_c\right\}^2\\&=2\sum_{v=1}^{d'}\gamma_v^{(n)}\left[\sum_j\left(\mathbf{D}_{i+1j}-\mathbf{D}_{ij}\right)\cdot\frac{\partial g_v}{\partial\mathbf{r}_j}\right]_c\cdot\mathbf{u}'_v\end{aligned}, \tag{A3.8}$$

where $n$ indicates the number of iterations. The procedures start with $\gamma_v^{(0)}=0$. In eq S14, we set the residual $\varepsilon$ as, $\varepsilon=\sum_v\left|\gamma_v^{(n)}-\gamma_v^{(n-1)}\right|$, and this procedure is repeated until the residual is lower than a specific tolerance ($\varepsilon<0.0001\Delta t$).

The EV interactions are described with the Week-Chandler-Andersen Lennard-Jones potential model[22] treating the bead as a "hard sphere," non-dimensionalized with $k_BT$:

$$U_{LJ}(r_{ij})=\begin{cases}4\left[\left(\dfrac{\sigma}{r_{ij}}\right)^{12}-\left(\dfrac{\sigma}{r_{ij}}\right)^{6}\right] & r_{ij}\le 2^{1/6}\sigma\\ -1 & r_{ij}>2^{1/6}\sigma\end{cases}, \tag{A3.9}$$

between all the non-bonded beads $i$ and $j$ ($r_{ij}=|\mathbf{r}_{ij}|=|\mathbf{r}_i-\mathbf{r}_j|$). The parameter $\sigma=0.8\,a$ is indicative of the diameter of a bead. HI is included with the Rotne-Prager-Yamakawa tensor $\mathbf{D}_{ij}$,[23,24] non-dimensionalized with $k_BT/\xi$:

ULSAN NATIONAL INSTITUTE OF SCIENCE AND TECHNOLOGY

$$\mathbf{D}_{ij} = \begin{cases} \mathbf{I} & i = j \\ \dfrac{3\sigma}{4|\mathbf{r}_{ij}|}\left[\left(1+\dfrac{2\sigma^2}{3r_{ij}^2}\right)\mathbf{I}+\left(1-\dfrac{2\sigma^2}{r_{ij}^2}\right)\dfrac{\mathbf{r}_{ij}\mathbf{r}_{ij}^T}{r_{ij}^2}\right] & i \neq j, |r_{ij}| \geq \sigma \\ \left[\left(1-\dfrac{9|\mathbf{r}_{ij}|}{32\sigma}\right)\mathbf{I}+\left(\dfrac{3}{32\sigma|\mathbf{r}_{ij}|}\right)\mathbf{r}_{ij}\mathbf{r}_{ij}^T\right] & i \neq j, |r_{ij}| < \sigma \end{cases}, \quad \text{(A3.10)}$$

where $\xi$ and **I** are the bead friction coefficient and the second-rank unit tensor, respectively. The longest characteristic relaxation time $\tau_R^*$ [made dimensionless by normalizing with $\xi a^2 / k_B T$, i.e., $\tau_R^* = \tau / \left(\xi a^2 / k_B T\right)$] of the system, which is estimated by the integral below the stretched-exponential curve describing the time autocorrelation function for the unit $\mathbf{R}_d$ for ring polymer and unit $\mathbf{R}_{ete}$ for linear polymer;[6] $\tau_R^* = 63.3 \pm 1.0$ and $\tau_R^* = 124 \pm 2.0$ for the ring and linear polymers, respectively.

ULSAN NATIONAL INSTITUTE OF
SCIENCE AND TECHNOLOGY

## 4. References

[1] Flory, P. J. *Statistical Mechanics of Chain Molecules*; Wiley, New York, 1969.

[2] Bird, R. B.; Curtiss, C. F.; Armstrong, R. C.; Hassager, O. Dynamics of Polymeric Liquids; Wiley: New York, 1987; Vol. 2.

[3] Rouse, P. A., Theory of the linear viscoelastic properties of dilute solutions of coiling polymers. *J. Chem. Phys.* **1953**, *21*, 1272-1280.

[4] Kim, J. M.; Edwards B. J.; Keffer D. J.; Khomami B. Dynamics of individual molecules of linear polyethylene liquids under shear: Atomistic simulation and comparison with a free-draining bead-rod chain. *J. Rheol.* **2010**, *54*, 283-310.

[5] Kim, J. M.; Keffer, D. J.; Kröger, M.; Edwards, B. J. Rheological and entanglement characteristics of linear chain polyethylene liquids in planar Couette and planar elongational flows. *J. Non-Newtonian Fluid Mech.* **2008**, *152*, 168-183.

[6] Baig, C.; Mavrantzas, V. G.; Kröger, M. Flow effects on melt structure and entanglement network of linear polymers: Results from a nonequilibrium molecular dynamics simulation study of a polyethylene melt in steady shear. *Macromolecules* **2010**, *43*, 6886-6902.

[7] Nosé, S. A molecular dynamics method for simulations in the canonical ensemble. *Mol. Phys.* **1984**, 52, 255-268.

[8] Hoover, W. G. Canonical dynamics: Equilibrium phase-space distributions. *Phys. Rev. A* **1985**, 31, 1695.

[9] Lees, A.; Edwards, S. The computer study of transport processes under extreme conditions. *J. Phys. C: Solid State Phys.* **1972**, *5*, 1921.

[10] Tuckerman, M.; Berne, B. J.; Martyna, G. J. Reversible multiple time scale molecular dynamics. *J. Chem. Phys.* **1992**, *97*, 1990-2001.

[11] Siepmann, J. I.; Karaborni, S.; Smit, B. Simulating the critical behaviour of complex fluids. *Nature* **1993**, *365*, 330-332.

[12] van der Ploeg, P.; Berendsen, H. Molecular dynamics simulation of a bilayer membrane. *J. Chem. Phys*. **1982**, *76*, 3271-3276.

[13] Jorgensen, W. L.; Madura, J. D.; Swenson, C. J. Optimized intermolecular potential functions for liquid hydrocarbons. *J. Am. Soc*. **1984**, *106*, 6638-6646.

[14] Williams, G.; Watts, D. C. Non-symmetrical dielectric relaxation behaviour arising from a simple empirical decay function. *Trans. Faraday Soc*. **1970**, *66*, 80-85.

[15] Williams, G.; Watts, D. C.; Dev, S.; North, A. Further considerations of non symmetrical dielectric relaxation behaviour arising from a simple empirical decay function. *Trans. Faraday Soc*. **1971**, *67*, 1323-1335.

[16] Tsolou, G.; Mavrantzas, V. G.; Theodorou, D. N. Detailed atomistic molecular dynamics simulation of cis-1, 4-poly (butadiene). *Macromolecules* **2005**, *38*, 1478-1492.

ULSAN NATIONAL INSTITUTE OF
SCIENCE AND TECHNOLOGY

[17] Yoon, J.; Kim, J.; Baig, C. Nonequilibrium molecular dynamics study of ring polymer melts under shear and elongation flows: A comparison with their linear analogs. *J. Rheol*. **2016**, *60*, 673-685.

[18] Ramachandran, R. et al. Persistence length of short-chain branched polyethylene. *Macromolecules* **41**, 9802-9806 (2008).

[19] Öttinger, H. C. Brownian dynamics of rigid polymer chains with hydrodynamic interactions. *Phys*. *Rev*. *E* **1994**, *50*, 2696.

[20] Öttinger, H. C. *Stochastic Processes in Polymeric Fluids*; Springer: Berlin, 1996.

[21] Liu, T. W. Flexible polymer chain dynamics and rheological properties in steady flows. *J. Chem*. *Phys*. **1989**, *90*, 5826-5842.

[22] Weeks, J. D.; Chandler, D.; Andersen, H. C. Role of repulsive forces in determining the equilibrium structure of simple liquids. *J. Chem*. *Phys*. **1971**, *54*, 5237-5247.

[23] Rotne, J.; Prager, S. Variational treatment of hydrodynamic interaction in polymers. *J. Chem*. *Phys*. **1969**, *50*, 4831-4837.

[24] Yamakawa, H. Transport properties of polymer chains in dilute solution: hydrodynamic interaction. *J. Chem*. *Phys*. **1970**, *53*, 436-443.

ULSAN NATIONAL INSTITUTE OF
SCIENCE AND TECHNOLOGY

## Acknowledgements

I deeply appreciate to all supports and helps that I received during my Ph. D.

박사 학위 과정동안 받은 많은 도움과 지지에 감사드립니다.

학위과정의 시작부터 마무리까지 저를 지도해주신 백충기 지도교수님께 깊은 감사를 드립니다. 교수님의 지도와 교육 덕분에 고분자 물리 및 유변학에 관한 연구를 알고 공부할 수 있었습니다. 교수님의 연구철학과 연구에 임하고 이를 대하는 태도 등으로부터 배움을 얻고 연구자로서 스스로의 기반을 닦을 수 있었던 매우 보람 있는 시간이었습니다. 이제까지의 지도와 조언들을 바탕으로 계속하여 발전하고 배워가는 연구자가 되도록 하겠습니다.

제가 연구를 시작하고 공부하는데 있어 많은 도움을 주신 김준모 교수님께도 깊은 감사를 드립니다. 김준모 교수님의 도움과 많은 경험을 통해 연구를 하는데 있어 어려웠던 부분들을 해결하고 헤쳐 나갈 수 있었습니다.

그리고 제 박사 학위 심사에 응해 주시고 많은 조언을 해 주신 김재업 교수님, 이지석 교수님, 이동욱 교수님께도 감사를 드립니다.

학부생 일때부터 함께 같은 연구실에서 같은 분야를 연구하며 많은 의견과 도움을 주고받고 힘들 때 의지가 되어준 연구실 동료들, 태희, 정하, 소담, 은정, 진성, 수원, 욱중, 동연, 태용에게도 감사를 전합니다.

끝으로 긴 학위 과정 기간 동안 많은 사랑과 도움을 주신 사랑하는 부모님, 동생들, 그리고 친척분들에게도 감사를 전하고 싶습니다.

모두 감사합니다.

ULSAN NATIONAL INSTITUTE OF SCIENCE AND TECHNOLOGY

## List of publications

[1] **Jeong, S. H.**; Kim, J. M.; Yoon, J.; Tzoumanekas, C.; Kröger, M.; Baig, C. Influence of molecular architecture on entanglement network: topological analysis of linear, long- and short-chain branched polyethylene melts via Monte Carlo simulation. *Soft Matter* **2016**, *12*, 3770.

[2] **Jeong, S. H.**; Kim, J. M.; Baig, C. Rheological Influence of Short-chain branching for polymeric materials under shear with variable branch density and branching architecture. *Macromolecules* **2017**, *50*, 4491.

[3] **Jeong, S. H.**; Kim, J. M.; Baig, C. Rheological behaviors of H-shaped polymers incorporated with short branches under shear and elongational flows via FENE-Rouse model. *J. Rheol.* **2018**, *62*, 1115.

[4] **Jeong, S. H.**; Cho, S.; Roh, E. J.; Ha, T. Y.; Kim, J. M.; Baig, C. Intrinsic surface characteristics and dynamic mechanisms of ring polymer solutions and melts under shear flow. *Macromolecules* **2020**, *53*, 10051.

[5] **Jeong, S. H.**; Cho, S.; Ha, T. Y.; Roh, E. J.; Baig, C. Structural and dynamical characteristics of short-chain branched ring polymer melts at interface under shear flow. *Polymers* **2020**, *12*, 3068.